2017

Development of Rhodamine 6G Thin Filmn as a Fluorescent Sensor for Explosive Vapor Detection

Mingyu Chapman
University of Rhode Island, mliu@chm.uri.edu

DEVELOPMENT OF RHODAMINE 6G THIN FILM AS A FLUORESCENT SENSOR FOR EXPLOSIVE VAPOR DETECTION

BY

MINGYU CHAPMAN

A DISSERTATION SUBMITTED IN PARTIAL FULFILLMENT OF THE REQUIREMENTS FOR THE DEGREE OF DOCTOR OF PHILOSOPHY OF SCIENCE

IN

CHEMISTRY

UNIVERSITY OF RHODE ISLAND

2017

DOCTOR OF PHILOSOPHY DISSERTATION

OF

Mingyu Chapman

APPROVED:

Dissertation Committee

Major Professor William B. Euler

Sze Yang

Geoffrey Bothun

Nasser H. Zawia
DEAN OF THE GRADUATE SCHOOL

UNIVERSITY OF RHODE ISLAND

2017

Abstract

With increasing public concern for possible future terrorist attacks involving novel explosives, there is a demand for advanced early detection technology. While trained canines are effective at detecting minute quantities of explosive vapors, canines also suffer from false positives, short attention spans, stress, expensive training, and require the assistance of an accompanying handler. Even with these disadvantageous, canines are currently more common in explosive detection due to conventional sensors. The extremely low vapor pressures at room temperature of most explosives limit the number of explosives molecules to be collected in a reasonable detection time pushes limits for most conventional sensors. Most of these sensor devices are big, as they require a vapor collection and pre-concentration system, and require time-consuming procedures. In addition, the concentration of explosive vapors decreases exponentially as a function of distance from the source, and as the function of time the explosive material is present in a location. The detection of trace quantities of explosives in the gas phase is very important in countering terrorist threats. Nanotechnology-enabled sensors could offer significant advantages over conventional sensors, such as better sensitivity and selectivity, lower production costs, reduced power consumption as well as improved stability. The purpose of this research is to provide a fundamental understanding of the materials and mechanisms required and aid in the development of small, inexpensive, effective portable sensor, which is capable for real time detecting explosives vapor at room temperature using only nature vapor pressure.

A new array sensing system for explosive gas phase is proposed in this study. This sensor is based on a layered structure of fluorophore deposited onto a few hundred nanometers of a transparent polymer, supported by a glass slide. The fluorophores

selected, Rhodamine 6G (Rh6G) and related species, are inexpensive xanthene laser dyes which are widely used as a fluorescence tracers because of their strong absorption properties in the visible light region and a high fluorescence quantum yield.

The adsorption of these dyes into solid host systems can alter the photophysical properties of the dye and protect it from thermal decomposition and photobleaching, thus improving the operating and lifetime of the dye. The incorporation of fluorescent dyes into a solid host system becomes of great interest for design of photonic devices with potential applications such as solid tunable lasers and sensors. The type and concentration of aggregates depends on the conditions used for preparation of the hybrid materials.

Formation of aggregates can affect the photophysical characteristics by inducing spectral shifts and band splitting. The presence of aggregates also leads to strong fluorescence quenching at high concentrations. Therefore, controlling the state of aggregation of the dye molecules in a solid matrix is a critical condition for efficiency of fluorescence sensor. The solvent system also plays a role in aggregation formation and a variety of solvents with differing polarities will be used to optimize this technology.

When this fluorophore layer is applied on an appropriate substrate structure before putting on the glass substrate, such as transparent layer of polymer, a huge emission enhancement will occur. This emission enhancement can be explained by internal reflection: When the light hits on the fluorophore layer, some of the light is reflected at each interface, which allows the light to bounce along the polymer layer, this internal reflection can provide more opportunities for the incident light to be absorbed, as a result, the emission enhancement could be over a factor of 1000. This huge emission enhancement shows the potential to be used as fluorescence-based sensor with improved

sensitivity, and it is sensitive enough to detect explosives with low vapor pressures under room temperature.

With this new sensing system, selectivity can be improved by using a variety of fluorophores with high quantum yield to create a sensor array. Each array of fluorophores will give a distinctive response to an analyte, resulting in different response pattern for each analyte. A standard pattern for each known analytes can be used on identifying unknowns by this array response pattern.

The photophysical properties of the fluorophores structure and polymer layer effect on the fluorophores needs to be further understood in order to develop this array sensor with improved sensitivity and selectivity.

ACKNOWLEDGMENTS

I would like to express my gratitude to Professor William Euler for advising me throughout my graduate school career. I am grateful to have Professor Euler as well as Professor Sze Yang, Professor Louis Kirschenbaum, Professor Otto Gregory, and Professor Geoffrey Bothun to have taken the time out of their busy schedules to review my dissertation. I would like to also acknowledge the University of Rhode Island Chemistry department for providing the resources required for this work and providing me with a Teaching Assistantship every semester that funded my education. This material is based upon work supported by the U.S. Department of Homeland Security, Science and Technology Directorate, Office of University Programs, under Grand Award 2013-ST-061-ED001.

Finally, thank you to my husband, Navid, my parents, Lin and Qinghui, and my guardian, Angela Barberton for all their support.

PREFACE

This dissertation is written in manuscript format. The first chapter is a manuscript published in the Journal of Physical Chemistry C. The second chapter is a manuscript that will be submitted to the Journal of Physical Chemistry C. The third chapter is a manuscript that will be submitted to the Journal of Physical Chemistry C. The fourth chapter is a manuscript that will be submitted to the Journal of Physical Chemistry C.

TABLE OF CONTENTS

LIST OF TABLES

Chapter 1

Chapter 2

LIST OF FIGURES

Chapter 1

Chapter 2

Chapter 3

Chapter 4

MANUSCRIPT – I

Published in the Journal of Physical Chemistry C

Structural Evolution of Ultra-thin Films of Rhodamine 6G on Glass

Mingyu Chapman[1], Matthew Mullen[1], Elsa Novoa-Ortega[1], Mona Alhasani[1], James F. Elman[2], and William B. Euler[1]

[1]Chemistry, University of Rhode Island, Kingston, RI, USA

[2]Filmetrics Application Lab-Rochester, Fairport, NY 14450

Corresponding Author: William B. Euler, Ph.D.

Chemistry

University of Rhode Island

140 Flagg Road

Kingston, RI, 02881, USA

Email address: wueler@chm.uri.edu

CHAPTER 1

ABSTRACT

Self-organized rhodamine 6G (Rh6G) thin films on a glass substrate were prepared by spin coating, dip coating, and drop coating. The thickness of the Rh6G layer strongly influences both the absorption and emission spectra, which are accounted for by monomers, exciton and excimer formation, and molecular aggregation. Submonolayer films of Rh6G show one maximum and one apparent shoulder in the absorption spectrum, but three peaks are required for deconvolution of the spectrum. As the thin film becomes thicker the observed maximum shifts to lower energy and a fourth peak is required for deconvolution. The emission spectra show similar features. In addition, the relative intensity of the emission is strongly dependent on the film thickness with thinner films being substantially more emissive than thick films.

INTRODUCTION

Rhodamine 6G (Rh6G) is a cationic xanthene dye widely used as a fluorescence tracer because it has strong absorption in the visible region and a high fluorescence quantum yield.[1–4] Rh6G tends to form aggregates at higher concentration in solutions, leading to the formation of dimers[5–7] and higher order structures.[6–8] The solvent system also plays a role in aggregation because of the hydrophobic alkyl groups on the Rh6G molecule.[9] Polar protic solvents promote aggregation while polar aprotic solvents hinder the aggregation process, and nonpolar solvents can induce deaggregation.[9–12]

Efficient procedures have been developed to incorporate Rh6G into solid matrices such as polymers,[13–16] sol-gel silicates,[17,18] and clays.[19,20] The adsorption of Rh6G into solid host systems can alter the photophysical properties of the dye and protect it from thermal decomposition and photobleaching, thus improving the operating and lifetime of the dye.[21] The incorporation of Rh6G into a solid host system becomes of great interest for design of photonic devices with potential applications such as solid tunable lasers and sensors.[14,21] The type and concentration of aggregates depends on the conditions used for preparation of the hybrid materials.[17,19,21] Controlling the state of aggregation of the dye molecules in a solid matrix is a critical condition for efficiency of a desired application.[17,19–21]

Formation of aggregates can affect the absorption characteristics by inducing spectral shifts and band splitting.[21] The spectral results are typically assigned to two main types of aggregates. A blue shift (relative to the monomer peak) is characteristic of an H-dimer, while a red shift is assigned to a J-dimer.[22] Therefore in solution the absorption spectra contain contributions from monomers and dimers in equilibrium, which is concentration dependent, so that deviations from the Beer-Lambert law occur.[23] The presence of aggregates also leads to strong fluorescence quenching at high concentrations.[24] This quenching process is largely due to the transfer of excitation energy from monomers to aggregates, which then decay non-radiatively.[25]

Exciton theory can be applied to understand the relationship between the structure of the aggregates and their optical characteristics.[26–28] According to this theory, the dye molecule is regarded as a point dipole and the excited state of the dye aggregate splits into two levels through the interaction of the transition dipoles.[26–28] In a J-dimer the monomer transition moments are aligned end-to-end. The lower energy exciton state for the J-dimer is an allowed electric-dipole transition while transition to the upper state is forbidden, so red shifted absorption is observed and the dimer is emissive.[24,26,27] In an H-dimer the monomer transition moments are parallel, and only the higher energy exciton state is allowed. Thus, for an H-dimer a blue shifted absorption band is characteristic and the excited state is a non-emissive species.[26,27] The general dimer is referred to as an oblique dimer, as shown in Scheme 1-1. When the chromophore is adsorbed onto a substrate the dimer is characterized by an

arbitrary angle, θ, between the transition moments.[26,27,29–31] In the common cases discussed above, an H-dimer has θ = 90o and a J-dimer has θ = 0o. For any other value of θ, transition to both exciton excited states is allowed with transition moments: M'=√2Mcosθ (for transition to the lower energy state, E') and M''=√2Msinθ (for transition to the higher exciton state, E"), where M is the transition moment of the monomer. In addition, an excimer can also be formed by the association of excited and unexcited molecules.[32–37] Excimer formation does not affect the absorption spectrum but owing to a mismatch between the monomer Franck–Condon state and the excimer state, a red-shifted emission band with long fluorescence lifetimes are typically observed.[37,38]

In this work we examine the absorption, emission, and excitation spectra for Rh6G deposited onto a glass substrate. The spectra change as a function of thickness, as expected. At submonolayer coverages the primary structures found on the surface are monomers that have the transition moment aligned parallel to the substrate surface. As the thickness increases both excimer and exciton spectroscopic features are observed. Finally, at the thickest coverage the formation of large aggregates occurs, which significantly suppresses emission. These structural conclusions are independent of the coating method used, which include dip-coating, spin-coating, and drop casting. This is in contrast to previous reports, which only assign exciton type dimers[9] and have not identified an excimer.

EXPERIMENTAL SECTION

Rhodamine 6G chloride (Rh6G) was supplied by Acros Organics and was used without further purification. A range of Rh6G solutions were prepared and used for thin film preparation: 1×10^{-9} M – 1×10^{-2} M in 95% ethanol. Borosilicate glass (BSG) microscope slides were prepared by sonication in 95% ethanol and distilled water (15 minutes each) followed by blow-drying with dry nitrogen gas.

A Laurell Technologies spin coater was used for spin-casting films. 250 µl of the Rh6G solution was placed on the BSG slide and the acceleration was set to 1200 rpm and the maximum rotation was set between 400 and 5000 rpm. The thin films were then allowed to dry in air. Dip-coating was done using an MTI Corp. HWTL-01 desktop dip coater with temperature chamber set at room temperature. After coating, the thin film on one side of the BSG slide surface was removed using 95% ethanol. Finally, drop-coated films were prepared by placing a known volume (5 to 20 µL) of a known concentration (5×10^{-7} M To 9×10^{-4} M) of Rh6G on the BSG slide and allowed to air dry. All thin films were prepared at low humidity (<20%).

The absorption spectra were obtained using a Perkin Elmer Lambda 1050 spectrometer. The slit width was set to 2 nm, the wavelength range was set from 700 nm to 350 nm, and the integration time was set to 10 s for samples made with concentrations lower than 2×10^{-6} M, 5 s for sample made with concentrations between 3×10^{-6} M to 3×10^{-5} M, 3 s for samples made with concentrations

between 4×10^{-5} M and 1×10^{-4} M, and 1 s for samples made with concentrations above 1×10^{-4} M. Polarized spectra were obtained using a Perkin Elmer Polarizer L900. The polarization angles used were from 0° to 220°. All spectra were baseline corrected by automatic baseline subtraction with PeakFit v4.12 software.

The fluorescence emission spectra and excitation spectra was acquired using a Horiba (Jobin Yvon) Fluorolog spectrometer. The light source used was a Xenon arc lamp. For emission spectra, the excitation wavelength was set at the absorbance maximum, and the slit width was set to 2 nm. For excitation spectra, the detection wavelengths used were 550 nm, 573 nm, 600 nm, 650 nm, and the maximum emission wavelength.

Time-resolved emission spectroscopy (TRES) measurements were made using a Horiba Fluorohub time-correlated single photon counting (TCSPC) system. A Horiba NanoLED N-460 pulsed diode laser was used as the light source with a wavelength of 464 nm, a repetition rate of 1.0 MHz, and 160 ps pulse duration time with a power output of about 7 pJ/pulse.

XPS measurements were carried out using a ThermoFisher K-Alpha spectrometer, under a focused monochromatised Al Ka radiation (E = 1486.6 eV). Spectra were recorded with a constant pass energy of 50 eV with energy resolution of 50 meV and charge neutralization. The peak positions and areas were optimized by a weighted least squares fitting method using Avantage (ThermoFisher) software.

AFM measurements were carried out using an Agilent 5500 AFM in tapping mode. The tip used was from Mikromasch, NSC15/A1 BS and had a force constant of 20-80 N/m. The angle of repose was used at about 15 degrees. The scan area was 95 μm by 5.9 μm.

Reflection spectra were obtained using a Filmetrics F40 microscope Thin Film Analyzer and thicknesses were fit using the software provided. Optical constants for Rh6G were determined by spin-casting films onto fused silica and the wavelength dependence of n and k are shown in Fig. 1-S1. The results are in good agreement with the literature.[39]

RESULTS AND DISCUSSION

Three solution deposition techniques were used to deposit Rh6G molecules as a thin film onto a glass substrate: dip coating, drop coating, and spin coating, with evaporation rate of the solvent increasing in the given order. In dip coating, the substrate to be coated is lowered into the solution and withdrawn at a suitable speed while for spin coating the solution is placed onto the substrate, which is then rotated at a high speed. Drop coating simply involves placing drops of the liquid onto the surface of the substrate. The different deposition techniques allowed controllable access to a wide range of film thicknesses, ranging from submonolayer to tens of layers.

The absorption spectra of a series of films are shown in Figure 1-1. As expected, as the Rh6G concentration increases in the casting solution, the films become thicker and the spectra more intense, as demonstrated in Figure 1-1A. However, there are also significant changes in the lineshape as the film thickness changes, indicating structural changes in the Rh6G film. As shown in the normalized spectra in Figure 1-1B, when using the lowest concentrations the film spectrum has a maximum at 525 nm and a small shoulder at ~490 – 500 nm. As the concentration of the casting solution increases and the film becomes thicker, the main peak shifts to lower energy and the high energy shoulder becomes more prominent.

Figure 1-2 shows the evolution of λmax (the wavelength of maximum absorption) and the absorbance at λmax as a function of film thickness. As shown in Figure 1-2A, λmax shifts from ~520 nm to ~560 nm between film thicknesses

of < 1 nm to about 10 nm. When the film is greater than 10 nm thick, λmax and the overall lineshape does not change with increasing film thickness. Similar behavior is seen for the absorbance at λmax, where it appears that three regions of different slopes are observed: 0 – ~1 nm, ~ 1 nm – ~ 10 nm, and > 10 nm.

The different thickness regimes require different methods for measurement. As demonstrated in Figure 1-2, we used reflection spectroscopy, XPS, AFM, and a simple area and density method to determine the film thickness. All methods were in agreement, giving us confidence that the thicknesses reported are meaningful. The absorbance (A) as a function of thickness (t) can be approximated by three different linear regions:

$$A = 0.019t - 0.012 \quad (t < 1.2 \text{ nm}, A < 0.025) \qquad [1]$$

$$A = 0.011t + 0.014 \quad (1.2 \text{ nm} < t < 12 \text{ nm}, 0.025 < A < 0.14) \qquad [2]$$

$$A = 0.0057t + 0.088 \quad (t > 12 \text{ nm}, A > 0.14) \qquad [3]$$

The uncertainties in the slopes are 0.009 nm–1 for equation [1], 0.002 nm–1 for equation [2], and 0.001 nm–1 for equation [3].

The data can be used empirically to determine the film thickness. Depending upon the orientation of the Rh6G molecule on the surface, a monolayer should be 0.9 – 1.4 nm thick. The break in slopes at ~ 1 nm suggests that the absorbance of films thinner than 1 nm is no longer being controlled by the thickness of the film but by the surface density of the Rh6G molecules.

The absorption spectra were deconvoluted into the component parts. Only four peaks were required to fit the observed spectra over the entire thickness

range. The absorption maxima and linewidths are given in Table 1-1 and representative fits for several thicknesses are given in Figure 1-S2.

Figure 1-3 shows the relationship between the concentration of Rh6G and the film thickness when coating by different methods. The Rh6G thickness is primarily controlled by the Rh6G concentration. If different rotation rates are used for spin-coating or different pull rates for dip-coating, different thicknesses are found but the variation is much smaller than that caused by the concentration. The shapes of the absorption spectra are independent of the deposition method. Consequently, further discussion will be based on films spin-cast at 1200 rpm, unless otherwise noted. Since all of the deposition techniques used here are evaporative, the initial solution concentration always increases during the deposition process. This allows some dimerization to occur even for the most dilute solution. However, the slow evaporation process (dip-coating and drop coating) and the fast evaporation process (spin-coating) leading to similar structures suggests that some fraction of the Rh6G is deposited onto the substrate by adsorption from solution before any evaporation starts. This would account for the observation that the rotation rate in the spin-coating process has little effect on the film thickness. Also, the low concentrations of the casting solutions means that there is little viscosity change for the different solutions, which also is consistent with the spin rate having only a small effect on the resulting film thickness.

Polarized absorbance spectra were recorded to provide further understanding of the Rh6G thin film structure. With the available instrumentation,

only polarization in the plane of the glass substrate (x-y) was accessible. Thus, if the Rh6G transition moment lies parallel to the surface, absorption would be observed but if the transition moment is perpendicular to the surface then no light would be absorbed. Figure 1-4 shows the polarized spectra for several different film thicknesses. For the thinnest films, Figure 1-4A, the x-y polarized spectra show absorption for the low energy peak and significant noise around the high energy shoulder. As the thickness is increased, the polarized spectra have the same shape as the unpolarized spectrum but with less intensity, figure 1-4B. With further increase in thickness, Figure 1-4C, the polarized spectra almost match the unpolarized spectra. Finally, at the highest thicknesses, Figure 1-4D, the polarized spectra is similar to unpolarized spectra at high energy, but the polarized spectrum is less intense in the low energy region.

The steady state emission spectra are shown in Figure 1-5. Similar to the absorption spectra, both the intensity and the emission wavelength maximum are strongly affected by the film thickness. As shown in Figure 1-5A, the emission maxima shift to longer wavelength as the film becomes thicker. The normalized spectra shown in Figure 1-5B demonstrate the lineshape changes. As the films become thicker the peaks become broader. All of the emission spectra could be deconvoluted into 4 peaks, with the parameters given in Table 1-1 and representative fits shown in Figure 1-S3.

Figure 1-6 shows the emission data plotted as a function of film thickness and the Rh6G casting concentration. Thinner films have stronger emission (Fig.

6A) and shorter wavelength maxima (Fig. 6B) while thick films have longer wavelength maxima and are strongly quenched.

Figure 1-7 shows plots of normalized absorption, emission, and excitation spectra for several film thicknesses. For very thin films, <1.2 nm, the absorption and excitation spectra superimpose. However, in this thickness range, the apparent Stokes shift is increasing slowly with increasing film thickness. When the film thickness is >1.2 nm the absorption and excitation spectra no longer match. The excitation spectra always match the high energy portion of the absorption but the low energy peaks are missing. Deconvolution of the excitation spectra gave the exact same peaks and linewidths, given in Table 1-1, as found for the absorption spectra.

We measured the excited state lifetimes for the radiative decay for the films as a function of thickness, as shown in Figure 1-8A. Two or three lifetimes were required to fit the decay curves for the excited state of the thin films, depending upon the thickness: $\tau 1 = 4.0 \pm 0.6$ ns, $\tau 2 = 1.9 \pm 0.7$ ns and $\tau 3 = 0.4 \pm 0.3$ ns, as shown in Figure 1-8B. As the film thickness increases, the lifetimes apparently decrease slightly, but this may be an artifact caused by the increased scattering in the thin films. Figure 1-8C shows the time resolved emission spectra for a film with a thickness of 1.1 nm. The dominant feature in the TRES is a peak centered at ~550 nm with a lifetime in the 1 – 2 ns region. This peak is assigned to the $\tau 1 = 1.9$ ns component found from fitting the decay curves. The TRES reveal a second peak centered at about 575 nm with a longer lifetime, which is assigned to the $\tau 1 = 4.0$ ns component. No component at longer wavelengths was found in

the TRES, presumably because the signal to noise ratio is so poor for these weakly emitting species.

Finally, we used the XPS results to measure the C 1s binding energy as a function of film thickness. The results are shown in Figure 1-S4. As the Rh6G film gets thicker the binding energy becomes smaller, changing from ~286 eV for a 0.7 nm film to ~284 eV for a 2.1 nm film. This shift may arise because of structural changes in the thin film or because of charging effects associated with the thick, nonconducting Rh6G film.[40]

The spectral results suggest the following structures. The Rh6G monomer (M) is found at some concentration in all films. The absorption maximum for the monomer is 527 nm and the emission maximum is found at 550 nm and the lifetime is τ_2 = 1.9 ns. The polarized spectra indicate that the transition moment of the monomer is located in the plane of the substrate. The second structure is an oblique dimer (D), giving rise to excitonic absorption peaks at 500 nm and 548 nm. From exciton theory[26,27] the angle θ (Scheme 1-1) can be found from the relative intensities of each absorption peak and was estimated to be ~67° (±5°). Emission occurs from the oblique dimer only from the lower energy state, assigned to the peak at 600 nm. The third structure is an aggregate (A) (or perhaps initial crystallization) of three or more Rh6G molecules. Aggregates are only found in films with average thicknesses greater than a monolayer (>1.2 nm) and are assigned the absorption peak at 562 nm. A is weakly emissive at 650 nm with a lifetime of τ_3 = 0.4 ns, typical of aggregates because of the increased number of nonradiative pathways available. Finally, the emission peak at 573 nm is assigned

to an excimer (E) with a lifetime of τ_1 = 4.0 ns. The presence of E is implied by the observation that the absorption and excitation spectra overlap for films less that about 1 monolayer thick but the emission spectra show an increase in intensity the 573 nm region as the density of molecules on the surface increases.

The relative amounts of each peak based on the deconvoluted areas are shown in Figure 1-S4. For the thinnest films (< 0.7 nm) the absorption is approximately equally distributed between M (or E) and D. The thinnest films prepared here, ~0.7 nm thick, are about 0.5 monolayer, assuming a closest packed structure and a spherical Rh6G with a diameter of 1.4 nm. At this thickness only about 1.6% of the Rh6G molecules have no nearest neighbors. Thus, observation of a high percentage of D in the absorption is not surprising. The emission in the submonolayer films is also dominated by M and E. The lifetime of the monomer is 1.9 ns, slightly less than the 4.22 ns lifetime for Rh6G in DMF solution,[41] but comprises the largest fraction of decay for films less than 0.7 nm thick (see Table 1-S1). The emission peak at 573 nm and the peak found at ~575 nm in the TRES with a lifetime of 4.0 ns is consistent with the assignment of an excimer. As the films become thicker, the absorption associated with M becomes small and that with A increases. The emission of the thicker films arises primarily from E and D. Only for the thickest films does the fraction of emission from A become significant, although the absolute emission is quenched.

CONCLUSION

Thin films of Rh6G formed by spin-casting, dip-coating, and drop-coating methods exhibit the same spectroscopic and structural characteristics – the coating method does not affect the film structure. At extremely low dye density, when the surface coverage is low, the spectroscopic signature of the monomeric structure is dominant. But even at submonolayer coverages evidence for exciton dimers and excimer formation is found since most of the Rh6G molecules have a nearby neighbor. Based on the exciton geometry, inferred from the intensities of the two peaks associated with the excited state oblique structure, the Rh6G molecules with nearest neighbors are tilted with respect to the surface at ~67°. A further increase in dye density, when the second layer starts to form, results in aggregation or crystallization. This leads to significant quenching of the emission spectrum and suppression of the monomer, excimer, and exciton emission.

Film thickness and structure can be determined by simply measuring the absorption spectrum. For the thinnest films, one monolayer or less (< 1.2 nm), the absorption maximum is found between 520 and 530 nm and the absorbance is less than 0.025. For films of 1 to 10 monolayers the absorption maximum gradually shifts from ~530 nm to ~560 nm as the films become thicker and the absorbance maximum varies between ~0.025 and ~0.14. For films greater than 10 monolayers, where crystallization may be starting, the absorption maximum is 562 nm and the absorbance linearly depends on the thickness. Despite these simple empirical observations, the nature of the excited states change

considerably, even in the submonolayer regime. The changes in the excited state strongly influence the emission characteristics. In films where the average thickness is about 0.5 monolayer the emission from the excited states are dominated by excimers. When this thickness grows a small amount, to 0.7 – 0.8 monolayer, the primary excited states becomes a mix of excimers and excitons, which is demonstrated effectively by the shape of the excitation spectrum. At ~1 monolayer, the excimer excited state becomes less populated and as the thickness grows the aggregate/crystalline structure becomes increasingly important. When the films are several monolayers thick, the aggregate/crystalline structures quench the emission precipitously.

ACKNOWLEDGEMENT

This material is based upon work supported by the U.S. Department of Homeland Security, Science and Technology Directorate, Office of University Programs, under Grant Award 2013-ST-061-ED0001. The views and conclusions contained in this document are those of the authors and should not be interpreted as necessarily representing the official policies, either expressed or implied, of the U.S. Department of Homeland Security.

LIST OF REFERENCES

(1) Zehentbauer, F. M.; Moretto, C.; Stephen, R.; Thevar, T.; Gilchrist, J. R.; Pokrajac, D.; Richard, K. L.; Kiefer, J. Fluorescence Spectroscopy of Rhodamine 6G: Concentration and Solvent Effects. *Spectrochim. Acta - Part A Mol. Biomol. Spectrosc.* **2014**, *121*, 147–151.

(2) De Queiroz, T. B.; Botelho, M. B. S.; De Boni, L.; Eckert, H.; De Camargo, Strategies for Reducing Dye Aggregation in Luminescent Host-Guest Systems: Rhodamine 6G Incorporated in New Mesoporous Sol-Gel Hosts. *J. Appl. Phys.* **2013**, *113*, 1–11.

(3) Penzkofer, A.; Leupacher, W. Fluorescence Behaviour of Highly Concentrated Rhodamine 6G Solutions. *J. Lumin.* **1987**, *37*, 61–72.

(4) Satake, A.; Kobuke, Y. Artificial Photosynthetic Systems: Assemblies of Slipped Cofacial Porphyrins and Phthalocyanines Showing Strong Electronic Coupling. *Org. Biomol. Chem.* **2007**, *5*, 1679–1691.

(5) Liu, T.; Yu, A.; Luo, G.; Zhao, X.; Ying, L.; Huang, Y.; Huang, C. Aggregates in Rhodamine-Labeled Phospholipid Films Probed by Spectroscopy and Atomic Force Microscopy. *Acta Physico-Chimica Sin.* **2000**, *16*, 49–53.

(6) Fedoseeva, M.; Letrun, R.; Vauthey, E. Excited-State Dynamics of Rhodamine 6G in Aqueous Solution and at the Dodecane/Water Interface. *J. Phys. Chem. B* **2014**, *118*, 5184–5193.

(7) Zhao, J.; Jensen, L.; Sung, J.; Zou, S.; Schatz, G. C.; Van Duyne, R. P. Interaction of Plasmon and Molecular Resonances for Rhodamine 6G

Adsorbed on Silver Nanoparticles. *J. Am. Chem. Soc.* **2007**, *129*, 7647–7656.

(8) Antonov, L.; Gergov, G.; Petrov, V.; Kubista, M.; Nygren, J. UV-Vis Spectroscopic and Chemometric Study on the Aggregation of Ionic Dyes in Water. *Talanta* **1999**, *49*, 99–106.

(9) Ojeda, P. R.; Amashta, I. A. K.; Ochoa, J. R.; Arbeloa, I. L. Excitonic Treatment and Bonding of Aggregates of Rhodamine 6G in Ethanol. *J. Chem. Soc. Faraday Trans. 2* **1988**, *84*, 1–8.

(10) De, S.; Das, S.; Girigoswami, A. Environmental Effects on the Aggregation of Some Xanthene Dyes Used in Lasers. *Spectrochim. Acta - Part A Mol. Biomol. Spectrosc.* **2005**, *61*, 1821–1833.

(11) Muntean, S. G.; Simu, G. M.; Kurunczi, L.; Szabadai, Z. Investigation of the Aggregation of Three Diazo Direct Dyes by UV-Vis Spectroscopy and Mathematical Analysis. *Rev. Chim.* **2009**, *60*, 152–155.

(12) Arbeloa, F.; Gonzalez, I. L.; Ojeda, P. R.; Arbeloa, I. L. Aggregate Formation of Rhodamine 6G in Aqueous Solution. *J. Chem. Soc., Faraday Trans* **1982**, *78*, 989–994.

(13) Kurian, A.; George, N.; Paul, B.; Nampoori, V. P. N.; Vallabhan, C. P. G. Studies on Fluorescence Efficiency and Photodegradation of Rhodamine 6G Doped PMMA Using a Dual Beam Thermal Lens Technique. *Laser Chem.* **2002**, *20*, 99–110.

(14) Somasundaram, G.; Ramalingam, A. Laser Gain Studies of Rhodamine 6G Dye Doped Polymer Laser. *Indian J. Pure Appl. Phys.* **1998**, *36*, 310–313.

(15) Martín, V.; Bañuelos, J.; Enciso, E.; Arbeloa, Í.; Costela, Á.; García-Moreno, I. Photophysical and Lasing Properties of Rhodamine 6G Confined in Polymeric Nanoparticles. *J. Phys. Chem. C* **2011**, *115*, 3926–3933.

(16) Zheng, Z.; Liang, H.; Ming, H.; Zhang, Q.; Yu, Y.; Liu, S.; Zhang, Y.; Xie, J. Rhodamine 6G-Doped Polymer Optical Fiber Amplifiers. *Chinese Opt. Lett.* **2004**, *2*, 67–68.

(17) Leonenko, E. V.; Telbiz, G. M.; Bogoslovskaya, A. B.; Manoryk, P. A. Effect of Aggregation of Rhodamine 6G on the Spectral and Luminescence Characteristics of Hybrid Mesostructured Silica Films. *Theor. Exp. Chem.* **2015**, *50*, 358–363.

(18) Lasio, B.; Malfatti, L.; Innocenzi, P. Photodegradation of Rhodamine 6G Dimers in Silica Sol–Gel Films. *J. Photochem. Photobiol. A Chem.* **2013**, *271*, 93–98.

(19) Arbeloa, F.; Estevez, M.; Arbeloa, T.; Arbeloa, I. Spectroscopic Study of the Adsorption of Rhodamine 6G on Clay Minerals in Aqueous Suspensions. *Clay Miner.* **1997**, *32*, 97–106.

(20) Tapia Estevez, M.; López Rbeloa, F.; López Rbeloa, T.; López Rbeloa, I.; Schoonheydt, R. Spectroscopic Study of the Adsorption of Rhodamine 6G on Laponite B for Low Loadings. *Clay Min.* **1994**, *29*, 105–113.

(21) Martínez, V. M.; Arbeloa, F. L.; Prieto, J. B.; Arbeloa, I. L. Characterization of Rhodamine 6G Aggregates Intercalated in Solid Thin

Films of Laponite Clay. 2 Fluorescence Spectroscopy. *J. Phys. Chem. B* **2005**, *109*, 7443–7450.

(22) Micheau, J.; Zakharova, G.; Chibisov, A. Reversible Aggregation, Precipitation and Re-Dissolution of Rhodamine 6G in Aqueous Sodium Dodecyl Sulfate. *Phys. Chem. Chem. Phys.* **2004**, *2*, 2420–2425.

(23) Lu, Y.; Penzkofer, A. Absorption Behaviour of Methanolic Rhodamine 6G Solutions at High Concentration. *Chem. Phys.* **1986**, *107*, 175–184.

(24) Anedda, A.; Carbonaro, C. M.; Corpino, R.; Ricci, P. C.; Grandi, S.; Mustarelli, P. C. Formation of Fluorescent Aggregates in Rhodamine 6G Doped Silica Glasses. *J. Non. Cryst. Solids* **2007**, *353*, 481–485.

(25) Vogel, R.; Meredith, P.; Harvey, M. D.; Rubinsztein-Dunlop, H. Absorption and Fluorescence Spectroscopy of Rhodamine 6G in Titanium Dioxide Nanocomposites. *Spectrochim. Acta - Part A Mol. Biomol. Spectrosc.* **2004**, *60*, 245–249.

(26) Kasha, M.; Rawls, H. R.; Ashraf El-Bayoumi, M. The Exciton Model in Molecular Spectroscopy. *Pure Appl. Chem.* **1965**, *11*, 371–392.

(27) Kasha, M. Energy Transfer Mechanisms and the Molecular Exciton Model for Molecular Aggregates. *Radiat. Res.* **1963**, *20*, 55–70.

(28) Tennakone, K.; Pitigala, P. K. D. D. P.; Perera, A. G. U. Exciton Transport and Electron Mobility of Organized Aggregates of Cationic Dye Thiocyanates. *RSC Adv.* **2013**, *3*, 2770–2775.

(29) Kemnitz, K.; Yoshihara, K. Entropy-Driven Dimerization of Xanthene Dyes in Nonpolar Solution and Temperature-Dependent Fluorescence Decay of Dimers. *J. Phys. Chem.* **1991**, *95*, 6095–6104.

(30) Fujii, T.; Nishikiori, H.; Tamura, T. Absorption Spectra of Rhodamine B Dimers in Dip-Coated Thin Films Prepared by the Sol-Gel Method. *Chem. Phys. Lett.* **1995**, *233*, 424–429

(31) Lofaj, M.; Valent, I.; Bujdak, J. Mechanism of Rhodamine 6G Molecular Aggregation in Montmorillonite Colloid. *Cent. Eur. J. Chem.* **2013**, *11*, 1606–1619.

(32) Birks, J. Excimers. *Rep. Prog. Phys*. **1975**, *38*, 903–974.

(33) Song, Q.; Bamesberger, A.; Yang, L.; Houtwed, H.; Cao, H. Excimer-Monomer Switch: A Reaction-Based Approach for Selective Detection of Fluoride. *Analyst* **2014**, *139*, 3588–3592.

(34) Focsaneanu, K.; Scaiano, J. C. Potential Analytical Applications of Differential Fluorescence Quenching: Pyrene Monomer and Excimer Emissions as Sensors for Electron Deficient Molecules. *Photochem. Photobiol. Sci.* **2005**, *4*, 817–821.

(35) Son, M.; Park, K. H.; Shao, C.; Wu, F.; Kim, D. Spectroscopic Demonstration of Exciton Dynamics and Excimer Formation in a Sterically Controlled Perylene Bisimide Dimer Aggregate. *J. Phys. Chem. Lett.* **2014**, *5*, 3601–3607.

(36) Martinho, J. M. G.; Sreis e Sousa, A.; Oliveira Torres, M. E.; Fedorov, A. Fluorescence Quenching of Pyrene Monomer and Excimer by CH3I. *Chem. Phys.* **2001**, *264*, 111–121.

(37) Penzkofer, A.; Lu, Y. Fluorescence Quenching of Rhodamine 6G in Methanol at High Concentration. *Chem. Phys.* **1986**, *103*, 399–405.

(38) Lim, J. M.; Kim, P.; Yoon, M.; Sung, J.; Dehm, V.; Chen, Z.; Würthner, F.; Kim, D. Exciton Delocalization and Dynamics in Helical π-Stacks of Self-Assembled Perylene Bisimides. *Chem. Sci.* **2013**, 388–397.

(39) Penzkofer, A.; Drotleff, E.; Holzer, W. Optical Constants Measurement of Single-Layer Thin Films on Transparent Substrates. *Optics Commun*. **1998**, *158*, 221 – 230.

(40) Gouzman, I.; Dubey, M.; Carolus, M. D.; Schwartz, J.; Bernasek, S. L. Monolayer vs. Multilayer Self-Assembled Alkylphosphonate Films: X-ray Photoelectron Spectroscopy Studies. Surface Science **2006**, *600*, 773–781.

(41) Latendresse, C. A.; Fernandes, S. C.; You, S.; Zhang, H. Q.; Euler, W. B. A Fluorometric Sensing Array for the Detection of Military Explosives and IED Materials. *Anal. Methods* **2013**, *5*, 5457–5463.

Peak	Absorbance (λ, Γ)	Excitation (λ, Γ)	Emission (λ, Γ)	Thickness (nm)	Concentration (M)
1	500, 26	500, 26	550, 16	0.6-60	$6\times10^{-7} – 1\times10^{-2}$
2	527, 14	527, 14	573, 21	0.6-60	$6\times10^{-7} – 1\times10^{-2}$
3	548, 14	548, 14	600, 35	0.6-60	6×10^{-7} - 1×10^{-2}
4	562, 16	562, 16	650, 47	1.2-60	$3\times10^{-4} – 1\times10^{-2}$

Table 1-1. Deconvoluted peak composition (using a Gaussian lineshape) for absorption and emission spectra as a function of nominal film thickness and Rh6G concentration used. The peak positions (λ) and full width at half-maximum (Γ) are given in pairs. The uncertainties for both λ and Γ are ± 2 nm.

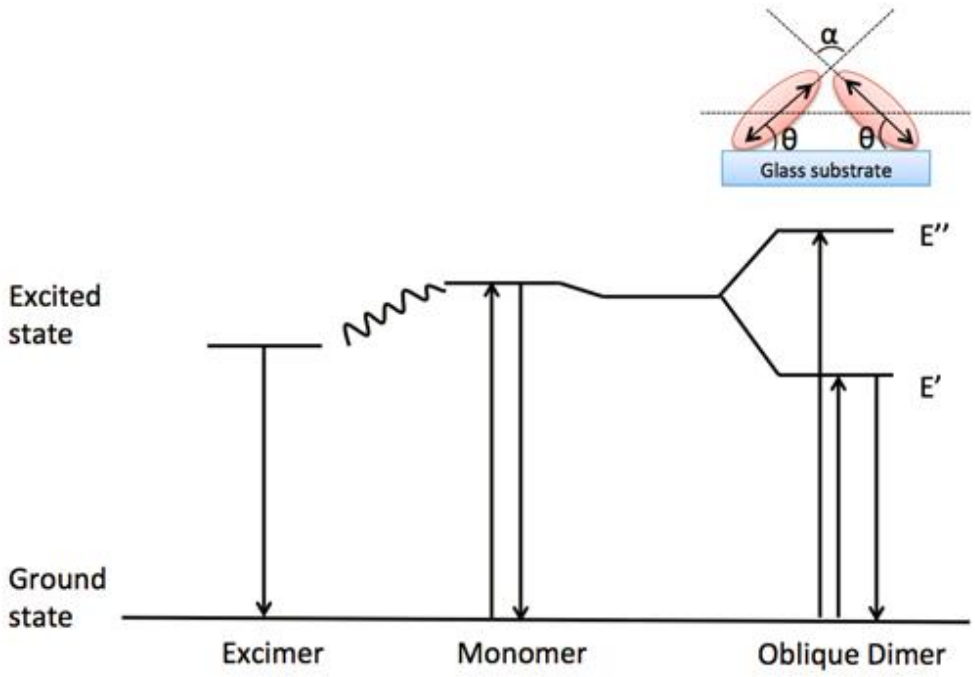

Scheme 1-1. Energy levels for excimer (left), monomer (center), and exciton dimers (right)

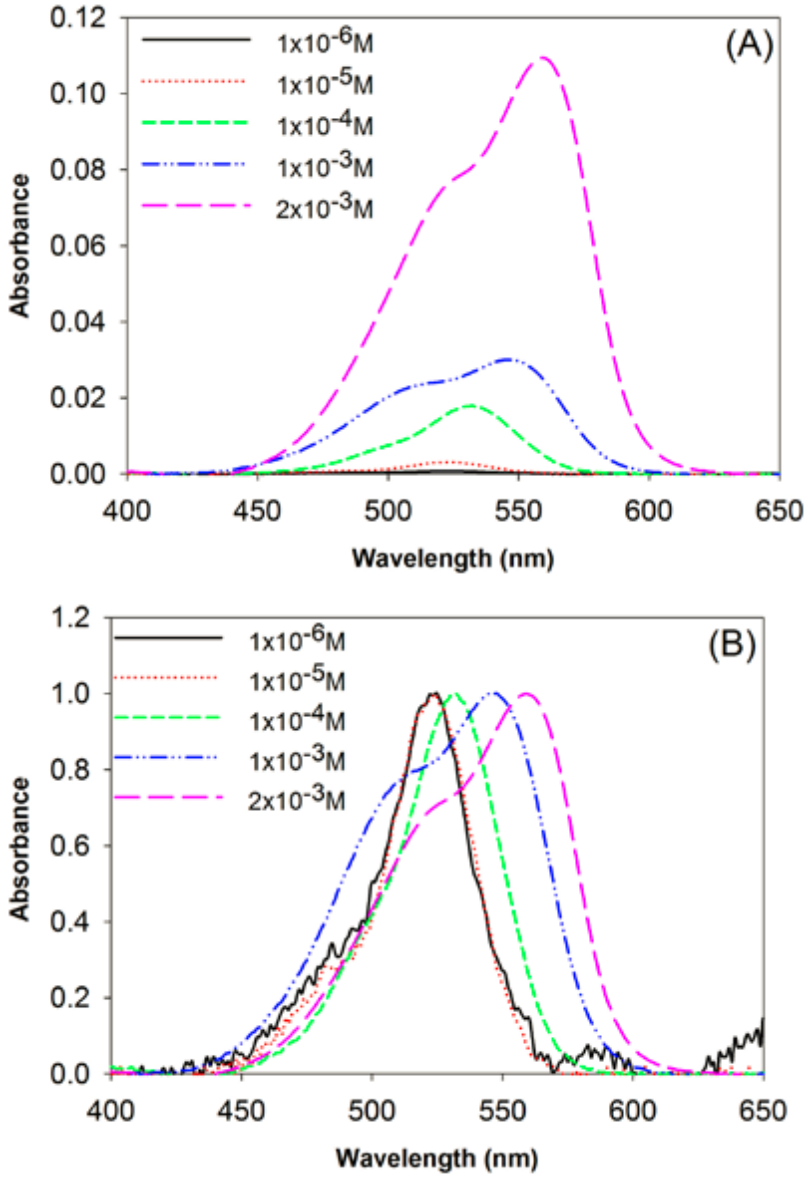

Figure 1-1. Absorption spectra (A) and normalized absorption spectra (B) for spin-cast Rh6G thin films as a function of the concentration of Rh6G in the applied solution. All thin films were formed using a maximum rotation of 1200 rpm.

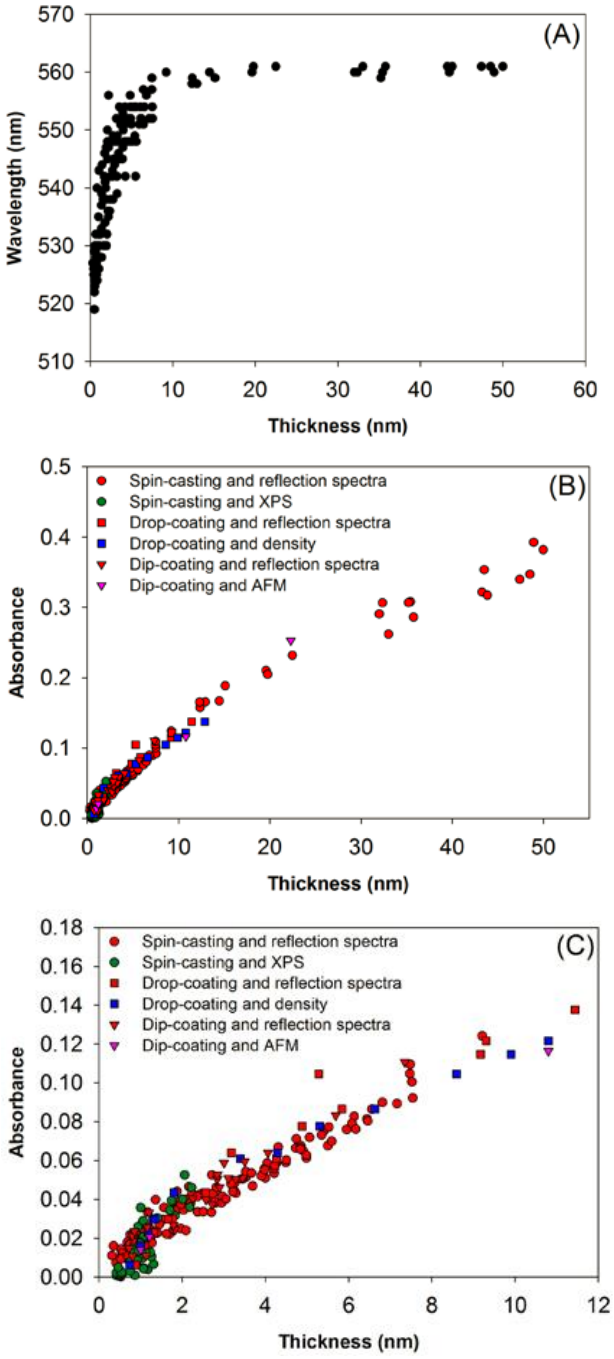

Figure 1-2. λmax (A) and the absorbance at λmax (B) of thin films prepared by different methods plotted as a function of the film thickness with a range from 0 nm to 60 nm. The symbol shape indicates the deposition method: Circles for spin-casting, squares for drop-coating, and triangles for dip-coating. The symbol color indicates how the thickness was determined: red, reflection spectra; green, XPS; blue, density calculation; pink, AFM. (C) Shows an enlarged plot of the region with thickness below 12 nm.

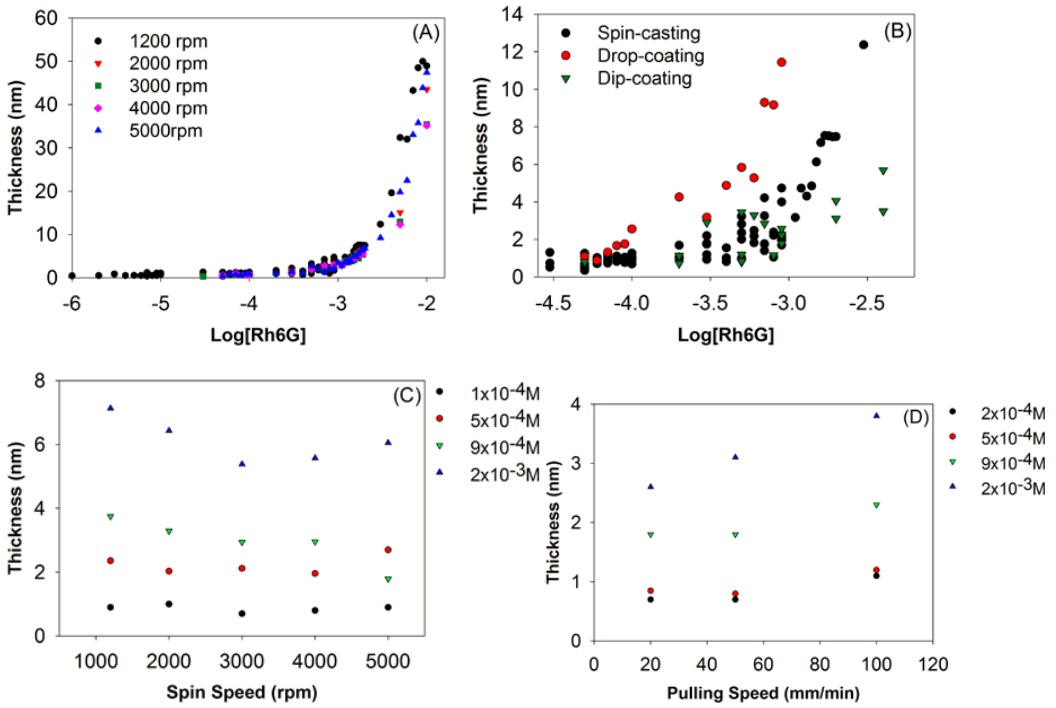

Figure 1-3. A: spin-cast thin films as a function of solution concentration and maximum rotation velocity. B: comparison of film thickness using spin-coating (1200 rpm), drop-coating, and dip-coating as a function of solution concentration. Note the log scale for concentration. C. Relation between film thickness and spin speed. D. Relation between film thickness and pulling speed for dip coating.

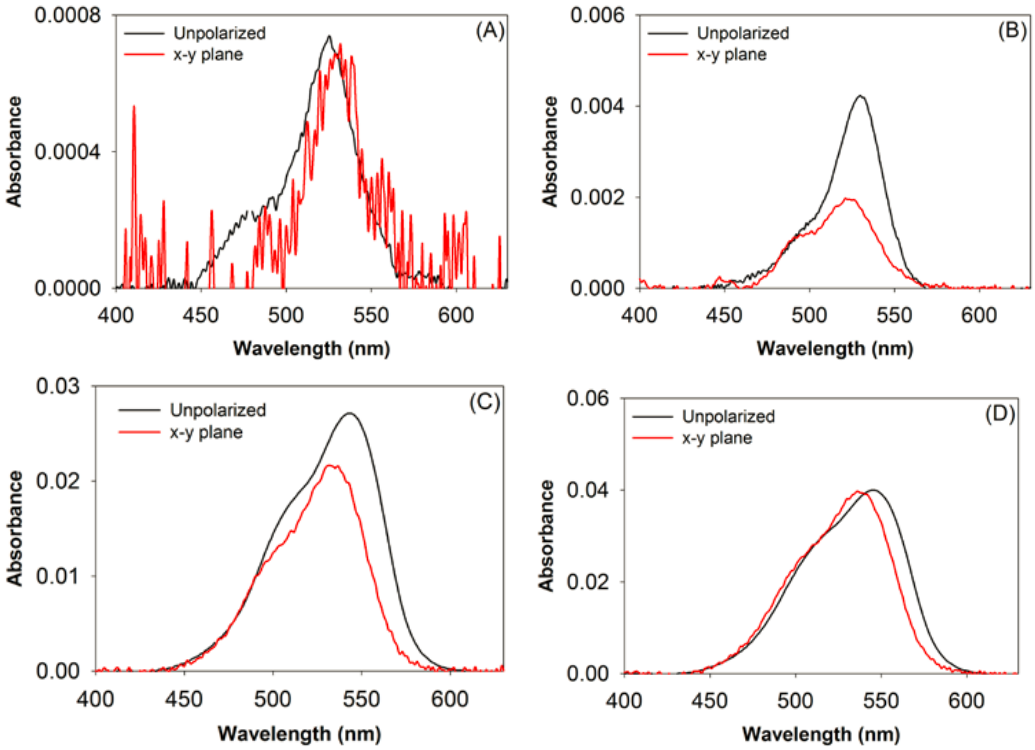

Figure 1-4. Absorption spectra using unpolarized light (black) and light polarized in the plane of the substrate (x-y). Film thicknesses: (A) 0.7 nm; (B) 1.1 nm; (C) 1.4 nm; and (D) 2.1 nm.

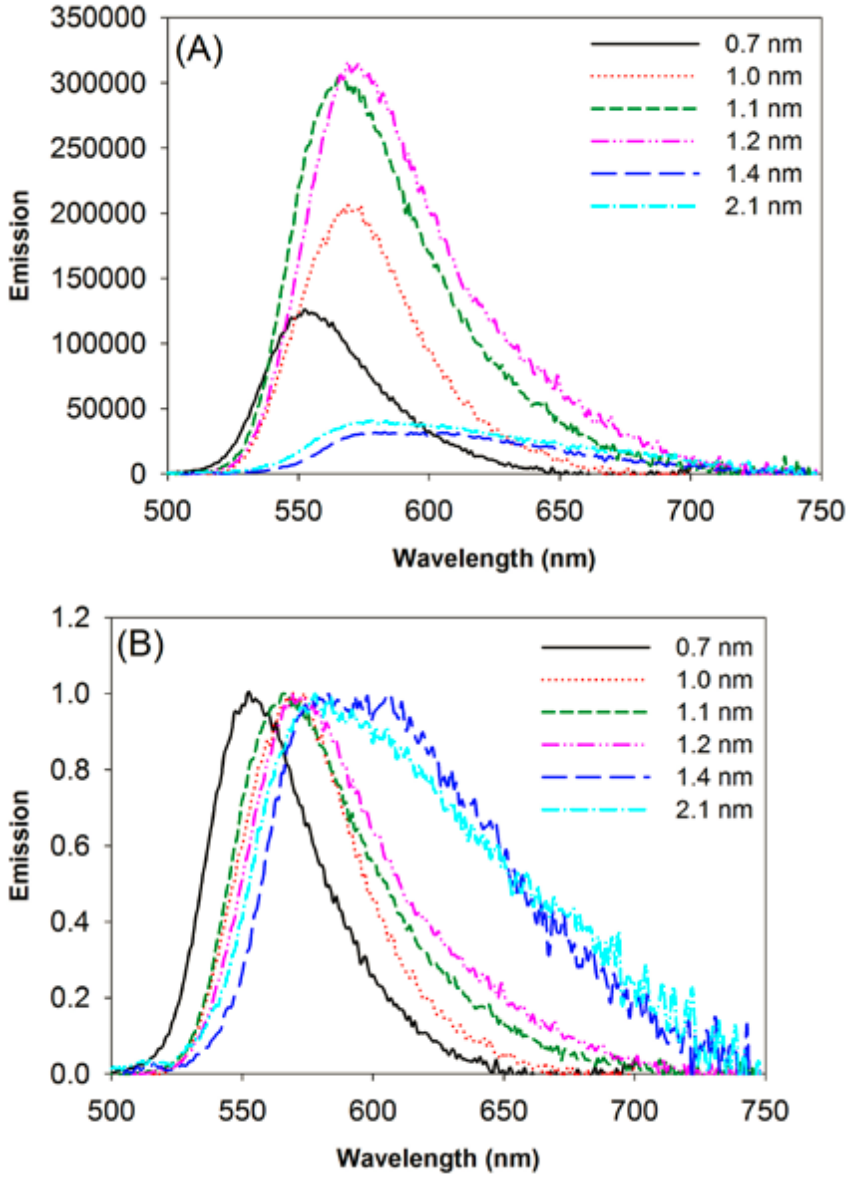

Figure 1-5. (A) Steady-state emission spectra and (B) normalized emission spectra for spin-cast Rh6G thin films as a function of film thickness: 0.7 nm; 1.0 nm; 1.1 nm; 1.2 nm; 1.4 nm; 2.1 nm.

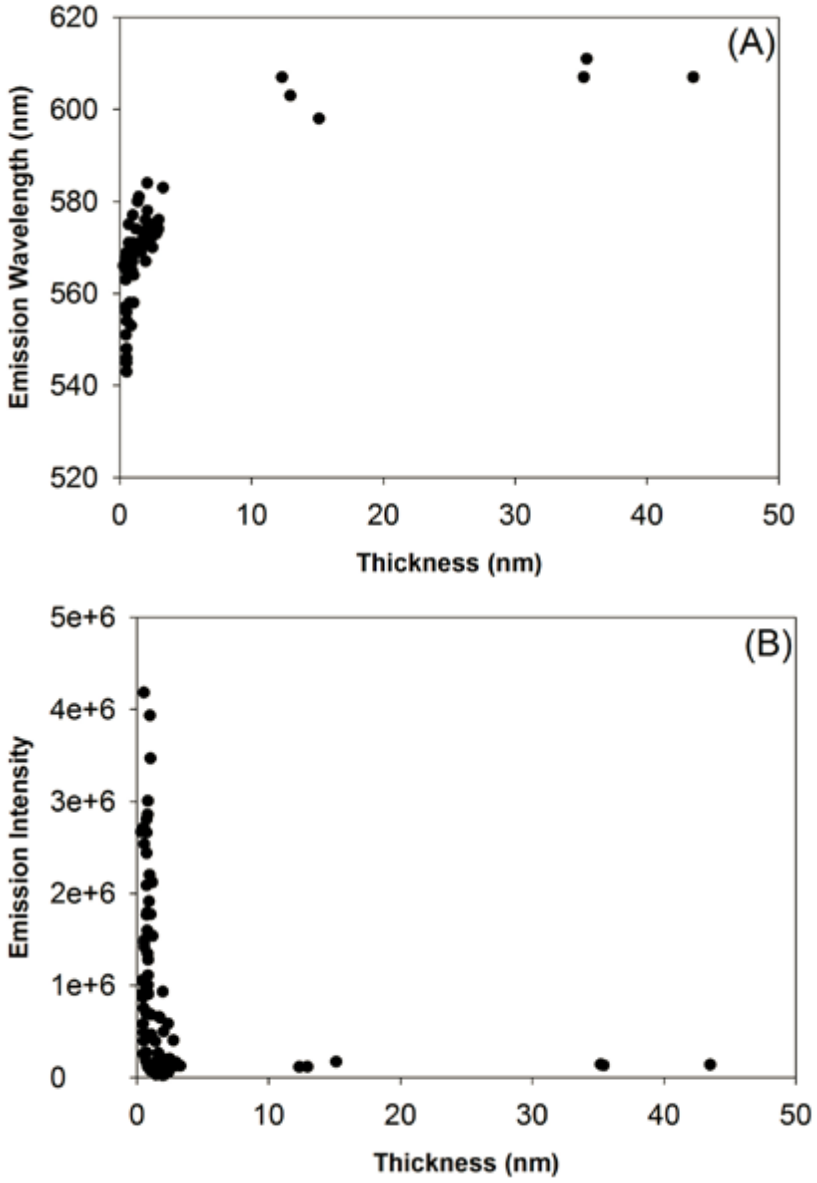

Figure 1-6. (A) Emission intensity changes, (B) emission wavelength maxima shifts as a function of Rh6G film thickness.

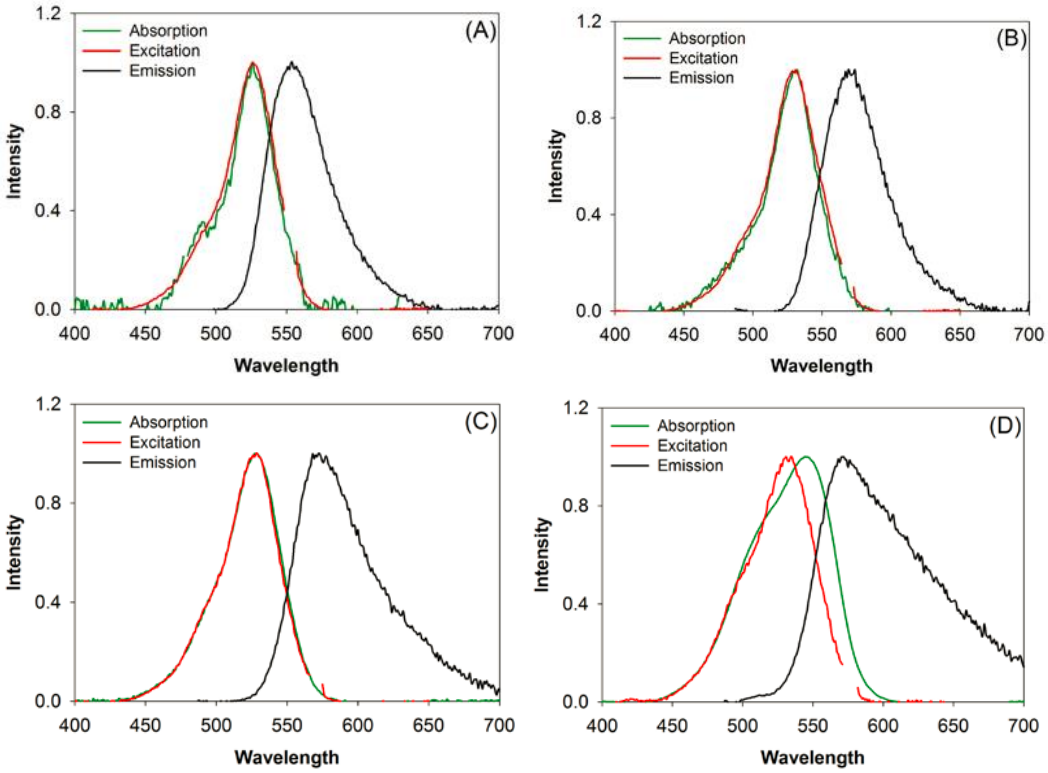

Figure 1-7. Normalized emission (green), excitation (red) and absorption (black) spectra of Rh6G: (A) t = 0.7 nm; (B) t = 1.0 nm; (C) t = 1.2 nm; (D) t = 2.1 nm thin film.

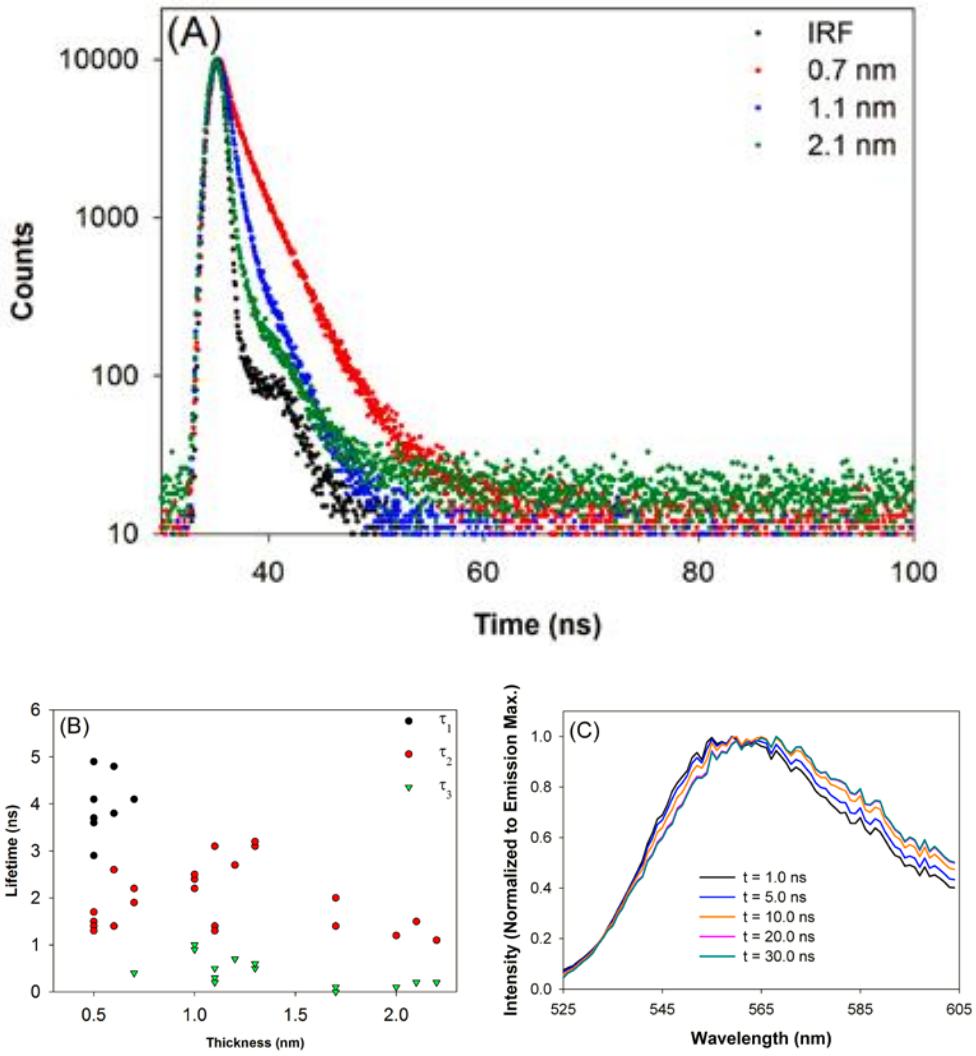

Figure 1-8. (A) Lifetime decay of 0.7 nm (red), 1.1 nm (blue), and 2.1 nm (green) thin films. (B) Lifetime as a function of film thickness, and (C) TRES of 1.1 nm Rh6G thin film at different times. All spectra are normalized at their corresponding peak maxima.

Thickness (nm)	τ1 (ns)	τ2 (ns)	τ3 (ns)	B1	B2	B3
0.5	3.6	1.5		0.13	0.87	
0.5	4.9	1.7		0.13	0.87	
0.5	4.1	1.5		0.10	0.90	
0.5	3.7	1.4		0.12	0.88	
0.5	2.9	1.3		0.17	0.83	
0.6	3.8	1.4		0.07	0.93	
0.6	4.8	2.6		0.32	0.68	
0.7	4.1	1.9		0.21	0.79	
0.7		2.2	0.4		0.44	0.56
1.0		2.2	1.0		0.54	0.46
1.0		2.4	0.9		0.33	0.67
1.0		2.5	0.9		0.39	0.61
1.1		3.1	0.5		0.14	0.86
1.1		1.4	0.3		0.11	0.89
1.1		1.3	0.2		0.06	0.94
1.2		2.7	0.7		0.27	0.73
1.3		3.1	0.5		0.12	0.88
1.3		3.2	0.6		0.15	0.85
1.7		2.0	0.1		0.06	0.94
1.7		1.4	0.0		0.06	0.94
2.0		1.2	0.1		0.16	0.84
2.1		1.5	0.2		0.21	0.79
2.2		1.1	0.2		0.19	0.81

Table 1-S1: Fluorescence lifetimes for a range of different thickness of Rh6G thin films on glass. All decay curves are 3-exponential fits:

$$I(t) = B_1 e^{-t/\tau_1} + B_2 e^{-t/\tau_2} + B_3 e^{-t/\tau_3}$$

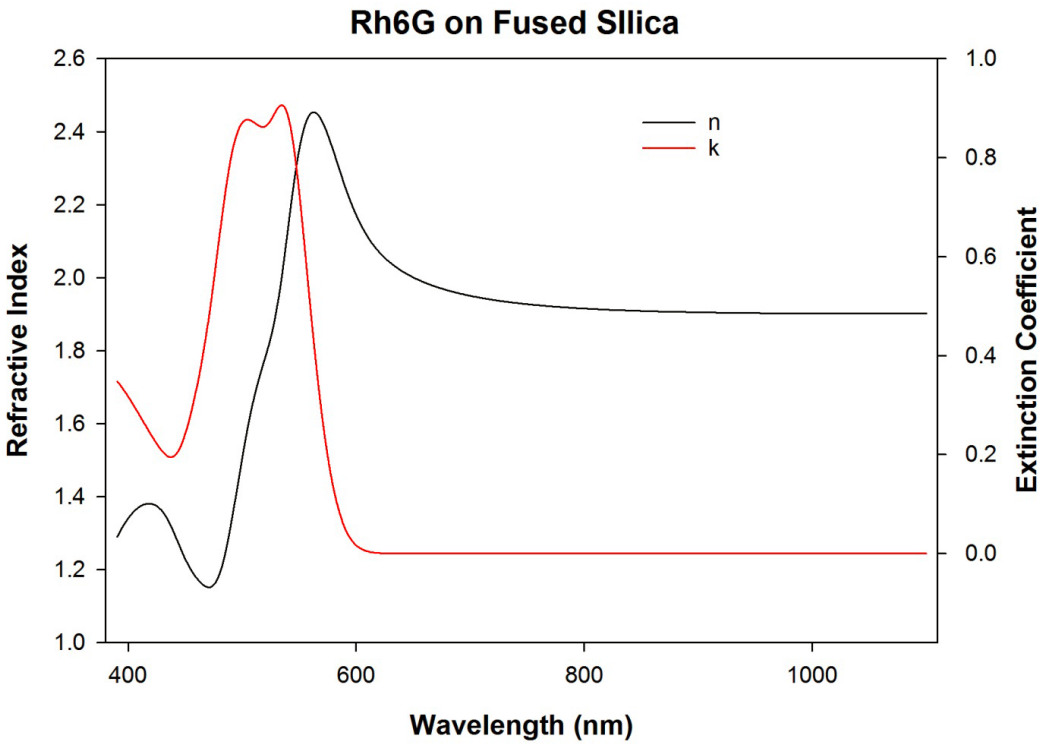

Figure 1-S1. Refractive index and extinction coefficient for Rh6G on fused silica. These provided the parameters used to determine thickness.

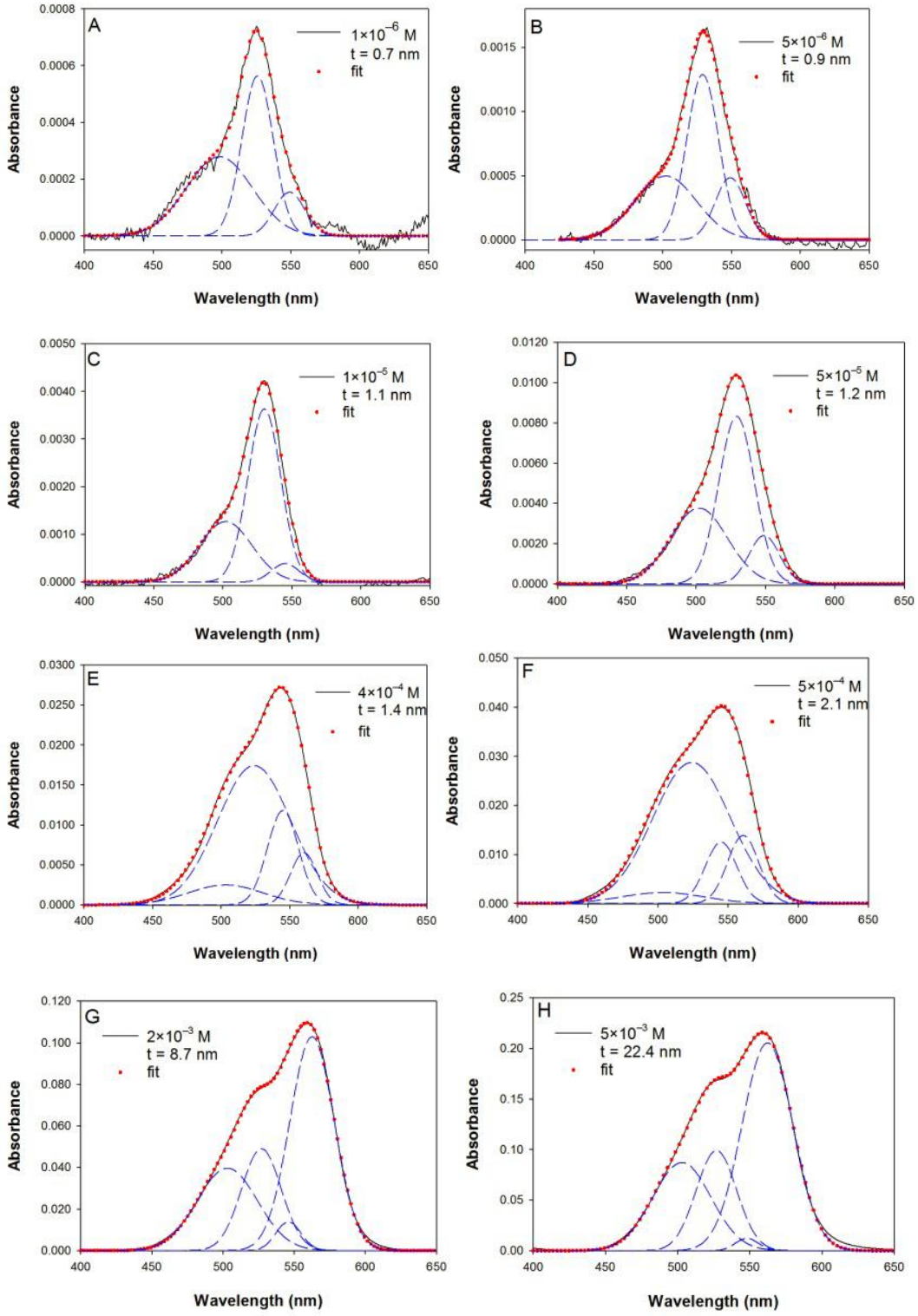

Figure 1-S2. The representative absorbance fits for several thicknesses/concentrations by using the parameters given in table 1-S1

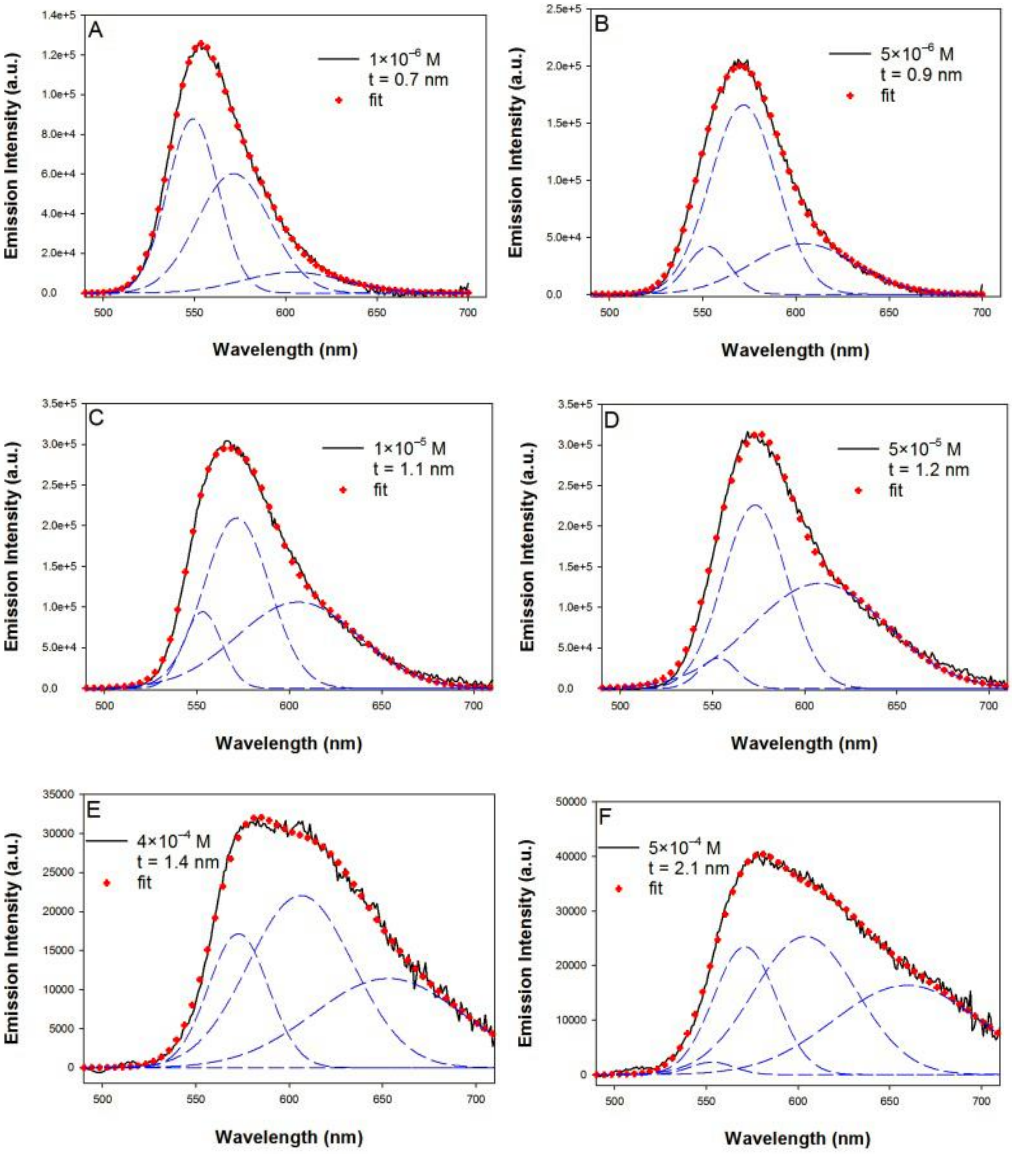

Figure 1-S3. The representative emission fits for several thicknesses/concentrations by using the parameters given in table 1-S1.

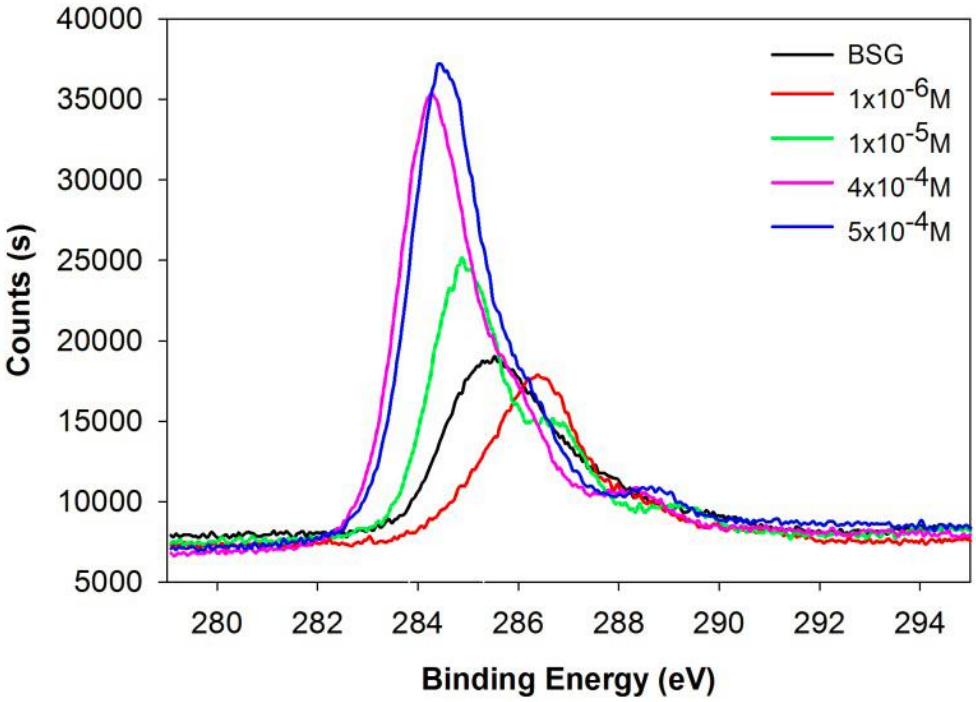

Figure 1-S4. The binding energy shifts for carbon as a function of thin film thickness/concentration. $1x10^{-6}$ M, 0.7nm; $1x10^{-5}$ M, 1.1 nm; $4x10^{-4}$ M, 1.4 nm; and $5x10^{-4}$ M, 2.1 nm. BSG = borosilicate glass.

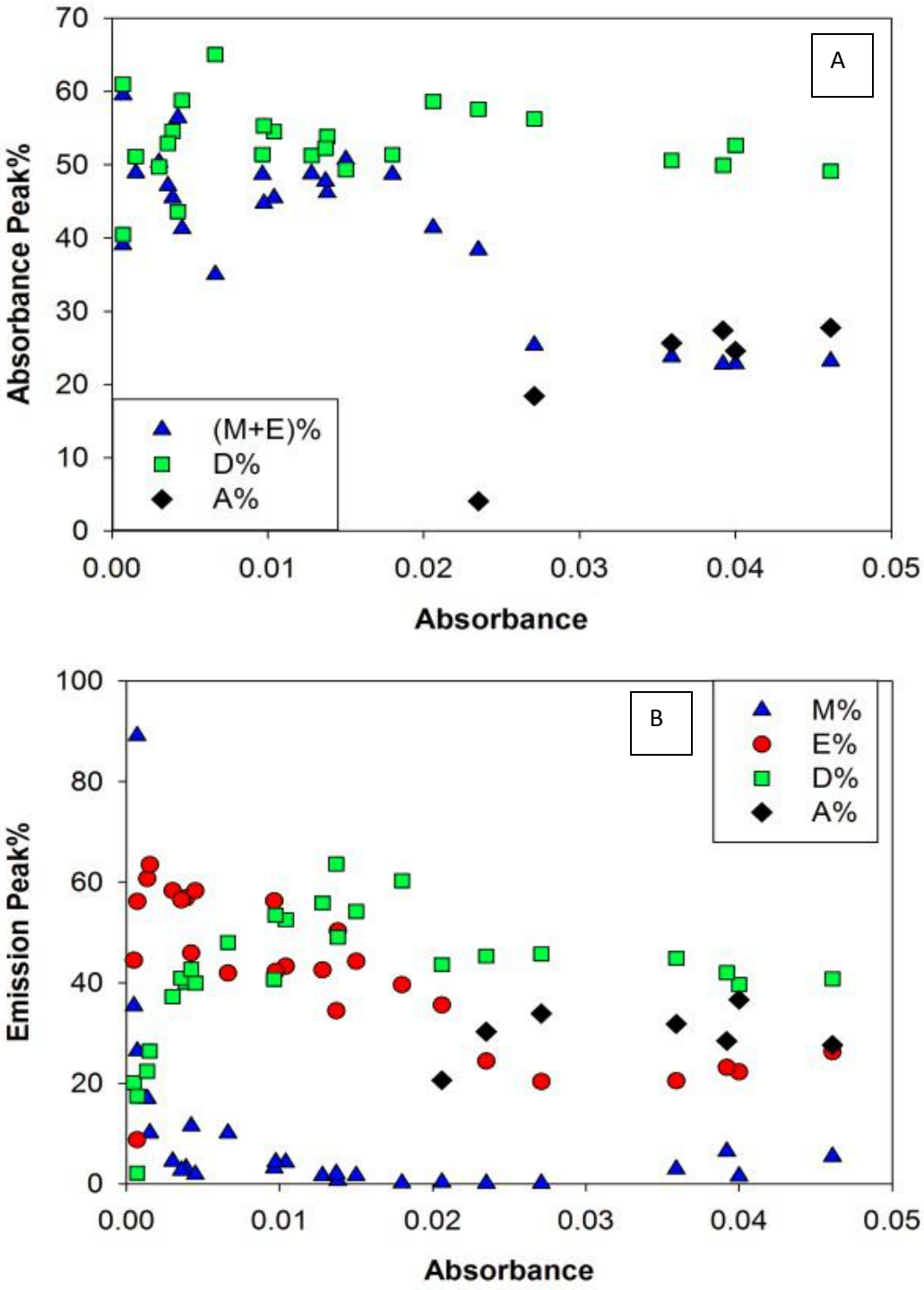

Figure 1-S5. Thin films structure composition with different thicknesses/concentrations according to deconvolution of (A) absorption spectra, and (B) emission spectra. M stands for monomer, E stands for excimer, D stands for oblique dimer, and A stands for crystalline structure/large aggregate.

MANUSCRIPT – II

Prepared for submission to the Journal of Physical Chemistry C

Study of Rhodamine 6G Structures in Different Solvent Systems

Mingyu Chapman and William B. Euler

Chemistry, University of Rhode Island, Kingston, RI, USA

Corresponding Author: William B. Euler, Ph.D.

Chemistry

University of Rhode Island

140 Flagg Road

Kingston, RI, 02881, USA

Email address: wueler@chm.uri.edu

CHAPTER 2

ABSTRACT

Rhodamine 6G (Rh6G) tends to form aggregates at higher concentrations; the presence of aggregates leads to strong fluorescence quenching. Therefore, understanding and controlling the state of aggregation of the dye molecules is of great interest. A series of solvents, differing in polarity were utilized to investigate Rh6G at various concentrations, and they influence absorption, excitation and emission spectra, the observed spectrum are accounted for by monomer, excimer, dimer, and excited state exciplex formation. The size of monomer and dimer measured by light scattering to be 1.4 ± 0.2 nm and 3.3 ± 0.6 nm.

INTRODUCTION

Rhodamine 6G is a well-known dye for fluorescence application due to its strong emission. Rh6G tends to self-aggregate at higher concentrations.[1,2] This could induce dramatic color changes, that is, changes of the extinction coefficient.[3,4] It could also modify the absorption characteristics such as spectral shifts and band splitting.[5–7] Moreover, the fluorescence quantum yield and decay time could also be decreased.[8–10]

The first stage of the dye aggregation should be the formation of a dimer, but further increases in the dye concentration would lead to the formation of high-order aggregates.[11–13] In order to form the simplest aggregate, a dimer, the dye-dye interaction must be strong enough to overcome any other forces that would favor solvation of a monomer.[14,15] Hydrogen bonding and hydrophobic interactions are the possible binding mechanism between Rh6G aggregates.[16–18] Therefore, the formation of aggregates is influenced by the hydrophobicity of the environment and the electrostatic interaction of the dye molecules.[13,17–20]

The exciton theory suggests when dimerization occurs, the two-excited states split.[19,21,22] The relative orientation of the transition moment vector of the monomeric unit in the aggregate affects the energy gap and the transition probabilities from the ground to excited states.[5,11,19,22–24] A blue shift (relative to the monomer peak) is characteristic of an H-dimer, while a red shift is assigned to a J-dimer.[9,22–24] An H-dimer is non emissive and normally associated with a

sandwich type structure, and a J-dimer is emissive and is a head-to-tail linear structure.[9,22–24]

An electronically excited monomer tends to form dimers with an adjacent ground state monomer at higher concentration, forming a electronically excited state dimer and is called an excimer.[25–28] The fluorescent quantum yield decreases at high concentration, but the absorption spectrum will not change since there is no ground state association.[29–32] Similarly, a complex formed between an excited state monomer and a ground state molecule of a different nature is called an exciplex.[33–35]

As previously reported, Rh6G thin films were spin cast onto a glass substrate using ethanol (EtOH) as a solvent.[36] The thickness of the Rh6G film was controlled by the concentration of the casting solutions, surface coverage and dye density on the surface.[36] At extremely low dye density, when the surface coverage is low, monomeric structure is dominant, excited state excimer and exciton dimer formation is also found in most of the Rh6G molecules have a near by neighbor. Further increase in surface coverage and dye density, additional layer of Rh6G forms and aggregated Rh6G grow until eventually the aggregated Rh6G dominates the structure.[30,36–41] Theoretically, the behavior of Rh6G molecules in solution could be similar as in the solid, changing from monomeric unit to aggregates as a function of dye density.[36–41]

The purpose of this study is to investigate the structure of Rh6G molecules in different solvents at different concentrations. A series of 5 different solvents

(acetone, acetonitrile (CH_3CN), dimethylformamide (DMF), ethanol (EtOH) and water) were studied. A wide range of concentrations was studied. The transition from primarily monomers to aggregate was abrupt in pure solvents. Thus, a mixed solvent system of EtOH/Water was used to better control particle growth.

EXPERIMENTAL SECTION

Rhodamine 6G chloride (Rh6G) was supplied by Acros Organics and was used without further purification. Dye solutions were prepared with a range of concentration from 1×10^{-7} M to 1×10^{-2} M in all solvents. acetone, acetonitrile (CH_3CN), dimethylformamide (DMF), Ethanol (etOH), all with purity >99%, were purchased from Sigma Aldrich or Fisher Scientific and used without further purification. Reverse osmosis purified water was obtained from the University of Rhode Island, Department of Chemistry.

The absorption spectra were obtained using a Perkin Elmer Lambda 1050 spectrometer. The slit width was set to 2 nm for low concentration solutions, and 0.1 nm for high concentration solutions, the wavelength range was set from 700 nm to 350 nm, and the integration time was set to 5 s for samples made with concentrations lower than 1×10^{-4} M, 0.2 s for samples made with concentrations above 1×10^{-4} M, the cuvette pathlength was 1 mm for concentrations lower than 1×10^{-5} M, and 0.1 mm pathlength cuvette was used for concentrations higher than 1×10^{-5} M. All spectra were baseline corrected by automatic baseline subtraction with PeakFit v4.12 software.

The fluorescence emission spectra and excitation spectra was acquired using a Horiba (Jobin Yvon) Fluorolog spectrometer. The light source used was a Xenon arc lamp. For emission spectra, the excitation wavelength was set at the absorbance maximum, the slit width was set to 2 nm for low concentration

solutions, and 0.1 nm for high concentration solutions, the wavelength range was set from 700 nm to 350 nm, the cuvette pathlength was 1 mm for concentrations lower than 1×10^{-5} M, and 0.1 mm pathlength cuvette was used for concentrations higher than 1×10^{-5} M. For excitation spectra, the detection wavelengths used were 550 nm, 570 nm, 600 nm, and the maximum emission wavelength.

Number weighted size distribution, volume weighted size distribution, and intensity weighted size distributions were obtained by dynamic light scattering using a Malvern Zetasizer Nano instrument. Scattering optics were set at 90 degree with the cuvette temperature set at 20°C, the integration time was automatically set to get a good signal-to-noise ratio, every measurement were performed after 2 minutes waiting time to allow solutions to be at rest, and every measurement was repeated 10 times.

RESULTS AND DISCUSSION

Solvent and Concentration effects. Figure 2-1 displays the absorption and emission spectra of Rh6G dissolved in each separate organic solvent and water. The solvents have different polarities: acetone (0.355), Dimethylformamide (0.386), acetonitrile (0.460), ethanol (0.654), and water (1).

Figure 2-1A and 2-1C are the normalized absorbance and emission spectra for low Rh6G concentration, the spectra differ in terms of peak wavelength, and the normalized general spectral shapes are virtually identical. At this concentration, there is minimal solvent influence on the molecular structure and the fluorescence process. Small deviations in the location of peak maxima can be attributed to the effects that solvents of differing polarity have on Rh6G molecule solvation.

Rh6G molecules tend to form aggregates at increased concentrations. As shown in Figure 2-1B, increasing total dye concentration leads to an increase in the absorption intensity of the high energy shoulder. The shoulder peak intensity is clearer in water, the absorbance maximum peak shift from 530 nm to 500 nm. At the same time, the fluorescence spectra change their shape in the high concentration solution. The emission peak shifted to the lower energy side and emission at long-wavelength region appeared. At this concentration, aggregate formation is favored in the presence of water.

In order to analyze the emission spectra more quantitatively, emission peak wavelength and intensity are plotted as a function of Rh6G concentration in Figure 2-2A and 2B, respectively. As stated in the previous paper, as dye density and surface coverage increases, Rhodamine 6G forms excited state excimer, which absorbs at 525 nm and has

an emission at 570 nm; further increases in concentration result in dimer formation with an emission peak wavelength at 600 nm.

Of interest within Figure 2-2A is that at concentration below 1 x 10^{-5} M, the peak wavelength is virtually constant for all five solvents, and are below 560 nm. This indicates that the Rh6G molecules are truly isolated and solvated in this regime. The peak wavelength continuously increases with increasing concentration to 1 x 10^{-4} M in all five solvents, indicating there are noticeable contributions from excited state excimer or dimers in this concentration region, but the peak wavelength is still dominated by the monomeric fluorescence structure as it is below 570 nm. In water, there is a huge jump in the peak wavelength from 1 x 10^{-4} M to 1 x 10^{-3} M, and the dominating peak changes from 560 nm to 610 nm, indicating the dominating structure changes from monomer to aggregates.

In general, as concentration increases, the emission intensity increases if no aggregation occurs. Such as for ethanol solvent, the emission intensity only reaches a maximum at 1 x 10^{-3} M as shown in Figure 2-2B. But for water, it reveals a maximum intensity around 5 x 10^{-5}, and intensity decreases when going to higher or lower Rh6G concentrations. The alkyl groups of Rh6G dye are hydrophobic in nature, and therefore they prefer to aggregate in water. On the other hand, ethanol can solvate the Rh6G molecule extensively at different places, such as the methyl, and ethylamine group, and oxygen, so the aggregation of Rh6G occurs at much higher concentration than in water.

Water and ethanol were chosen to study the aggregation process in detail as follows.

Aggregation Study in Water, Ethanol and Water-Ethanol binary Solvents. For both Rh6G in ethanol and water, the absorbance spectra consist of a 530 nm main peak and a small shoulder peak around 500 nm as shown in Figure 2-3. The absorbance spectra shape did not change with increasing concentration in ethanol. But in water, the 500 nm peak slowly increases with increasing dye concentration.

As shown in Figure 2-4, the absorbance spectra of a 1 x 10^{-3} M Rh6G is observed in a binary of ethanol and water with solvent:solvent ratios ranging from 10:0 to 0:10 respectively. Observing the spectra of pure ethanol with increasing fractions of water, the 500 nm peak slowly increases at the expense of the 530 nm peak, which results in the emergence of an isosbestic point at 508 nm. The presence of this isosbestic point indicates that only two species are present in the solutions, which are attributed to a monomer and the first order aggregate, a dimer. The absorbance shape of the dimer has the maximum 500 nm peak with a large 530 shoulder.

The size of Rh6G molecules in ethanol and water was measured and the size distribution by volume and intensity was shown in Figure 2-5 and Figure 2-6. In the volume distribution, the area of the peak is depending on the volume of the particle (volume of a particle sphere is equal to $4/3\pi(r)^3$), and is proportional to the 3rd power of its diameter[42,43]. In intensity distribution, the area of the peak is proportional to the sixth power of its diameter from Rayleigh's approximation. The size distribution was much wider in water compared to in ethanol[42,43].

In ethanol, the size distribution shows the size of molecule was ranging from 0.8 to 3 nm, with the two similar peaks at 0.8 ± 0.2 nm and 1.5 ± 0.2 nm. The average size calculated based on the volume is 1.4 ± 0.6 nm, and the average size calculated based on the intensity is 1.4 ± 0.6 nm. The hydrogen bonds between ethanol and alkyl amine group

could possibly keep the solvent molecules nearly parallel to the planar xanthene ring, making the stacking of the monomers difficult, so the average molecule size in ethanol should be in the monomeric unit range, as shown in Figure 2-7, the size of one monomeric unit is calculated based on the bond angles and bond length by using Chemdraw program, and is between 0.7 nm – 1.4 nm depending on the direction of the measurement.

While in water the size was ranging from 0.8 nm to 6 nm, with major peak at 3.25 ± 0.6 nm and a much smaller peak at 1.4 ± 0.2 nm. The average size calculated based on volume is 3.03 ± 0.3 nm, and the average size calculated based on the intensity is 3.3 ± 0.3 nm. At high concentration, the Rh6G molecules arrange themselves in dimer or larger aggregates. In dimer, two structures can be found. Sandwich structure (H-type dimer), in which the xanthene rings are in parallel planes with a twist angle. Linear configuration (J-type dimer), where the xanthene rings is in the same plane. Due to the hydrophobic character of the xanthene ring, the parallel plane is more favored in water in order to avoid the solvating water molecule, so the H-type dimer is energetically favored.

The absorption spectra were deconvoluted into the component parts, only four peaks were required to fit the observed spectra. The absorption maxima and the line widths are given in Table 2-1.

In monomeric solution, peak 1 at 508 nm and peak 2 at 531 nm are required to fit the spectra that account for vibronic shoulder and monomeric absorbance peak. The ratio between these two peaks are 509 nm / 531 nm = 0.88.

As formation of dimer starts, the 531 nm peak slowly decreases, with formation of new peaks at 499 nm and 508 nm. The 499 nm peak dominates in the most concentrated Rh6G in water.

A particularly interesting feature is the change of band shape of the fluorescence emission for 1 x 10^{-3} M Rh6G in water, and this is due to detector saturation. The emission spectra can no longer be obtained at this concentration.

As shown in Figure 2-8, at concentrations lower than this 1 x 10^{-4} M, the emission band shapes of water and ethanol samples are very similar. However, the shapes of emission spectra are the same but with small shift to the lower energy side. This emission peak shift to the lower energy side is due to vibronic coupling. The emission spectra were deconvoluted into the component parts, the emission maxima and the line widths are given in Table 2-2.

At low concentration, majority of Rh6G are in the solvated monomeric state, have the absorbance peak at 531 nm and small shoulder at 508 nm. In the excitation spectra, there is a major peak at 531 nm, and smaller peak at 508 nm in excitation spectra, the absorption and excitation spectra superimpose as shown in Figure 2-9. Emission spectra consists of 4 peaks as shown in Table 2-2, have the same line width and with similar energy gap in between, which can be the result of vibronic coupling.

The enlarged Frank-Condon shifts allow explain this observed shape of the dimer absorption and emission cross-section spectra as shown in Figure 2-10. Due to the binding energy between two molecules, the potential energy surfaces are lowered compared to the monomer. The energy levels of both molecules in the dimer are somewhat different due to the mutual interaction. The Frank-Condon shifts of both

molecules are also assumed to be larger than the Frank-Condon shift of an undisturbed monomer.

In general, the formation of dimer has been investigated through study of Rh6G thin film on glass substrate in our previous paper. At low Rh6G concentration, most dye molecules are isolated from each other and fully solvated, hence the emission band is around 560 nm. As the concentration increases, the emission maxima wavelength shift to the low energy side, the excited state excimer started to form, resulting in the emission shift to 580 nm. The 584 nm emission peak in solution increases as concentration increases, is assigned to be the excited state Rh6G excimer. The weak emission at 620 nm can be attributed by large size exciplex in the solution. Increase in concentration greatly affects the excited state excimer formation, but the excited state exciplex is less concentration depended as shown in Figure 2-11.

The monomeric emission decreases as the concentration goes up as a result of formation of dimer, the 499 nm absorbance peak is associated with the dimer absorbance, and it is non emissive, which means it is a H-type dimer.

CONCLUSION

In this work, the solvent and concentration effects in the absorption and fluorescence spectra of the Rh6G were studied. A full Rh6G concentration range in five different solvents, from the solubility limit to highly dilute systems, was studied in detail. A very small change of the spectrum was observed in all solvents at low concentration. When the dye concentration increases in water, a significant change is observed in both absorption and emission.

A careful analysis of the spectra revealed the formation of molecular dimers at high concentration. This is indicated by the appearance of a second absorbance spectral band, which is red-shifted with respect to the fully solvated, isolated monomers. The formation of dimer is also studied by the size change from monomeric dominating solution to dimer dominating solution. It shows that the monomeric unit has an average size of 1.0 ± 0.2 nm, and average size of 3.25 ± 0.6 nm for the dimer dominated solution. The ratio of monomer to dimer structure can be altered either by increasing the concentration in water, or increasing the water solvent ratio in the mixed solvent, and this provides the tunability between 550 nm to 610 nm for emission wavelength. The type of dimer formed in water is H-type non-emissive dimer. Excited state excimer and excited

state exciplex which emits at 584 nm and 620 respectfully, were identified in the monomeric solution.

ACKNOWLEDGEMENT

This material is based upon work supported by the U.S. Department of Homeland Security, Science and Technology Directorate, Office of University Programs, under Grant Award 2013-ST-061-ED0001. The views and conclusions contained in this document are those of the authors and should not be interpreted as necessarily representing the official policies, either expressed or implied, of the U.S. Department of Homeland Security.

LIST OF REFERENCES

(1) Zehentbauer, F. M.; Moretto, C.; Stephen, R.; Thevar, T.; Gilchrist, J. R.; Pokrajac, D.; Richard, K. L.; Kiefer, J. Fluorescence Spectroscopy of Rhodamine 6G: Concentration and Solvent Effects. *Spectrochim. Acta - Part A Mol. Biomol. Spectrosc*. **2014**, *121*, 147–151.

(2) Hildebrandt, P.; Stockburger, M. Surface-Enhanced Resonance Raman Spectroscopy of Rhodamine 6G Adsorbed on Colloidal Silver. *J. Phys. Chem.* **1984**, *88* (24), 5935–5944.

(3) Penzkofer, A.; Lu, Y. Fluorescence Quenching of Rhodamine 6g in Methanol at High Concentration. *Chem. Phys.* **1986**, *103*, 399–405.

(4) Lu, Y.; Penzkofer, A. Absorption Behaviour of Methanolic Rhodamine 6G Solutions at High Concentration. *Chem. Phys*. **1986**, *107* (2–3), 175–184.

(5) Liu, T.; Yu, A.; Luo, G.; Zhao, X.; Ying, L.; Huang, Y.; Huang, C. Aggregates in Rhodamine-Labeled Phospholipid Films Probed by Spectroscopy and Atomic Force Microscopy. *Acta Physico-Chimica Sin.* **2000**, *16* (1), 49–53.

(6) Martínez, V. M.; Arbeloa, F. L.; Prieto, J. B.; Arbeloa, I. L. Characterization of Rhodamine 6G Aggregates Intercalated in Solid Thin Films of Laponite Clay. 2 Fluorescence Spectroscopy. *J. Phys. Chem. B* **2005**, *109* (15), 7443–7450.

(7) Yamagata, H.; Maxwell, D. S.; Fan, J.; Kittilstved, K. R.; Briseno, a L.; Barnes, M. D.; Spano, F. C. HJ-Aggregate Behaviour of Crystalline 7,8,15,16-Tetraazaterrylene: Introducing a New Design Paradigm for Organic Materials. *J. Physic* **2014**, *118*, 28842–28854.

(8) Kazakevičius, A.; Peckus, D.; Boiko, O.; Valkunas, L.; Leonenko, E.; Telbiz, G.; Gulbinas, V. Insights into the Mechanism of Enhanced Rhodamine 6G Dimer Fluorescence in Mesoscopic Pluronic-Silica Matrixes. *J. Phys. Chem. C* **2015**, *119* (33), 19126–19133.

(9) Fita, P.; Fedoseeva, M.; Vauthey, E. Hydrogen-Bond-Assisted Excited-State Deactivation at Liquid / Water Interfaces. *Langmuir* **2011**, *27*, 4645–4652.

(10) Penzkofer, A.; Leupacher, W. Fluorescence Behaviour of Highly Concentrated Rhodamine 6G Solutions. *J. Lumin.* **1987**, *37*, 61–72.

(11) Zhao, J.; Jensen, L.; Sung, J.; Zou, S.; Schatz, G. C.; Van Duyne, R. P. Interaction of Plasmon and Molecular Resonances for Rhodamine 6G Adsorbed on Silver Nanoparticles. *J. Am. Chem. Soc.* **2007**, *129* (24), 7647–7656.

(12) Yuan, Q.; Zhang, X.; Wang, Z.; Shibraen, M. H. M. A.; Yang, S.; Xu, J. Dimerization of Rhodamine B in Alumina Sol and Corresponding Dip-Coated Film. *Colloids Surfaces A Physicochem. Eng. Asp.* **2015**, *486*, 139–144.

(13) Gilani, A. G.; Sariri, R.; Bahrpaima, K. Aggregate Formation of Rhodamine 6G in Anisotropic Solvents. *Spectrochim. Acta - Part A Mol. Biomol. Spectrosc.* **2001**, *57* (1), 155–161.

(14) Kemnitz, K.; Yoshihara, K. Entropy-Driven Dimerization of Xanthene Dyes in Nonpolar Solution and Temperature-Dependent Fluorescence Decay of Dimers. *J. Phys. Chem.* **1991**, *95* (16), 6095–6104.

(15) Synak, A.; Kułak, L.; Rangełowa-Jankowska, S.; Grobelna, B.; Kubicki, A.; Bojarski, P. Reversible Energy Transfer between Monomers and Fluorescent Dimers of Rhodamine S in Polyvinyl Alcohol Films. *Chem. Phys.* **2011**, *382* (1–3), 47–51.

(16) Malfatti, L.; Kidchob, T.; Aiello, D.; Aiello, R.; Testa, F.; Innocenzi, P. Aggregation States of Rhodamine 6G in Mesostructured Silica Films. *J. Phys. Chem. C* **2008**, *112* (42), 16225–16230.

(17) Kunjappu, J. O. Y. T.; Manohar, C. Aggregagtion Characteristics of Laser Dye Rhodamine 6G in Aqueous Surfactant Solutions. **1990**, *52* (4), 717–721.

(18) Lofaj, M.; Valent, I.; Bujdak, J. Mechanism of Rhodamine 6G Molecular Aggregation in Montmorillonite Colloid. *Cent. Eur. J. Chem* **2013**, *11* (10), 1606–1619.

(19) Ojeda, P. R.; Amashta, I. a. K.; Ochoa, J. R.; Arbeloa, I. L. Excitonic Treatment and Bonding of Aggregates of Rhodamine 6G in Ethanol. *J. Chem. Soc. Faraday Trans. 2* **1988**, *84* (1), 1.

(20) Muntean, S. G.; Simu, G. M.; Kurunczi, L.; Szabadai, Z. Investigation of the Aggregation of Three Disazo Direct Dyes by UV-Vis Spectroscopy and Mathematical Analysis. *Rev.Chim* **2009**, *60* (2), 152–155.

(21) Vogel, R.; Meredith, P.; Harvey, M. D.; Rubinsztein-Dunlop, H. Absorption and Fluorescence Spectroscopy of Rhodamine 6G in Titanium Dioxide Nanocomposites. *Spectrochim. Acta - Part A Mol. Biomol. Spectrosc.* **2004**, *60* (1–2), 245–249.

(22) Kasha, M.; Rawls, H. R.; Ashraf El-Bayoumi, M. The Exciton Model in Molecular Spectroscopy. *Pure Appl. Chem.* **1965**, *11*, 371–392.

(23) Anedda, a.; Carbonaro, C. M.; Corpino, R.; Ricci, P. C.; Grandi, S.; Mustarelli, P. C. Formation of Fluorescent Aggregates in Rhodamine 6G Doped Silica Glasses. *J. Non. Cryst. Solids* **2007**, *353* (5–7), 481–485.

(24) Tennakone, K.; Pitigala, P. K. D. D. P.; Perera, a. G. U. Exciton Transport and Electron Mobility of Organized Aggregates of Cationic Dye Thiocyanates. *RSC Adv.* **2013**, *3* (8), 2770.

(25) Khan, A. U.; Kasha, M. Mechanism of Four-Level Laser Action in Solution Excimer and Excited-State Proton-Transfer Cases. *Proc. Natl. Acad. Sci. USA* **1983**, *80* (6), 1767–1770.

(26) Birks, J. Excimers. *Rep. Prog. Phys* **1975**, *38*, 903–974.

(27) Claire, P. D. Sainte. Molecular Simulation of Excimer Fluorescence in Polystyrene and Poly (Vinylcarbazole). **2006**, 7334–7343.

(28) Ibnaouf, K. H. Excimer State of a Conjugated Polymer (MEH-PPV) in Thin Films. *Opt. Laser Technol*. **2013**, *48*, 401–404.

(29) Bains, G. K.; Kim, S. H.; Sorin, E. J.; Narayanaswami, V. The Extent of Pyrene Excimer Fluorescence Emission Is a Reflector of Distance and Flexibility: Analysis of the Segment Linking the LDL Receptor-Binding and Tetramerization Domains of Apolipoprotein E3. *Biochemistry* **2012**, *51* (31), 6207–6219.

(30) Yip, W. T.; Levy, D. H. Excimer / Exciplex Formation in van Der Waals Dimers of Aromatic Molecules. **1996**, *3654* (95), 11539–11545.

(31) Conlon, P.; Yang, C. J.; Wu, Y.; Chen, Y.; Martinez, K.; Kim, Y.; Stevens, N.; Marti, A.; Jockusch, S.; Turro, N.; et al. Pyrene Excimer Signaling Molecular Beacons for Probing Nucleic Acids. *J Am Chem Soc* **2009**, *130* (1), 336–342.

(32) Martinho, J. M. G.; SReis e Sousa, A. .; Oliveira Torres, M. E.; Fedorov, A. Fluorescence Quenching of Pyrene Monomer and Excimer by CH3I. *Chem. Phys.* **2001**, *264* (1), 111–121.

(33) Hui, M.; Ware, W. R. Exciplex Photophysics. IV. Effect of Diffusion-Controlled Quenching on Exciplex Photokinetics. **1976**, *144*, 4712–4717.

(34) Aroca, R.; Can, T. Del; Nb, O.; Saja, J. A. De. Exciplex Formation and Energy Transfer in Mixed Films of Phthalocyanine and Perylene Tetracarboxylic Diimide Derivatives. **2003**, *13*, 3012–3019.

(35) Stewart, D. J.; Dalton, M. J.; Swiger, R. N.; Cooper, T. M.; Haley, J. E.; Tan, L. Exciplex Formation in Blended Spin-Cast Films of Fluorene-Linked Dyes and Bisphthalimide Quenchers. **2013.**

(36) Chapman, M.; Mullen, M.; Novoa-Ortega, E.; Alhasani, M.; Elman, J. F.; Euler, W. B. Structural Evolution of Ultrathin Films of Rhodamine 6G on Glass. *J. Phys. Chem. C* **2016**, *120* (15), 8289–8297.

(37) Kalinowaki, J. Excimers and Exciplexes. **2009**, *27* (3).

(38) Son, M.; Park, K. H.; Shao, C.; Wu, F.; Kim, D. Spectroscopic Demonstration of Exciton Dynamics and Excimer Formation in a Sterically Controlled Perylene Bisimide Dimer Aggregate. *J. Phys. Chem. Lett.* **2014**, *5*, 3601–3607.

(39) Cho, D. W.; Cho, D. W. Excimer and Exciplex Emissions of 1,8-Naphthalimides Caused by Aggregation in Extremely Polar or Nonpolar Solvents. **2014**, 2233–2236.

(40) Noginov, M. a; Vondrova, M.; Williams, S. M.; Bahoura, M.; Gavrilenko, V. I.; Black, S. M.; Drachev, V. P.; Shalaev, V. M.; Sykes, a. Spectroscopic Studies of Liquid Solutions of R6G Laser Dye and Ag Nanoparticle Aggregates. *J. Opt. A Pure Appl. Opt.* **2005**, *7* (2), S219–S229.

(41) Ojeda, P. R.; Katime, I.; Ochoa, J. R.; López, I. Excitonic Treatment and Bonding of Aggregates of Rhodamine 6G in Ethanol. *J. Chem. Soc. Faraday Trans. 2* **1988**, *84*, 1–8.

(42) De Kanter, M.; Meyer-Kirschner, J.; Viell, J.; Mitsos, A.; Kather, M.; Pich, A.; Janzen, C. Enabling the Measurement of Particle Sizes in Stirred Colloidal Suspensions by Embedding Dynamic Light Scattering into an Automated Probe Head. *Meas. J. Int. Meas. Confed*. **2016**, 80, 92–98.

(43) Lorber, B.; Fischer, F.; Bailly, M.; Roy, H.; Kern, D. Protein Analysis by Dynamic Light Scattering: Methods and Techniques for Students. *Biochem. Mol. Biol. Educ.* **2012**, *40* (6), 372–382.

Peak	λ_{max} (nm)	Γ (nm)	[Rh6G] in Ethanol	[Rh6G] in Water	1 x 10^{-3} M ($EtOH : H_2O$)
1	508	26	1 x10^{-7} M – 1 x 10^{-3} M	1 x10^{-7} M – 1 x 10^{-5} M	10:0 – 3:7
2	531	12	1 x10^{-7} M – 1 x 10^{-3} M	1 x10^{-7} M – 1 x 10^{-3} M	10:0 – 0:10
3	508	32		1 x10^{-5} M – 1 x 10^{-3} M	2:8 – 0:10
4	499	11		1 x10^{-5} M – 1 x 10^{-3} M	2:8 – 0:10

Table 2-1. Deconvoluted peak composition (using a Gaussian Line Shape) for Absorption spectra as a function of concentration and solvent ratio. Peak position (λ_{max}) and FWHM (Γ) have an uncertainty of ± 2 nm.

Peak	λ_{max} (nm)	Γ (nm)	[Rh6G] in H_2O and EtOH
1	546	11	1 x10^{-7} M – 1 x 10^{-5} M
2	555	11	1 x10^{-7} M – 1 x 10^{-4} M
3	564	11	1 x10^{-7} M – 1 x 10^{-4} M
4	573	11	1 x10^{-7} M – 1 x 10^{-4} M
5	584	27	1 x10^{-7} M – 1 x 10^{-4} M
6	620	47	1 x10^{-7} M – 1 x 10^{-4} M

Table 2-2. Deconvoluted peak composition (using a Gaussian Line Shape) for emission spectra. Peak position (λ_{max}) and FWHM (Γ) have an uncertainty of ± 2 nm.

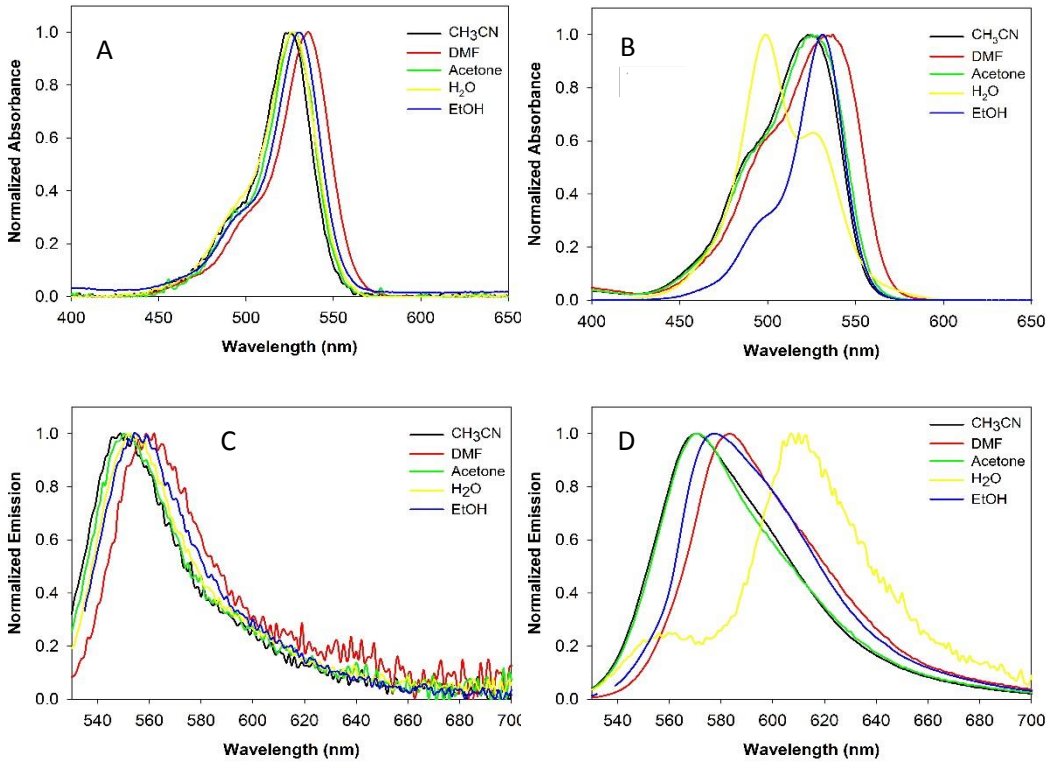

Figure 2-1. Normalized spectra of Rh6G in different solvents: (A) Absorption spectra at 1 x 10^{-7} M, (B) absorption spectra at 1 x 10^{-2} M, (C) Emission spectra at 1 x 10^{-7} M, and (D) Emission spectra at 1 x 10^{-2} M.

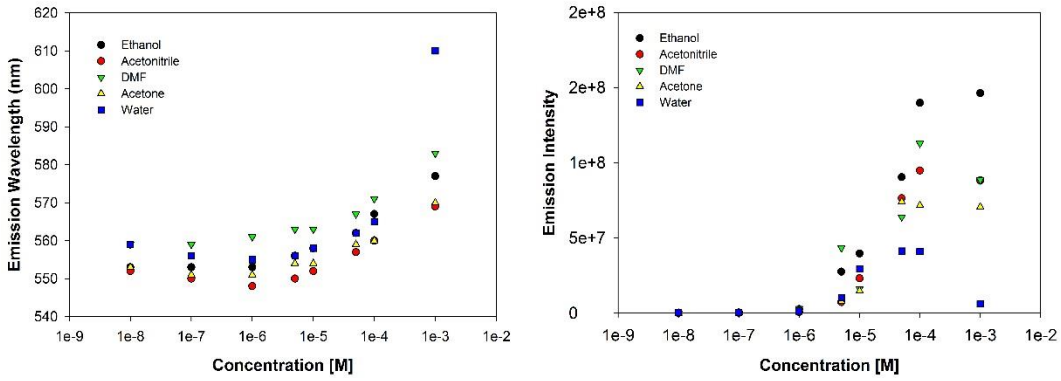

Figure 2-2. The change of (A) Emission peak wavelength, and (B) emission intensity as a function of Rh6G concentration in different solvents.

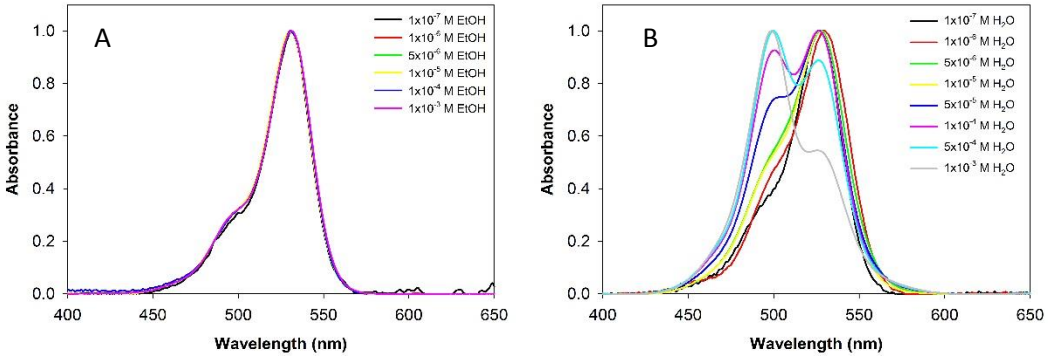

Figure 2-3. Normalized absorbance spectra for Rhodamine 6G dissolved in Ethanol (A) and in water (B).

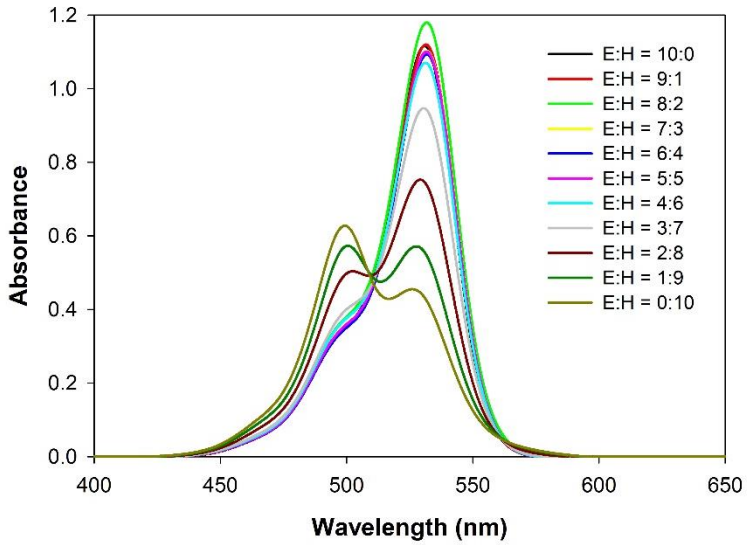

Figure 2-4: The absorption spectra to show solvent ratio (binary solution of Ethanol:Water) effect in $1x10^{-3}$ M Rh6G solution

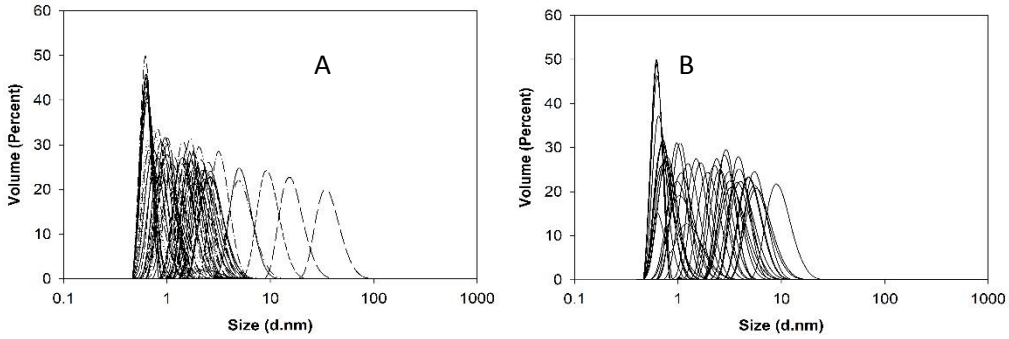

Figure 2-5. Molecule size distribution in terms of volume for 1 x 10^{-3} M Rh6G in (A) Ethanol, and (B) in Water

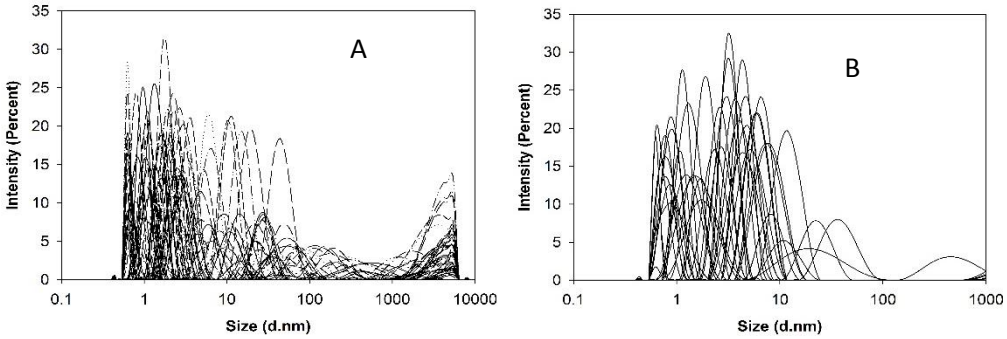

Figure 2-6. Molecule size distribution in term of intensity for 1 x 10^{-3} M Rh6G in (A) Ethanol, and (B) Water

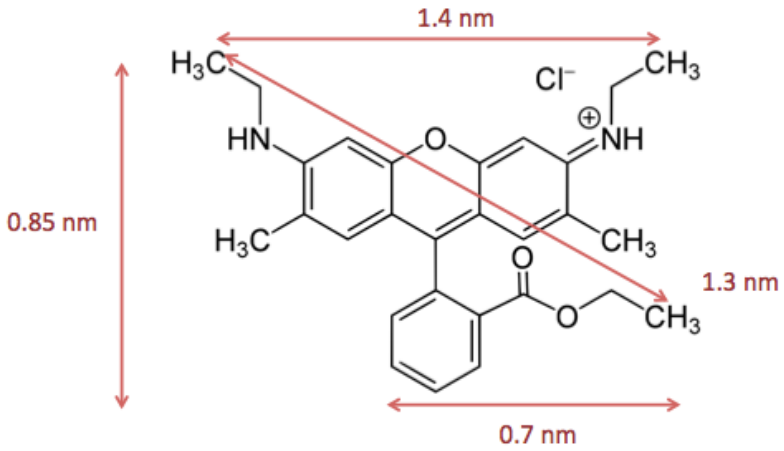

Figure 2-7. Molecular structure of the Rh6G monomer

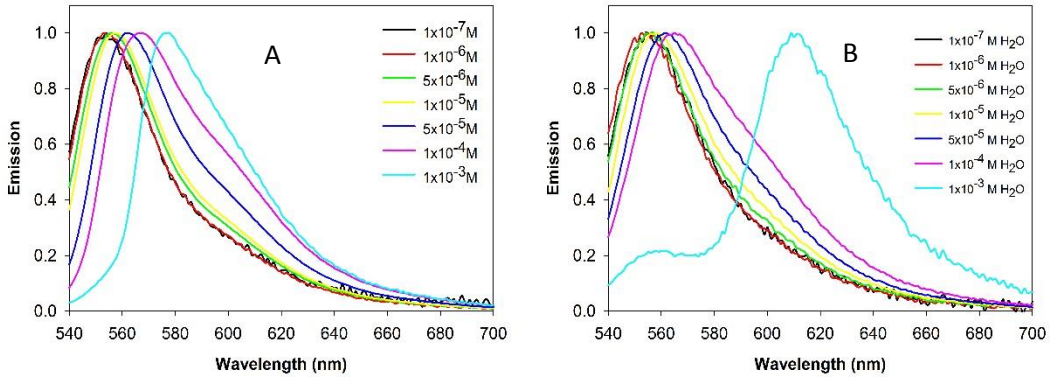

Figure 2-8. Emission spectra of Rhodamine 6G in Ethanol (A) and in Water (B)

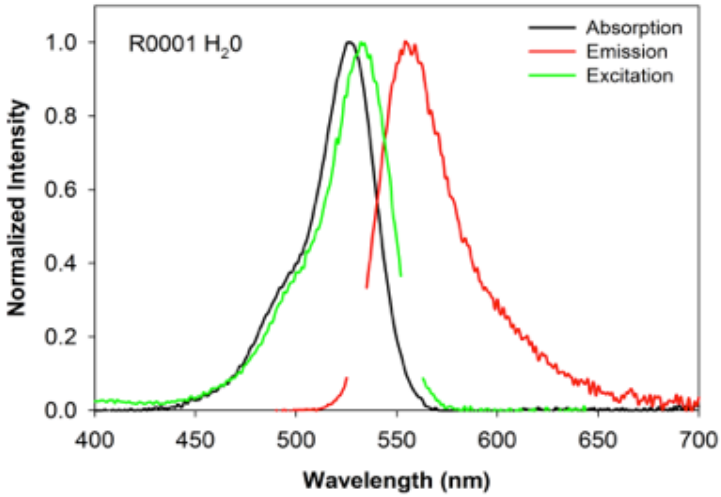

Figure 2-9. Normalized absorption (black), emission (red), and excitation (green) spectra of 1 x 10^{-7} M Rh6G in water

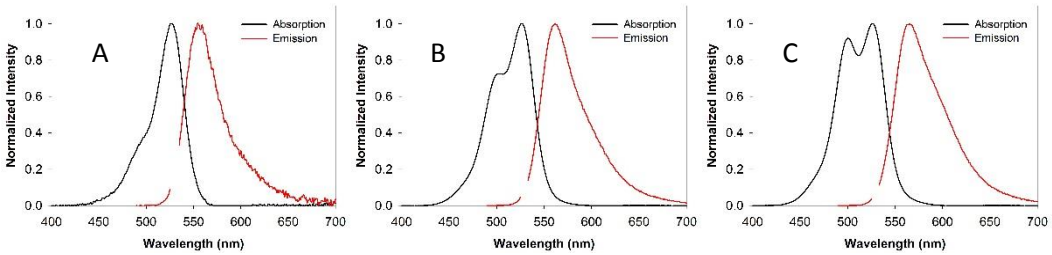

Figure 2-10. Normalized absorption (black) and emission (red) spectra for Rh6G in water at concentration (A) 1 x 10^{-7} M, (B) 5 x 10^{-5} M, and (C) 1 x 10^{-4} M.

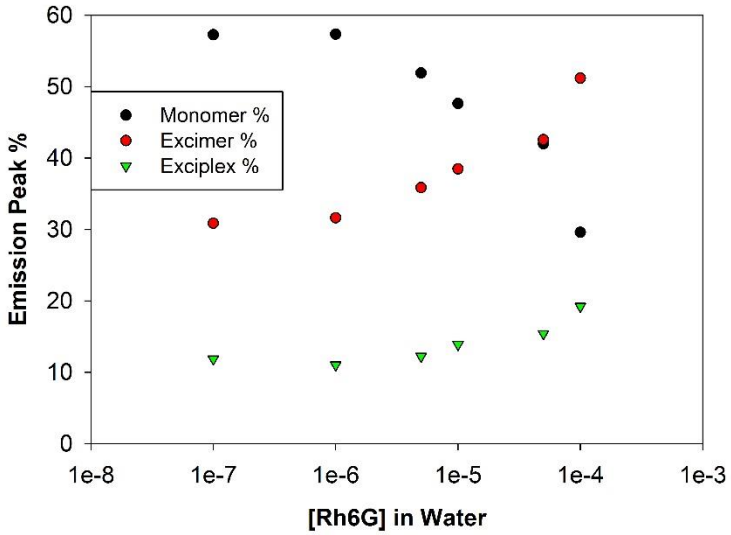

Figure 2-11. The molecular structure composition of Rh6G in water as a function of concentration according to deconvolution of emission spectra.

MANUSCRIPT – III

Prepared for submission to the Journal of Physical Chemistry C

Fabrication of Polymer Wrinkles and Photonic Structures Using a Simple Spin-Casting Method

Mingyu Chapman and William B. Euler

Chemistry, University of Rhode Island, Kingston, RI, USA

Corresponding Author: William B. Euler, Ph.D.

Chemistry

University of Rhode Island

140 Flagg Road

Kingston, RI, 02881, USA

Email address: wueler@chm.uri.edu

CHAPTER 3

ABSTRACT

The wrinkle patterns observed in PMMA are of the length scales that they could provide interesting optical effects. The wavelengths are in the range of visible, NIR, and IR light so the interaction of light with these structures may lead to trapping or redirection of the light. The amplitudes of the wrinkle patterns are in the tens of nm range, which might allow quantum confinement of small molecules located in the valleys. The relation between wrinkle amplitude and wrinkle wavelength can be controlled by the film thickness, which is further controlled by solution concentration and spin rate.

INTRODUCTION

The surface morphology of polymer films can have a strong influence on the interfacial properties and has been studied for many years in terms of adhesion.[1,2] Of more recent interest is the ability to pattern polymer thin films that then can be used as substrates for a variety of diverse areas, ranging from microelectronics[3-6] to understanding cell growth.[7,8] One common method for patterning a polymer surface is to induce wrinkling,[9,10] which, ideally, induces a periodic series of ridges and valleys. Wrinkles have been proposed to be used for stretchable electronics,[5,6] microlens applications,[11] and measurement of thin film mechanical properties.[12-17]

Wrinkles on polymer thin films can be formed spontaneously and is done by a variety of methods.[9,10,18-26] Typically these are multistep processes: a template is produced using a mechanically or thermally induced compressive stress (generally poly(dimethylsiloxane), PDMS) and then the template is used to transfer the wrinkle pattern to another substrate. The other common approach is to use block co-polymers, which aggregate into different phases that create the wrinkle.[27-35] A compendium of the different patterning approaches can be found in the comprehensive review by Rodríguez-Hernández.[10]

It has been reported that spin-casting can be used to create wrinkles in selected polymer systems.[28,35,36] In this research we are able to demonstrate wrinkle patterns in poly(methylmethacrylate) (PMMA) films by simple spin-casting without any templating or additional field to induce the periodic

deformation. PMMA is one of the polymers used to establish the foundational parameters for spin-casting.[37-41] In developing models to describe spin-casting, it was always assumed that the films had a uniform thickness. However, it was later recognized that solvent-polymer interactions could be used to influence surface roughness,[42-44] but no periodicity was reported. The spin-cast PMMA forms wrinkle pattern with wavelengths on the order of tens of microns and with amplitudes of tens of nanometers. These are the correct length scales to create a photonic structure that could lead to interesting properties.[45-51]

This work is aiming at understanding the parameters needed to create wrinkle patterns in polymer thin films. The periodicity of the wrinkles correlates with polymer thickness as controlled by changing the concentration of PMMA in the spin-casting solution. These data will be used to develop a model to predict wrinkle patterns. Finally, the study of wrinkle patterns act as a photonic structure and can influence the light emission of rhodamine 6G (Rh6G), a common laser dye will be investigated in the next paper.

EXPERIMENTAL SECTION

Microscope glass slides were cut into dimensions of 3.75 cm x 1.75 cm, followed by placing in a container of 95% ethanol (EtOH, Pharmaco-Aaper) and sonicated for 15 minutes. The Glass slides were rinsed and placed in water and sonicated for another 15 minutes, followed by drying with N_2 gas.

Different w/v solution of poly(methylmethacrylate) (PMMA, Signa-Aldrich, MW ~ 120000) was made in tolulene and sonicated for 4 hours at room temperature to ensure all PMMA was in solution.

The PMMA solution was applied to the glass substrate by spin casting. 2 minutes of purge with N_2 was done to reduce the humidity when humidity is above 20%. A 250 µl aliquot of solution was placed on the sample and was spun at a given RPM for 45 seconds. The sample was then placed in the over set at 60 °C for 1 minutes to dry.

The film thickness of the PMMA was determined by obtaining the fringing patterns in the reflection and absorption spectra from a PerkinElmer Lambda 1050 UV/vis/NIR spectrometer with 2.0 nm slit widths. Also, this film thickness of the PMMA was measured using a Filmetrics F40 thin film analyzer. The reflection spectrum was recorded with a tungsten halogen light source over a range of 400-900 nm and then compared to a calculated spectrum of given thickness and refractive index. The surface roughness and topography was obtained from optical profilometry (The Profilm 3D).

RESULTS AND DISCUSSION

PMMA films were produced by spin-casting a series of different concentrated PMMA solutions onto a glass slide at rotation rate of 1200 RPM. The edge of the films tend to be thicker than the center of the films at this rotation rate, so all the thickness were measured at the center of the film.

Spin-casting has been used to create polymer films for many years. The virtues of the method are that it is simple, highly reproducible, and gives films of controlled thickness. The thickness of a spin-cast can be estimated by

$$h = \chi_{pol}^{o}\left[\eta_o\left(\frac{cD_g}{\nu_g^{1/2}\rho}\right)\left(\frac{p_{sol}M_{pol}}{RT}\right)\left(1-\chi_{pol}^{o}-\chi_{sol}^{\infty}\right)\right]^{1/3}\frac{1}{\omega^{1/2}} \qquad [1]$$

where χ_{pol}^{o} is the mass fraction of polymer in the initial solution, η_o is the viscosity of the initial solution, χ_{sol}^{∞} is the mass fraction of pure solvent in the gas phase at equilibrium, ω = rotational velocity, D_g is the diffusivity of the solvent in the overlying gas, $\square_g$ is the kinematic velocity of the overlying gas, $\square$ is the solution density, p_{sol} is the vapor pressure of the pure solvent, M_{pol} is the molecular weight of the polymer, R is the ideal gas constant, T is the absolute temperature, and c = constant. Equation [1] demonstrates that controlling the thickness of the polymer film is complicated and can be achieved multiple ways: changing the concentration of the initial solution or changing the spin rate will have the biggest effect but changing the solvent, polymer molecular weight, temperature, or the composition of the overlying gas can all have small effects.

Primary control of the polymer thickness is attained either via spin rate or solution concentration.

Figure 3-2 shows the thickness of PMMA spin-cast from a range of different concentration and spin rate conditions. The solid lines are fits to equation [1], in the simplified form h = A/□^{½}. The fits are reasonable for all concentrations except the lowest, 3 mass % PMMA. Figure 3-3 shows the fit parameter, A, plotted as a function of initial PMMA concentration.

Equation [1] is complicated as a function of initial concentration because there is implicit concentration dependence in the initial viscosity, □$_o$. The solid line in Figure 3-2 is a fit to $A^3 = \left(a - b\chi_{pol}^{o}\right)\chi_{pol}^{o3}$, where the higher order terms in the brackets in equation [1] have been truncated. Again, the fit is reasonable except for the lowest concentration. This will allow us to determine other parameters in equation [1]. More importantly, equation [1] can serve as a starting point for understanding the details of the formation of the PMMA films.

A closer examination of the surfaces of the PMMA films shows that there is a periodic wrinkle observable in the film. Figure 3-4 shows optical microscopic images of several films formed by spin-casting different concentrations of PMMA solutions. The wrinkle pattern extends radially out from the middle of the substrate centered about the spinning axis.

The wavelengths of the wrinkles were measured by measuring the number light and dark lines along a measured distance and these results are shown in Figure 3-5. The wavelengths vary depending upon the thickness of the PMMA layer. The wrinkle wavelength increases as the PMMA film thickness increases

and then levels off at about 45 □m when the thickness reaches about 500 nm. The periodicity also changes as a function of the distance from the center of the spin axis. The farther from the middle that the measurement is made, the longer the wavelength of the wrinkles.

Figure 3-6 shows the depth profile of three samples taken near the edge of the film. There are several observations that can be made.

First, the wrinkles only started to form at the concentration of 1% (w/v), the thickness of this PMMA film is ~160 nm. Second, the wavelength of the wrinkles is longer at the edges than in the center of the film, for sample 3, the wavelength is ~80 □m, significantly higher than found in the center of the film (~70 □m). Third, the periodicity is reasonable constant over the millimeter length scale. Finally the amplitude of the periodic structure is on the order of nanometers, and the amplitude is increasing as the film thickness increases, the 1%, 2% and 3% PMMA film has the amplitude as 1.0 nm, 9.8 nm, and 21 nm respectfully. Finally, in case of the 3% w/v solution, which about 315 nm thick, the amplitude varies noticeable across the film: center is 13.5 nm, more cross to the right is 20.9 nm, and at the right edge is 37.5 nm. In contrast, the 2% w/v solution, which is about 200 nm thick, the amplitude is much more consistent.

Figure 3-7 shows the height profile for a PMMA with thickness ~315 nm fit to a sinusoid function

$$h = h_o + a_o sin\left(\frac{2\pi x}{\lambda_o} + b\right) \qquad [2]$$

where h_o is the mean film thickness if the zero of the y axis is set at the top of the underlying substrate, a_o is the amplitude of the wave, λ_o is the wavelength, and b

is a phase shift parameter. The parameter b is arbitrary and depends solely on the location of the zero point of the x axis. For this sample the fit is not perfect but does represent the data reasonably well with amplitude a_o = 15 nm, wavelength λ_o = 76 nm, and b = 6.

Figure 3-8 shows the average amplitude as a function of PMMA thickness can be calculated as

$$a = -40 + 1.8*t^{0.62} \quad [3]$$

where a is the average amplitude of the PMMA wrinkle, t is the average thickness of the PMMA film. This equation can be served as the basis for the quantitative investigation of the wrinkle formation in PMMA films.

The wrinkle wavelength also plotted as a function of PMMA thickness as shown in Figure 3-9. It decreases as PMMA film increase to 230 nm, and then increases as the PMMA film thickness increases, and levels off at about 100 □m when the thickness reaches about 500 nm. The decrease of the wrinkle wavelength could be associated with PMMA film reflective index. The reflective index of PMMA film drop from 1.9 to 1.53 as thickness increases to 250 nm[56].

CONCLUSION

Spin-casting is a simple method to obtain PMMA thin films with different film thickness. The two strongest influences on the PMMA thin film structure are the rotation rate and the initial solution concentration. Periodic wrinkles that develop in PMMA are on the length scale to act as photonic structures. The amplitudes are a bit larger than small molecules and the wavelengths are a few multiples of visible light and directly in the infrared. The periodicity of the wrinkles correlates with polymer thickness as controlled by changing the concentration of PMMA in the spin-casting solution. The wrinkled pattern starts to form with PMMA thickness above 160 nm, the amplitude of the wrinkle increases as the PMMA thickness increases, the amplitude can be predicted based on the PMMA thickness using equation $a = -40 + 1.8*t^{0.62}$. The wavelength of the wrinkle decreases as PMMA film increase to 230 nm, and increases as the PMMA film thickness increases, and eventually levels off at about 100 □m when the thickness reaches about 500 nm.

ACKNOWLEDGEMENT

This material is based upon work supported by the U.S. Department of Homeland Security, Science and Technology Directorate, Office of University Programs, under Grant Award 2013-ST-061-ED0001. The views and conclusions contained in this document are those of the authors and should not be interpreted as necessarily representing the official policies, either expressed or implied, of the U.S. Department of Homeland Security.

LIST OF REFERENCES

(1) G. Fourche, "An Overview of the Basic Aspects of Polymer Adhesion. Part I: Fundamentals," *Polym. Eng. & Sci.*, **1995**, *35*, 957–967.

(2) A. W. Adamson and A. P. Gast, *Physical Chemistry of Surfaces*, 6th edition, John Wiley & Sons, New York, **1997**.

(3) N. Bowden, S. Brittain, A. G. Evans, J. W. Hutchinson, and G. M. Whitesides, "Spontaneous Formation of Ordered Structures in Thin Films of Metals Supported on an Elastomeric Polymer," *Nature*, **1998**, *393*, 146–149.

(4) H. O. Jacobs and G. M. Whitesides, "Submicrometer Patterning of Charge in Thin-Film Electrets," *Science*, **2001**, *291*, 1763–1766.

(5) D.-Y. Khang, H. Jiang, Y. Huang, and J. A. Rogers, "A Stretchable Form of Single-Crystal Silicon for High-Performance Electronics on Rubber Substrates," *Science*, **2006**, *311*, 208–212.

(6) D.-H. Kim, J.-H. Ahn, W. M. Choi, H.-S. Kim, T.-H. Kim, J. Song, Y. Y. Huang, Z. Liu, C. Lu, and J. A. Rogers, "Stretchable and Foldable Silicon Integrated Circuits," *Science*, **2008**, *320*, 507–511.

(7) M. J. Dalby, M. O. Riehle, S. J. Yarwood, C. D. W. Wilkinson, and A. S. G. Curtis, "Nucleus Alignment and Cell Signaling in Fibroblasts: Effects of Channel Size, Cell Type, and Matrix Composition on Pattern Integrity," *Exp. Cell. Res.*, **2003**, *284*, 274–282.

(8) Y. Hu, J.-O. You, and J. Aizenberg, "Micropatterned Hydrogel Surface with High-Aspect-Ratio Features for Cell Guidance and Tissue Growth," *ACS Appl. Mater. Interfaces*, **2016**, *8*, 21939–21945.

(9) J. Genzer and J. Groenewold, "Soft Matter with Hard Skin: From Skin Wrinkles to Templating and Material Characterization," *Soft Matter*, **2006**, *2*, 310–323.

(10) J. Rodríguez-Hernández, "Wrinkled Interfaces: Taking Advantage of Surface Instabilities to Pattern Polymer Surfaces," *Progress in Polymer Science*, **2015**, *42*, 1–41.

(11) S. Y. Ryu, J. Xiao, W. I. Park, K. S. Son, Y. Y. Huang, U. Paik, and J. A. Rogers, "Lateral Buckling Mechanics in Silicon Nanowires on Elastomeric Substrates," *Nano Lett.*, **2009**, *9*, 3214–3219.

(12) C. M. Stafford, M. G. Harrison, K. Beers, A. Karim, E. J. Amis, M. R. Vanlandingham, H.-C. Kim, W. Volksen, R. D. Miller, and E. E. Simonyi, "A Buckling-Based Metrology for Measuring the Elastic Moduli of Polymeric Thin Films," *Nat. Mater.*, **2004**, *3*, 545–550.

(13) H. Huang, J. Y. Chung, A. J. Nolte, and C. M. Stafford, "Characterizing Polymer Brushes via Surface Wrinkling," *Chem. Mater.*, **2007**, *19*, 6555–6560.

(14) J. Y. Chung, T. Q. Chastek, M. J. Fasolka, H. W. Ro, and C. M. Stafford, "Quantifying Residual Stress in Nanoscale Thin Polymer Films via Surface Wrinkling," *ACS Nano*, **2009**, *3*, 844–852.

(15) J. A. Howarter and C. M. Stafford, "Instabilities as a Measurement Tool for Soft Materials," *Soft Matter*, **2010**, *6*, 5661 – 5666.

(16) J. Y. Chung, J.-H. Lee, K. L. Beers, and C. M. Stafford, "Stiffness, Strength, and Ductility of Nanoscale Thin Films and Membranes: A Combined Wrinkling Cracking Methodology," *Nano Lett.*, **2011**, *11*, 3361–3365.

(17) E. P. Chan, S. Kundu, Q. Lin, and C. M. Stafford, "Quantifying the Stress Relaxation Modulus of Polymer Thin Films via Thermal Wrinkling," *ACS Appl. Mater. Interfaces*, **2011**, *3*, 331–338.

(18) K. E. Efimenko, M. Rackaitis, E. Manias, A. Vaziri, L. Mahadevan and J. Genzer, "Nested Self-Similar Wrinkling Patterns in Skins," *Nat. Mater.*, **2005**, *4*, 293–297.

(19) J. A. Rogers, "Slice and Dice, Peel and Stick: Emerging Methods for Nanostructure Fabrication," *ACS Nano*, **2007**, *1*, 151–153.

(20) M. Wang, J. E. Comrie, Y. Bai, X. He, S. Guo, and W. T. S. Huck, "Formation of Hierarchically Structured Thin Films," *Adv. Funct. Mater.*, **2009**, *19*, 2236–2243.

(21) S. H. Ahn and L. J. Guo, "Spontaneous Formation of Periodic Nanostructures by Localized Dynamic Wrinkling," *Nano Lett.*, **2010**, *10*, 4228–4234.

(22) M. Ramanathan, S. M. Kilbey II, Q. Ji, J. P. Hill, and K. Ariga, "Materials Self-Assembly and Fabrication in Confined Spaces," *J. Mater. Chem.*, **2012**, *22*, 10389–10405.

(23) M. Ramanathan, B. S. Lokitz, J. M. Messman, C. M. Stafford, and S. M. Kilbey II, "Spontaneous Wrinkling in Azlactone-Based Functional Polymer Thin Films in 2D and 3D Geometries for Guided Nanopatterning," *J. Mater. Chem. C*, **2013**, *1*, 2097–2101.

(24) J. Choi, J. Huh, K. R. Carter, and T. P. Russell, "Directed Self-Assembly of Block Copolymer Thin Films Using Minimal Topographic Patterns," *ACS Nano*, **2016**, *10*, 7915–7925.

(25) D. S. Kim, Y. J. Cha, M.-J. Gim, and D. K. Yoon, "Fast Fabrication of Sub-200-nm Nanogrooves Using Liquid Crystal Material," *ACS Appl. Mater. Interfaces*, **2016**, *8*, 11851–11856.

(26) C. T. Chapman, J. T. Paci, W.-K. Lee, C. J. Engel, T. W. Odom, and G. C. Schatz, "Interfacial Effects on Nanoscale Wrinkling in Gold-Covered Polystyrene," *ACS Appl. Mater. Interfaces*, **2016**, *8*, 24339–24344.

(27) C. W. Frank, V. Rao, M. M. Despotopoulou, R. F. W. Pease, W. D. Hinsberg, R. D. Miller, and J. F. Rabolt, "Structure in Thin and Ultrathin Spin-Cast Polymer Films," *Science*, **1996**, *273*, 912–915.

(28) S. Walheim, M. Böltau, J. Mlynek, G. Krausch, and U. Steiner, "Structure Formation via Polymer Demixing in Spin-Cast Films," *Macromolecules*, **1997**, *30*, 4995–5003.

(29) S. Yang, K. Khare, and P.-C. Lin, "Harnessing Surface Wrinkle Patterns in Soft Matter," *Adv. Funct. Mater.*, **2010**, *20*, 2550 – 25564.

(30) H. Yang, M. Su, K. Li, L. Jiang, Y. Song, M. Doi, and J. Wang, "Preparation of Patterned Ultrathin Polymer Films," *Langmuir*, **2014**, *30*, 9436–9441.

(31) H. Ogawa, M. Takenaka, T. Miyazaki, A. Fujiwara, B. Lee, K. Shimokita, E. Nishibori, and M. Takata, "Direct Observation on Spin-Coating Process of PS‐b‐P2VP Thin Films," *Macromolecules*, **2016**, *49*, 3471–3477.

(32) X. Gu, I. Gunkel, A. Hexemer, and T. P. Russell, "Controlling Domain Spacing and Grain Size in Cylindrical Block Copolymer Thin Films by Means of Thermal and Solvent Vapor Annealing," *Macromolecules*, **2016**, *49*, 3373–3381.

(33) A. A. Abate, G. T. Vu, A. D. Pezzutti, N. A. García, R. L. Davis, F. Schmid, R. A. Register, and D. A. Vega, "Shear-Aligned Block Copolymer Monolayers as Seeds To Control the Orientational Order in Cylinder-Forming Block Copolymer Thin Films," *Macromolecules*, **2016**, *49*, 7588–7596.

(34) Q. Yang, B. Q. Li, H. Tian, X. Li, J. Shao, X. Chen, and F. Xu, "Deformation Hysteresis of Electrohydrodynamic Patterning on a Thin Polymer Film," *ACS Appl. Mater. Interfaces*, **2016**, *8*, 17668–17675.

(35) C. Schaefer, J. J. Michels, and P. van der Schoot, "Structuring of Thin-Film Polymer Mixtures upon Solvent Evaporation," *Macromolecules*, **2016**, *49*, 6858–6870.

(36) J.-S. Peng, F. Yang, D. Chiang, and S. Lee, "Kinetics of Field-Induced Surface Patterns on PMMA," *Langmuir*, **2016**, *32*, 4602–4609.

(37) W.M. Prest, Jr., and D. J. Luca, "The Origin of the Optical Anisotropy of Solvent Cast Polymeric Films," *J. Appl. Phys.*, **1979**, *50*, 6067–6071.

(38) W. M. Prest, Jr. and D. J. Luca, "The Alignment of Polymers During the Solvent-Coating Process," *J. Appl. Phys.*, **1980**, *51*, 5170–5174.

(39) D. E. Bornside, C. W. Macosko, and L. E. Scriven, "Spin Coating: One-dimensional Model," *J. Appl. Phys.*, **1989**, *66*, 5185–5193.

(40) D. E. Bornside, 1 C. W. Macosko, and L. E. Scriven, "Spin Coating of a PMMA/Chlorobenzene Solution," *J. Electrochem. Soc.*, **1991**, *138*, 317–320.

(41) S. Askar, C. M. Evans, and J. M. Torkelson, "Residual Stress Relaxation and Stiffness in Spin-Coated Polymer Films: Characterization by Ellipsometry and Fluorescence," *Polymer*, **2015**, *76*, 113–122.

(42) K. E. Strawhecker, S. K. Kumar, J. F. Douglas, and A. Karim, "The Critical Role of Solvent Evaporation on the Roughness of Spin-Cast Polymer Films, *Macromolecules*, **2001**, *34*, 4669–4672.

(43) M. Benz, W. B. Euler, O. J. Gregory, "The Influence of Preparation Conditions on the Surface Morphology of Poly(vinylidene fluoride) Films," *Langmuir*, **2001**, *17*, 239–243.

(44) M. Benz, W. B. Euler, O. J. Gregory, "The Role of Solution Phase Water on the Deposition of Thin Films of Poly(vinylidene fluoride)," *Macromolecules*, **2002**, *35*, 2682–2688.

(45) C. Genet and T. W. Ebbesen, "Light in Tiny Holes," *Nature*, **2007**, *445*, 39–46.

(46) I. A. Levitsky, W. B. Euler, N. Tokranova, and A. Rose, "Fluorescent Polymer – Porous Silicon Microcavity Devices for Explosives Detection," *Appl. Phys. Lett.*, **2007**, *90*, 041904.

(47) P. Lalanne, C. Sauvan, and J. P. Hugonin, "Photon Confinement in Photonic Crystal Nanocavities," *Laser & Photonics Reviews*, **2008**, *2*, 514–526.

(48) Y.-S. Hsiao, S. Charan, F.-Y. Wu, F.-C. Chien, C.-W. Chu, P. Chen, and F.-C. Chen, "Improving the Light Trapping Efficiency of Plasmonic Polymer Solar Cells through Photon Management," *J. Phys. Chem. C*, **2012**, *116*, 20731–20737.

(49) M. A. Matoian, R. Sweetman, E. C. Hall, S. Albanese, and W. B. Euler, "Light Trapping to Amplify Metal Enhanced Fluorescence with Application for Sensing TNT," *J. Fluoresc.*, **2013**, *23*, 877- 880.

(50) W. Zhou, R. Liu, D. Tang, X. Wang, H. Fan, A. Pan, Q. Zhang, Q. Wan, and B. Zou, "Luminescence and Local Photonic Confinement of Single ZnSe:Mn Nanostructure and the Shape Dependent Lasing Behavior," *Nanotechnology*, **2013**, *24*, 055201.

(51) A. Mischok, R. Brückner, M. Sudzius, C. Reinhardt, V. G. Lyssenko, H. Fröb, and K. Leo, "Photonic Confinement in Laterally Structured Metal-Organic Microcavities," *Appl. Phys. Lett.*, **2014**, *105*, 051108.

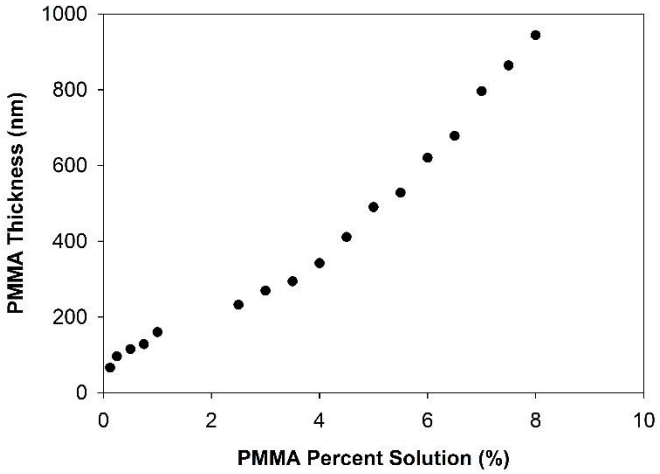

Figure 3-1. Thickness of PMMA thin film as a function of PMMA percent at rotation rate of 1200 RPM. The thicknesses were determined using reflection spectra.

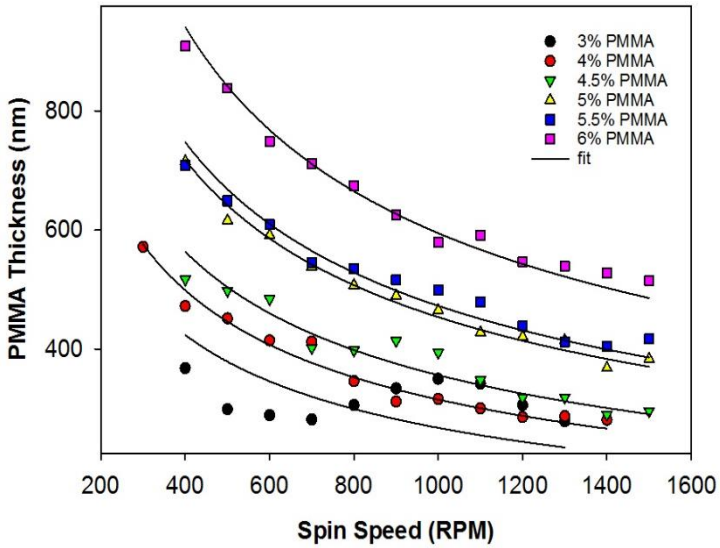

Figure 3-2. Film thickness of PMMA with different initial solution concentration as a function of rotational rate. The solid lines are fits to equation [1].

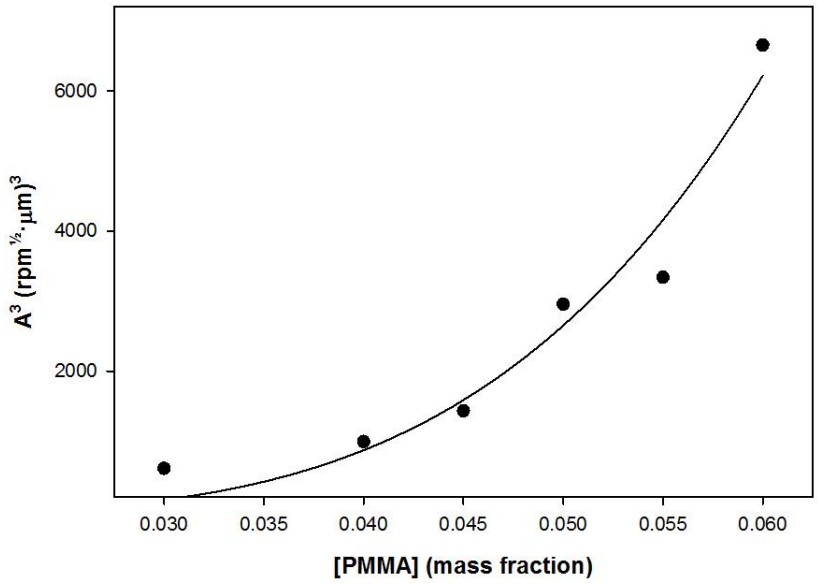

Figure 3-3. The fit parameter from Figure 3-2 plotted as a function of the initial PMMA solution. The solid line is a fit to a function of the form $A^3 = \chi_{pol}^{o3}(a - b\chi_{pol}^{o})$.

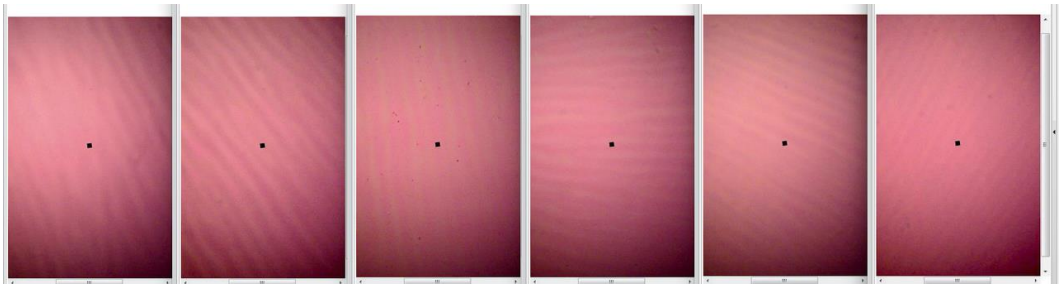

Figure 3-4: Optical micrographs of PMMA films formed by spin-casting solutions of the indicated mass percent of PMMA. Each image is 450 mm wide and 710 mm tall. The images were taken near the center of the films.

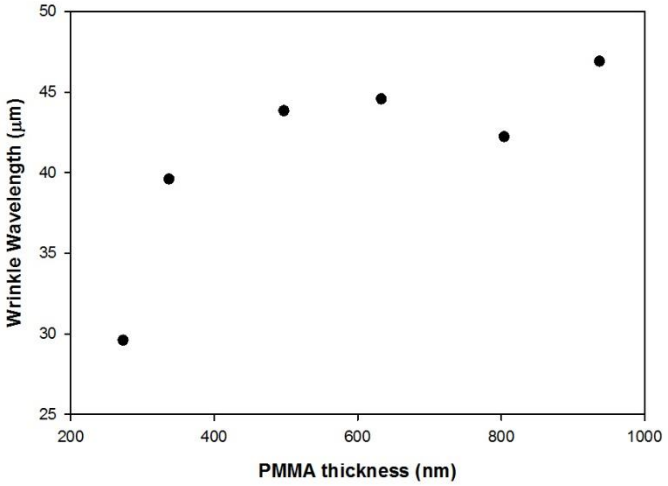

Figure 3-5. Wrinkle wavelength measured as a function of PMMA thickness, sampled near the middle of the film.

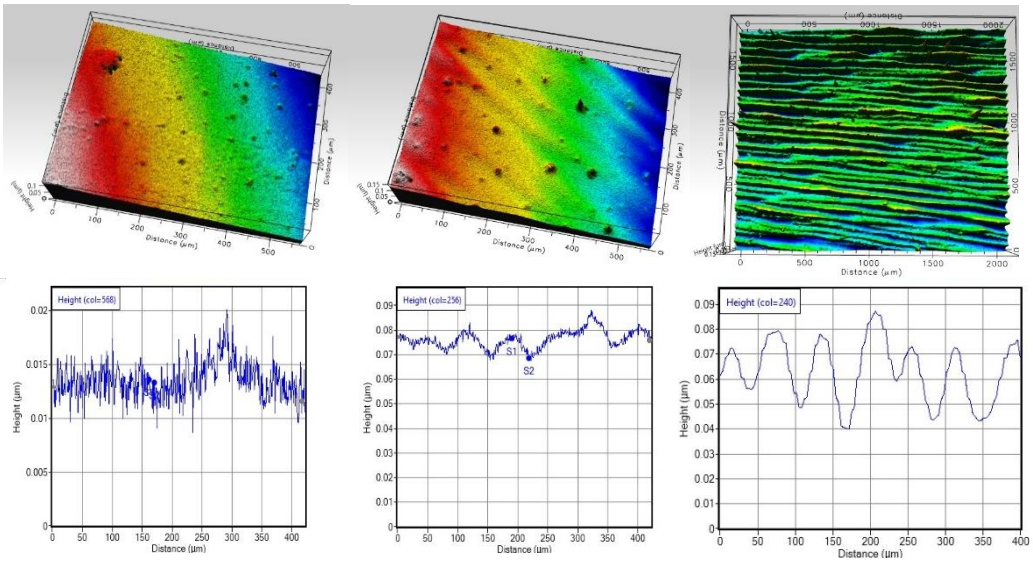

Figure 3-6. Optical profiles of PMMA films spin-cast from 1%, 2% and 3% w/v solution. The image was taken near the edge of the film. Bottom: Height profile of the image shown in the top. The profile was taken at the right edge in the upper image.

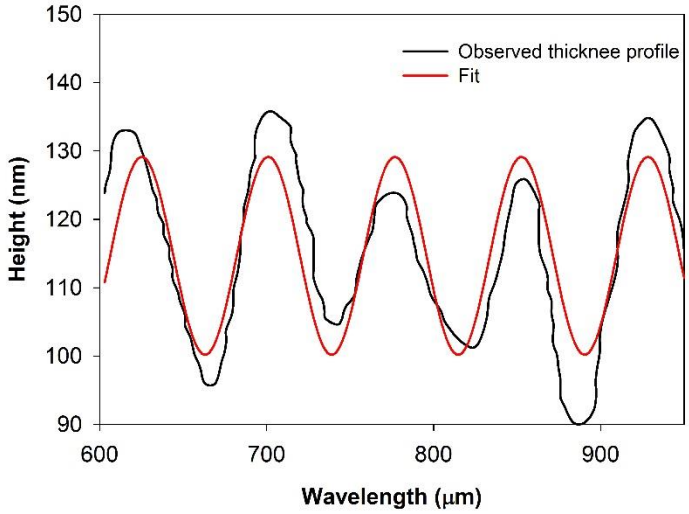

Figure 3-7. Black line: observed height profile (closer to the center) of a ~315 nm PMMA film. Red line: fit to a function of the form $h = h_o + a_o sin\left(\frac{2\pi x}{\lambda_o} + b\right)$

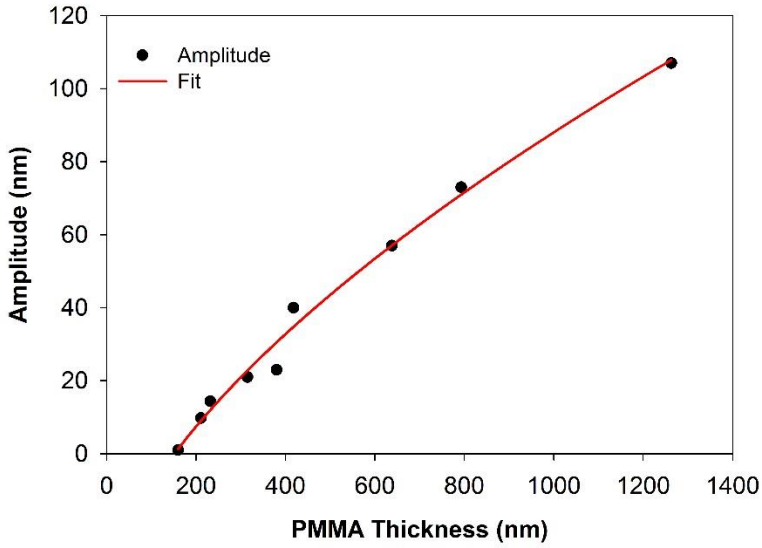

Figure 3-8. Black dot: observed average amplitude of a range of PMMA films. Red line: fit to a function $a = y_0 + k*t^b$

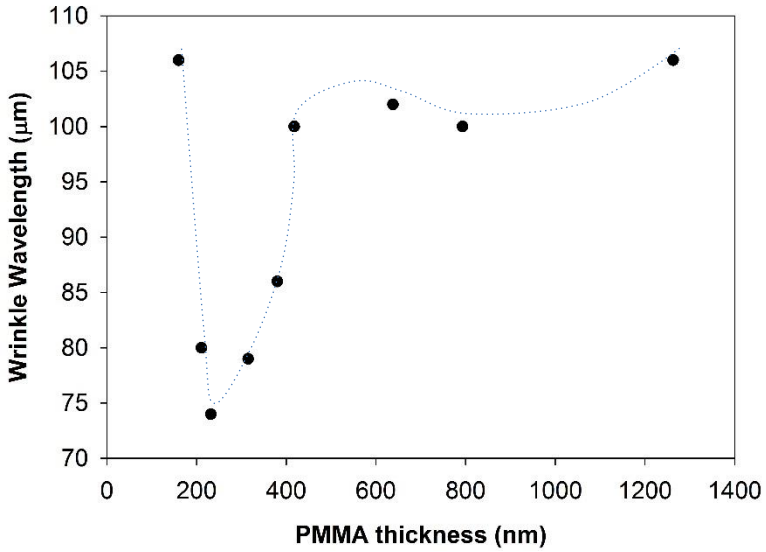

Figure 3-9. Averaged wrinkle wavelength as a function of PMMA thickness. The dotted line is intended to be a guide for the eye.

MANUSCRIPT – IV

Prepared for submission to the Journal of Physical Chemistry C

Fluorescence Enhancement Effect of Poly(methylmethacrylate) PMMA on Rhodamine 6G Thin Film for Explosive Vapor Detection

Mingyu Chapman and William B. Euler

Chemistry, University of Rhode Island, Kingston, RI, USA

Corresponding Author: William B. Euler, Ph.D.

Chemistry

University of Rhode Island

140 Flagg Road

Kingston, RI, 02881, USA

Email address: wueler@chm.uri.edu

CHAPTER 4

ABSTRACT

A three-layered sensor system with enhanced emission intensity has been demonstrated and studied. When Rh6G thin film is deposited on a glass substrate, a fluorescent signal is observed of modest intensity. However, when a transparent poly(methylmethacrylate) PMMA layer is added to separate the Rh6G layer and the glass substrate, the emission signal increases dramatically. The increased sensitivity associated with this emission enhancement allows for low vapor pressure analyte detection. The interfacial properties that control the nature of fluorescent emission and photophysics are determined and exploited to optimize sensor system sensitivity.

INTRODUCTION

With the increasing public concern for possible future terrorist attacks involving novel explosives, there is a demand for advanced early detection technology.[1–4] The extremely low vapor pressures at room temperature of most explosives limit the number of explosives molecules to be collected in a reasonable detection time pushes limits for most conventional fluorescence sensors.[1–6]

The underlying idea behind analyte fluorescent detection is simple.[5,6] Fluorophore emissions are measured before and after analyte sample exposure.[7] The emission intensity can be quenched, enhanced or unchanged.[7] There are three distinct mechanisms underlying these emission intensity changes: collisional quenching, aggregation changes and energy transfers.[8–10] Collisional quenching occurs when analyte molecules collide with a fluorophore in the excited state.[11–15] Additional nonradiative pathways become available for the fluorophore to lose its energy, resulting in a decreased amount of emitted light, thus the emission intensity is quenched.[11–15] In the case of aggregation changes, the analyte can cause a structural change in a fluorophore by either inducing aggregation or by disrupting aggregation, which can lead to either enhancement or quenching of the emission.[19–26] Energy transfer upon exposure to the analyte occurs when the energy transfer from higher energy excited state is disrupted causing a quenching of the emission intensity.[27–30]

To improve emission signal output, several methods have been used to amplify the fluorescent signal, such as metal-enhanced fluorescence, which is a common approach but making reproducible metallic surfaces is challenging.[28,29] Other methods include incorporating the fluorophore into a solid matrix such as polymers and clays, but the photophysical properties of the fluorophore might be changed.[30–34]

A new sensing system for gas phase explosive is proposed in this study. This sensor is based on a layered structure of fluorophore deposited onto a few hundred nanometers of a transparent polymer, supported by a glass slide, as shown in Scheme 4-1. The fluorophore selected is Rhodamine 6G (Rh6G), which is an inexpensive xanthene laser dye, widely used as a fluorescence tracer because of its strong absorption properties in the visible light region and high fluorescence quantum yield.[35–37]

A monolayer thin film deposited onto a substrate could have several structures, such as ground state monomer and aggregates, excited state excimer and dimer.[38–42] As reported previously, Rh6G thin films were spin cast into glass substrate using EtOH as a solvent. The thickness of Rh6G film was controlled by the concentration of the casting solutions, surface coverage and dye density on the surface.[38–42] At extremely low dye density, when the surface coverage is low, monomeric structure is dominating.[38–42] With increasing dye density, the formation of excited state excimer and excitonic dimer can occur since most of the Rh6G molecules have a nearby neighbor.[43–52] Further increase in surface

coverage and dye density, additional layer of Rh6G forms and aggregated Rh6G grow until eventually the aggregated Rh6G dominates the structure.[44,56–61]

When this Rh6G layer is applied on PMMA layer before putting on the glass, a huge emission enhancement will occur.[7,59] This emission enhancement can be explained by internal reflection, as shown in Scheme 4-2: When the light hits on the fluorophore layer, some of the light is reflected at each interface, which allows the light to bounce along the polymer layer.[60–66] At each bounce on the polymer/fluorophore interface, the light that escapes excites more fluorophore, effectively increasing the efficiency of the use of the excitation light.[60–66] This huge emission enhancement shows the potential to be used as a fluorescence-based sensor with improved sensitivity, and it is sensitive enough to detect explosives with low vapor pressures under room temperature.[67–70]

In this work we examine the absorption and emission spectra for Rh6G deposited onto glass substrate directly and with a PMMA layer in between. The thickness of the fluorophore will be a key feature in determining the sensitivity of the sensor. The role of the transparent PMMA film interface on Rh6G properties is studied in detail, shows the thickness of the PMMA layer affects the internal reflection, and the surface morphology of PMMA film affects the Rh6G structure by reducing the amount of aggregation of Rh6G. Finally, the reaction mechanism between Rh6G and TNT vapor is examined and studied, the relationship between Rh6G structure and types of mechanism leads to a better mechanistic understanding of the sensor platform.

EXPERIMENTAL SECTION

Rhodamine 6G chloride (Rh6G) was supplied by Acros Organics and was used without further purification. A range of Rh6G solutions were prepared and used for thin film preparation: 1×10^{-9} M − 1×10^{-2} M in 95% ethanol.

The polymer used is polymethylmethacrylate (MW ~120,000, PMMA) and was obtained from Sigma Aldrich. PMMA was dissolved in toluene to form a 4% (w/v) solution.

Borosilicate glass (BSG) microscope slides were prepared by sonication in 95% ethanol and distilled water (15 min each) followed by blow-drying with dry nitrogen gas.

A Laurell Technologies spin coater was used for spin-casting films. A 250 μL portion of the Rh6G solution was placed on the BSG slide, and the rotation was set to 1200 rpm. The thin films were then allowed to dry in air. A 250 μL portion of the poly(methylmethacrylate) (PMMA) solution was placed on the BSG slide, and the rotation was set to 1200 rpm. The three layered samples were prepared by spin-coating the polymer onto the glass slide followed by spin coating the Rh6G solutions into the polymer layer. All thin films were prepared at low humidity (<20%).

The absorption spectra were obtained using a PerkinElmer Lambda 1050 spectrometer. The slit width was set to 2 nm, the wavelength range was set from

700 to 350 nm, and the integration time was set to 10 s for samples made with concentrations lower than 2×10^{-6} M, 5 s for samples made with concentrations between 3×10^{-6} M and 3×10^{-5} M, 3 s for samples made with concentrations between 4×10^{-5} M and 1×10^{-4} M, and 1 s for samples made with concentrations above 1×10^{-4} M. All spectra were baseline corrected by automatic baseline subtraction with PeakFit v4.12 software.

The fluorescence emission spectra and excitation spectra was acquired using a Horiba (Jobin Yvon) Fluorolog spectrometer. The light source used was a Xenon arc lamp. For emission spectra, the excitation wavelength was set at the absorbance maximum, and the slit width was set to 2 nm.

The film thickness of the PMMA was determined by obtaining the absorbance spectra from a PerkinElmer Lambda 1050 UV/vis/NIR spectrometer with 2.0 nm slit widths, and calculated based on the absorbance intensity. And it also measured by using a Filmetrics F40 thin film analyzer.

The film thickness of the PMMA was determined by obtaining the fringing patterns in the reflection and absorption spectra from a PerkinElmer Lambda 1050 UV/vis/NIR spectrometer with 2.0 nm slit widths. Also, this film thickness of the PMMA was measured using a Filmetrics F40 thin film analyzer. The reflection spectrum was recorded with a tungsten halogen light source over a range of 400-900 nm and then compared to a calculated spectrum of given thickness and refractive index. The surface roughness and topography was obtained from optical profilometry (The Profilm 3D).

RESULTS AND DISCUSSION

The spin coating deposition technique was used to build the three layered sensor as shown in Scheme 4-1: a layered structure of fluorophore (Rh6G) deposited onto a transparent polymer, supported by a glass slide. The polymer chosen was polymethylmethacrylate (PMMA), the thicknesses of the PMMA layer ranged from 200 nm to 1000 nm with sample-to-sample variance of ± 30 nm. This was measured via the fringing pattern in absorption spectra and thickness fit with reflection spectra. The Rh6G thin film thicknesses ranged from 0.6 nm to 13 nm measured by reflection spectra.

Figure 4-1 shows the emission spectra of 0.7 nm, 1.0 nm and 1.7 nm Rh6G film deposited on glass substrate and on a layer of 385 nm PMMA film. The data shows, the addition of this transparent PMMA film layer causing a large emission enhancement. The Area under curve ratio of emission on PMMA to emission on glass is 4.0, 3.3, and 6.9 respectfully. This three-layered structure shows high fluorescent signal output comparing to the general two-layered structure, leading to high sensitivity as fluorescent sensor. This increased sensitivity associated with emission enhancement has the potential for detecting low vapor pressure analyte, such as TNT molecules.

In order to understand this emission enhancement, Rh6G structure, role of the interface and PMMA thickness are examined in more detail.

SECTION 1: Effects of PMMA layer on sensor sensitivity. The absorption spectra of a series of films on glass and PMMA surface are shown in Figure 4-2. The thickness of the Rh6G thin film was measured by reflection spectroscopy, and the formulas given in previous report was used to estimate the Rh6G film thickness, both methods agree with each other on the thickness determination. The Rh6G film thicknesses are 0.7 nm, 1.0 nm, 1.7 nm, 2.6 nm and 9.2 nm respectfully. The thickness of PMMA film measured by reflection spectroscopy is 385 nm.

As the Rh6G casting concentration increases, the films became thicker and the spectra became more intense. Based on assignments from previous study, Figure 4-2A and 4-2B correspond to a sub-monolayer and a monolayer of Rh6G, Figure 4-2C corresponds to a bilayer of Rh6G and Figure 4-2D and Figure 4-2E corresponds to multilayers of Rh6G.

The absorption spectra of Rh6G on glass and PMMA are similar: both have a low energy peak maximum and a higher energy shoulder. The peak maximum is shifted to the lower energy in the PMMA samples with Rh6G thickness smaller than 1.0 nm, as shown in Figure 4-2A and 4-2B, peak maximum on glass for 0.7 nm Rh6G is 522 nm while on PMMA is 537 nm, and peak maximum on glass for 1.0 nm Rh6G is 522 nm, while on PMMA is 541 nm. This peak maximum is shifted to the higher energy in the PMMA sample when Rh6G is thicker than 1.0 nm as shown in Figure 4-2C to Figure 4-2E, peak maximum for

2.6 nm Rh6G on glass is 560 nm while on PMMA is 548 nm, and peak maximum for 9.2 nm Rh6G on glass is 563 nm while on PMMA is 555 nm.

At extremely low dye density, the surface coverage of this film is low. The spectroscopic signature of the monomeric structure is dominant in both glass and PMMA samples. As shown in Figure 4-2A, the absorbance maxima for Rh6G on PMMA is 537 nm, while on glass is 521 nm, which can be attributed to the polarity difference in the two surfaces.

Figure 4-2B is a film with surface coverage just below a monolayer. From the previous paper, it was shown that on a glass surface, the primary excited states become a mix of excimers and excitons, with excimers dominating at this film thickness. The line shape did not change much when comparing to the low surface coverage film. On the PMMA surface, the line shape changed more when compared to the low surface coverage film, which the high-energy shoulder increased, and the low energy shoulder became broader.

Figure 4-2D and 4-2E show the multilayer Rh6G thin films on glass and PMMA surface. On both surfaces, the line shape of bilayer and multilayer Rh6G remained the same, although both shifted to the lower energy side with increasing film thickness. This shows the structural changes in these films are very few to none.

The surface coverage plays a very important role in the Rh6G thin film structure. With the same deposition concentration and same volume on the surface,

shows the initial number of molecules were same on the glass and PMMA surface before spinning process start. The final surface coverage after spin-cast is significantly different on glass and PMMA as shown in Figure 4-3, especially for the lower deposition concentrations.

Figure 4-3A is the Rh6G thin film with extreme low surface coverage both spin-cast from $3x10^{-6}$ M solution on both surfaces. The absorbance area under curve on glass is 3.85 times more than on PMMA surface, shows the number of Rh6G molecules on glass is about 3.85 times more than on PMMA surface. The surface coverage on PMMA is almost 4 times smaller than on the glass.

Figure 4-3B is the Rh6G thin film with high surface coverage just below a monolayer. With this casting solution concentration, the surface coverage is reaching saturation. The absorbance area under curve is 1.5 times more than on PMMA surface, shows the number of molecules on glass surface is about 1.5 times more than on PMMA surface. With this casting solution concentration, the surface coverage on PMMA is 1.5 times smaller than on the glass.

For Rh6G film below one layer, the number of molecules on glass surface is much larger than on PMMA surface, thus the distance between two Rh6G molecules on glass is smaller than on glass, as a result, PMMA surface is less in favor for aggregates at this surface coverage.

Since further increases in casting solution concentration will start to form the second layer, Figure 4-3C is the bilayer Rh6G on PMMA and glass, and

Figure 4-3D is the multilayer Rh6G film on PMMA and glass. Once second layer of Rh6G starts to form, the thickness of Rh6G became same, shows the Rh6G film thickness and orientation of the molecules are no longer affected by the different surface, instead, they are both affected by the first Rh6G film layer.

Figure 4-4A shows the evolution of the thickness as a function of increasing of Rh6G casting solution concentration. With the same casting concentration, the thickness of a Rh6G film on PMMA is thinner than on a glass surface, showing that PMMA has a larger surface area compared to the glass surface.

As thickness of the Rh6G thin film increases, the absorbance maxima shift to low energy side for both glass and PMMA as shown on Figure 4-3B. The absorption maxima shift from 535 nm to 555 nm for Rh6G on PMMA, and absorption maxima shifts from 521 nm to 564 nm for Rh6G on glass. As the previous study had shown, the shift of absorbance maxima to the lower energy side is associated with the degree of aggregation. The aggregate is less affected by the PMMA surface.

The surface morphology of PMMA thin films have a strong influence on the interfacial properties from above spectra study. As shown in previous study on the PMMA film structure, it indicates the film surface is rough and has repetitive patterns of wrinkles.

A closer examination of the surface of this 385 nm PMMA films shows there is a periodic wrinkle observable in the film as shown in Figure 4-5. The wrinkle pattern extends radially out the middle of the substrate centered about the spinning axis. The wrinkle can act as a photonic structure as the amplitudes are larger than small molecules, and the wavelength are few multiples of visible light and directly in the infrared. In this PMMA thin film, the amplitude of the wrinkle is 17 nm, and the wrinkle wavelength is 80 μm. As the amplitude is larger than 10 nm, the possibility of quantum confinement effect is low. The emission enhancement could be due to the more emissive structure formation on PMMA surface, or due the multiple internal reflections in the PMMA layer allows for increases excitations of the Rh6G layer. A more detailed investigation study is carried out as below.

The thickness of the PMMA plays an important role in the emission enhancement. As shown in Figure 4-6A, for the same thickness Rh6G film on PMMA layer, as the PMMA thickness increases, the emission decreases, and the emission maxima shifts to the lower energy side, suggesting the component of the emissive structure has changed as shown in Figure 4-6C.

This could be explained by internal reflection. As shown in Scheme 4-2, when the light hit the Rh6G layer, some of the light is reflected back (red arrow). At same time, since PMMA is a transparent layer, some light will be able to penetrate further into the PMMA layer until reflected back by the bottom glass layer. This reflected light will hit on the Rh6G layer again and excited more

Rh6G molecules, as a result, the number of excited molecules increases, hence the emission intensity increases. As the PMMA layer getting thicker, the reflective index reduces, and less light can excite Rh6G molecules, results in the emission intensity drop.

The red dots are the wrinkle amplitude as a function of PMMA thickness. As the PMMA thickness increases, the wrinkle amplitude increases. As the wrinkle amplitude increases, the Rh6G emission intensity decreases as shown in Figure 4-6B, it shows the amplitudes of the wrinkle on PMMA affects the emission intensity. The maximum emission enhancement was achieved by 160 nm PMMA layer, right when the PMMA film starts to form the wrinkle pattern. The amplitude of the wrinkle is 1 nm. This amplitude is lower than 10 nm, allowing quantum confinement effect to occur.

SECTION 2: Effect of Rh6G layer on sensor sensitivity. In order to achieve the maximum sensor sensitivity, the thickness of the top Rh6G layer is critical. As shown in Figure 4-7, different thicknesses of Rh6G films were spin-cast on 385 nm PMMA layer. As the Rh6G thin film thickness increases, the emission maxima shift to the lower energy, indicating an increase in aggregation, and the emission intensity increases until reaching the 1.0 nm. Further increase in the Rh6G thickness results in decreasing emission intensity due to aggregation and formation of the second layer.

However, the 1.0 nm Rh6G thin film is unique in comparison with other Rh6G films; it has the highest emission intensity and the emission maxima is around 575 nm. This shows the excimer is the major emissive component in this thin film. Further increase in the thickness, as the second layer starts to form, the

emission due to the aggregates increases, which is in agreement with our previous work.

The intensity change due to the maximum surface coverage of the film is larger on PMMA compared to glass as shown in Figure 4-8A.

1.0 nm Rh6G thin film is the film with the highest surface coverage before forming the second layer on PMMA surface. Somehow, the 0.9 nm Rh6G film has even higher emission intensity compare to 1.0 nm film, right before reaching the saturation surface coverage as shown in Figure 4-8A.

This thickness 0.9-1.0 nm Rh6G film could be a good candidate for high sensitivity sensor design. And these films were spin-cast from 5 x 10^{-5} M to 1 x 10^{-5} M solution as shown in Figure 4-4. Understanding the structure of Rh6G molecules in this particular thickness thin film is very important for investigating the sensor mechanism.

We measured the excited state lifetimes for the radiative decay for the films as a function of thickness and casting solution concentration. Dependent upon the thickness of Rh6G thin film, two or three lifetimes were required to fit the decay curves for the excited state of the thin films on PMMA surface.

The spin casting solution concentration, which directly affects the surface dye density and surface coverage, plays an important role in lifetime of Rh6G sub-monolayer and monolayer. As shown in Figure 4-9A, sub-monolayer and monolayer of Rh6G could be formed by spin casting solutions with

concentrations lower than 1 x 10^{-4} M, and there is a distinct lifetime change at concentration range 5 x 10^{-5}M – 1 x 10^{-4}M, corresponding to the film thickness of 0.9 nm and 1.0 nm.

As shown in Figure 4-9B, for the Rh6G thin film with thickness less than 0.9 nm: τ_1= 4.0 ± 0.6 ns, τ_2 = 1.9 ± 0.4 ns. For the Rh6G film thickness between 0.9 nm to 1.0 nm, the two lifetimes became longer (τ_1 = 6.4 ± 0.1 ns, and τ_2 = 2.7 ± 0.3 ns), and a new lifetime with τ_3 = 0.8 ± 0.2 ns appeared. For the Rh6G film thickness above 1.0 nm, second layer starts to form, the τ_1 and τ_2 became same as in sub-monolayer thin film, but the 3rd life time remained as 0.8 ± 0.2 ns. Based on the previous paper, the τ_1=4.0 ± 0.6 ns is assigned to the excited state excimer, τ_2 = 1.9 ± 0.4 ns is assigned to the monomer, and τ_3 = 0.8 ± 0.2 ns is assigned to the aggregate.

The lifetime time of τ_1 and τ_2 in 0.9 nm and 1.0 nm Rh6G thin film gets longer, suggesting the possibility of phase transfer, the excited state of monomer and excimer were more stable.

As shown in Figure 4-10, B1 is corresponds to the fraction of excited state excimer emissive component, B2 is corresponds to the fraction of monomer emissive component, B3 is corresponding to the fraction of emissive aggregate.

It shows for the Rh6G on the PMMA surface, at extremely low dye density, the ground state monomeric and the excited state excimer are dominating. Since B1 is significantly larger than B2, suggests that PMMA surface morphology

enhances the excited state excimer rather than simple ground monomer. When Rh6G molecules deposited on the PMMA surface, they are not distributing evenly across the surface. Instead, the molecules tend to accumulate together at a proximity close enough to allow excited state excimer to occur, but too far to form aggregates.

With the dye density increases, right around when the surface coverage reaching the saturation stage, the excited state excimer reaching the maxima, and resulting in the phase transfer, allowing maximum excited state excimer emission.

When second layer of Rh6G starts to form on top of the first Rh6G layer, emission from aggregate structure dominates.

SECTION 3: Adapt the mechanistic ideas developed to optimize the sensor performance. In the 0.7 nm sub-monolayer Rh6G film, the surface has the extremely low dye density, the surface coverage is low, monomeric structure is dominant. Allowing the monomeric Rh6G molecules interact with TNT molecules, resulting in the quenching of emission intensity as shown in Figure 4-11A.

In Figure 4-11B and 4-11C, is the monolayer with high coverage, exciton dimers and excited state excimer is presenting in the film. The existence of many radiative and non-radiative pathways shielding the emission change caused by TNT collision. At the same time, the amount of monomeric structure has decreased.

In Figure 4-11D, the second layer starts to form, results in aggregation. TNT causes a structural change in this film, disrupting aggregation, thus the enhancement of the emission can occur.

Figure 4-11E, bilayer of Rh6G thin films with aggregates dominating the film structure, leads to significant quenching of emission spectrum and suppression of the monomer, excimer and Exciton emission. And the interactions between dye molecules and TNT molecules were shielded. Thus no change can be observed.

For Rh6G on glass, either the extremely low surface coverage monolayer thin film or bilayer with the second layer just starts to form could be used in the TNT detection. As the three-layered structure enhancing the emission intensity as the amount of Rh6G is decreased. This is an advantage for improving sensitivity. Since only a small amount of Rh6G is required for a strong signal, only a small amount of analyte would be required to modulate the signal.

Rh6G was put on the 385 nm PMMA layer to amplify the emission intensity, emission change was observed before and after the exposure as shown in Figure 4-12.

All Rh6G films showed an emission decrease upon exposure to TNT except the thinnest sub-monolayer film as shown in Figure 4-12 A. At this surface coverage, the molecular density is too low, the interaction between monomeric

molecules and TNT molecules are very weak, thus no emission change can be obtained.

When surface coverage increases, as shown in Figure 4-12B and Figure 4-12C, the dominating emissive components are monomer and excited state excimer. Upon exposure to TNT molecules, a decrease in emission intensity observed.

At multi layer Rh6G film, a much smaller emission intensity drop observed. This is because the emissive components in the film are aggregates, monomer and excited state excimer, upon exposure to TNT molecules, emission intensity increases as TNT molecules break down the aggregate combines, and at the same time, emission decrease as TNT molecules interact with monomer. With these two combined effects on the emission, a much smaller emission change is observed.

CONCLUSION

The sensor system being discussed here has several unique features. The fluorescence amplification afforded by the layered structure provides improved sensitivity. The Rh6G emission intensity is significantly higher when coat on PMMA surface instead of glass surface. Both of the absorbance and emission of the Rh6G are shifted to the lower energy compared to the glass surface, which is attributed to the change in surface polarity, surface roughness and the surface wrinkle pattern. The surface of the PMMA tends to form uniform wrinkle pattern from thickness equals to 160 nm or above. The total surface area of PMMA film increases due to the formation of wrinkle, results in increased number of excited molecules from incident light beam. The wrinkle amplitude and wavelength are directly affected by the PMMA film thickness. The Rh6G emission intensity is affected by wrinkle amplitude. When the amplitude are in the 10 nm range, quantum confinement effects occurs and results in the high emission intensity. As the amplitude increase, the emission intensity decreases. Further, this emission intensity also depends on the thickness of the PMMA interfacial structure. As the thickness increases, less internal reflection could occur, thus the emission intensity drops.

The PMMA surface affects the Rh6G dominating species in the thin film. The aggregation is less favored on the PMMA surface. At extreme low dye density and coverage, the monomeric and excited state excimer components are

dominating. And as closer to reach surface saturation, where the Rh6G film thickness between 0.9 nm and 1.0 nm, the emission intensity increases as a result of phase transfer.

The thickness of the Rh6G is a key feature in determining the sensitivity of the sensor. 0.7 nm Rh6G which has the monomeric units dominating in the film, allowing collision with TNT vapor molecules, results in the quenching of the emission, 1.5 nm Rh6G film which is at the stage of just forming the second layer with aggregates as the dominating species, the TNT molecules breaking down the aggregates, thus the emission is enhanced.

With Rh6G films on PMMA, and the PMMA surface is less favor to form aggregates in comparison to glass surface, only quenching of emission intensity occurred.

ACKNOWLEDGEMENT

This material is based upon work supported by the U.S. Department of Homeland Security, Science and Technology Directorate, Office of University Programs, under Grant Award 2013-ST-061-ED0001. The views and conclusions contained in this document are those of the authors and should not be interpreted as necessarily representing the official policies, either expressed or implied, of the U.S. Department of Homeland Security.

LIST OF REFERENCES

(1) Senesac, L.; Thundat, T. G. Nanosensors for Trace Explosive Detection. *Mater. Today* **2008**, *11* (3), 28–36.

(2) Singh, S. Sensors-An Effective Approach for the Detection of Explosives. *J. Hazard. Mater.* **2007**, *144* (1–2), 15–28.

(3) Strle, D.; Štefane, B.; Zupanič, E.; Trifkovič, M.; Maček, M.; Jakša, G.; Kvasič, I.; Muševič, I. Sensitivity Comparison of Vapor Trace Detection of Explosives Based on Chemo-Mechanical Sensing with Optical Detection and Capacitive Sensing with Electronic Detection. *Sensors (Switzerland)* **2014**, *14* (7), 11467–11491.

(4) Caygill, J. S.; Davis, F.; Higson, S. P. J. Current Trends in Explosive Detection Techniques. *Talanta* **2012**, *88* (January), 14–29.

(5) Lefferts, M. J.; Castell, M. R. Vapour Sensing of Explosive Materials. *Anal. Methods* **2015**, 9005–9017.

(6) Kasprzak, B.; Pękala, J.; Stępień, A. F.; Świerczyński, Z. Metrology and Measurement Systems. *Architecture* **2010**, *XVII* (4), 537–547.

(7) Zhang, H. Q.; Euler, W. B. Sensors and Actuators B : Chemical Detection of Gas-Phase Explosive Analytes Using Fluorescent Spectroscopy of Thin Films of Xanthene Dyes. *Sensors Actuators B. Chem*. **2016**, *225*, 553–562.

(8) Yang, J.-S.; Swager, T. M. Fluorescent Porous Polymer Films as TNT Chemosensors: Electronic and Structural Effects. *J Am Chem Soc* **1998**, *120*, 11864–11873.

(9) Zhang, J.; Fu, Y.; Lakowicz, J. R. Enhanced Förster Resonance Energy Transfer (FRET) on Single Metal Particle. *J. Phys. Chem. C. Nanomater. Interfaces* **2007**, *111* (1), 50–56.

(10) Qin, A.; Lam, J. W. Y.; Tang, L.; Jim, C. H. W.; Zhao, H.; Sun, J.; Tang, B. Z. Polytriazoles with Aggregation-Induced Emission Characteristics: Synthesis by Click Polymerization and Application as Explosive Chemosensors. *Macromolecules* **2009**, *42* (5), 1421–1424.

(11) Díaz de Greñu, B.; Moreno, D.; Torroba, T.; Berg, A.; Gunnars, J.; Nilsson, T.; Nyman, R.; Persson, M.; Pettersson, J.; Eklind, I.; et al. Fluorescent Discrimination between Traces of Chemical Warfare Agents and Their Mimics. *J. Am. Chem. Soc.* **2014**, *136* (11), 4125–4128.

(12) Latendresse, C. A.; Fernandes, S. C.; You, S.; Zhang, H. Q.; Euler, W. B.; Almirall, J. R.; Xu, D.; Ray, P. C.; Mayhew, C. A. A Fluorometric Sensing Array for the Detection of Military Explosives and IED Materials. *Anal. Methods* **2013**, *5* (20), 5457.

(13) Narayanan, A.; Varnavski, O. P.; Swager, T. M.; III, T. G. Multiphoton Fluorescence Quenching of Conjugated Polymers for TNT Detection. *J. Phys. Chem. C* **2008**, *112*, 881–884.

(14) Levitsky, I. A.; Euler, W. B.; Tokranova, N.; Rose, A. Fluorescent Polymer-Porous Silicon Microcavity Devices for Explosive Detection. *Appl. Phys. Lett.* **2007**, *90* (4), 41904.

(15) Martinho, J. M. G.; SReis e Sousa, A. .; Oliveira Torres, M. E.; Fedorov, A. Fluorescence Quenching of Pyrene Monomer and Excimer by CH3I. *Chem. Phys.* **2001**, *264* (1), 111–121.

(16) Koenen, J.-M.; Zhu, X.; Pan, Z.; Feng, F.; Yang, J.; Schanze, K. S. Enhanced Fluorescence Properties of Poly(phenylene Ethynylene)-Conjugated Polyelectrolytes Designed to Avoid Aggregation. *ACS Macro Lett*. **2014**, *3* (5), 405–409.

(17) Lee, P.; Li, W.-C.; Chen, B.-J.; Yang, C.-W.; Chang, C.-C.; Botiz, I.; Reiter, G.; Lin, T.-L.; Tang, J.; Yang, A. C.-M. Massive Enhancement of Photoluminescence through Nanofilm Dewetting. *ACS Nano* **2013**, *7* (8), 6658–6666.

(18) Li, H.; Chen, C.-Y.; Wei, X.; Qiang, W.; Li, Z.; Cheng, Q.; Xu, D. Highly Sensitive Detection of Proteins Based on Metal-Enhanced Fluorescence with Novel Silver Nanostructures. *Anal. Chem*. **2012**, *84* (20), 8656–8662.

(19) Cao, X.; Meng, L.; Li, Z.; Mao, Y.; Lan, H.; Chen, L.; Fan, Y.; Yi, T. Large Red-Shifted Fluorescent Emission via Intermolecular Π–π Stacking in 4-Ethynyl-1,8-Naphthalimide-Based Supramolecular Assemblies. *Langmuir* **2014**, *30* (39), 11753–11760.

(20) Laban, B.; Vodnik, V.; Dramićanin, M.; Novaković, M.; Bibić, N.; Sovilj, S. P.; Vasić, V. M. Mechanism and Kinetics of J-Aggregation of Thiacyanine Dye in the Presence of Silver Nanoparticles. *J. Phys. Chem. C* **2014**, *118* (40), 23393–23401.

(21) Liu, J.; Zhong, Y.; Lam, J. W. Y.; Lu, P.; Hong, Y.; Yu, Y.; Yue, Y.; Faisal, M.; Sung, H. H. Y.; Williams, I. D.; et al. Hyperbranched Conjugated Polysiloles: Synthesis, Structure, Aggregation-Enhanced Emission, Multicolor Fluorescent Photopatterning, and Superamplified Detection of Explosives. *Macromolecules* **2010**, *43* (11), 4921–4936.

(22) Yuan, W. Z.; Zhao, H.; Shen, X. Y.; Mahtab, F.; Lam, J. W. Y.; Sun, J. Z.; Tang, B. Z. Luminogenic Polyacetylenes and Conjugated Polyelectrolytes: Synthesis, Hybridization with Carbon Nanotubes, Aggregation-Induced Emission, Superamplification in Emission Quenching by Explosives, and Fluorescent Assay for Protein Quantitation. *Macromolecules* **2009**, *42* (24), 9400–9411.

(23) Andrew Satrijo; Steven E. Kooi, A.; Swager*, T. M. Enhanced Luminescence from Emissive Defects in Aggregated Conjugated Polymers. 2007.

(24) Nandi, L. G.; Nicoleti, C. R.; Bellettini, I. C.; Machado, V. G. Optical Chemosensor for the Detection of Cyanide in Water Based On Ethyl(hydroxyethyl)cellulose Functionalized with Brooker's Merocyanine. *Anal. Chem.* **2014**, *86* (10), 4653–4656.

(25) Lin, W.-C.; Fang, S.-K.; Hu, J.-W.; Tsai, H.-Y.; Chen, K.-Y. Ratiometric Fluorescent/Colorimetric Cyanide-Selective Sensor Based on Excited-State Intramolecular Charge Transfer−Excited-State Intramolecular Proton Transfer Switching. *Anal. Chem.* **2014**, *86* (10), 4648–4652.

(26) Gao, D.; Wang, Z.; Liu, B.; Ni, L.; Wu, M.; Zhang, Z. Resonance Energy Transfer-Amplifying Fluorescence Quenching at the Surface of Silica Nanoparticles toward Ultrasensitive Detection of TNT. *Anal. Chem*. **2008**, *80* (22), 8545–8553.

(27) Goldman, E. R.; Medintz, I. L.; Whitley, J. L.; Hayhurst, A.; Clapp, A. R.; Uyeda, H. T.; Deschamps, J. R.; Lassman, M. E.; Mattoussi, H. A Hybrid Quantum Dot−Antibody Fragment Fluorescence Resonance Energy Transfer-Based TNT Sensor. *J Am Chem Soc* **2005**, *127*, 6744–6751.

(28) Thomas, S. W.; Joly, G. D.; Swager, T. M. Chemical Sensors Based on Amplifying Fluorescent Conjugated Polymers. *Chem. Rev*. **2007**, *107* (4), 1339–1386.

(29) Jenie, S. N. A.; Pace, S.; Sciacca, B.; Brooks, R. D.; Plush, S. E.; Voelcker, N. H. Lanthanide Luminescence Enhancements in Porous Silicon Resonant Microcavities. *ACS Appl. Mater. Interfaces* **2014**, *6* (15), 12012–12021.

(30) Kurian, A.; George, N.; Paul, B.; Nampoori, V. P. N.; Vallabhan, C. P. G. Studies on Fluorescence Efficiency and Photodegradation of Rhodamine 6G Doped PMMA Using a Dual Beam Thermal Lens Technique. *Laser Chem.* **2002**, *20*, 99–110.

(31) Somasundaram, G.; Ramalingam, A. Laser Gain Studies of Rhodamine 6G Dye Doped Polymer Laser. *Indian J. Pure Appl. Phys.* **1998**, *36* (6), 310–313.

(32) Martín, V.; Bañuelos, J.; Enciso, E.; Arbeloa, Í.; Costela, Á.; García-Moreno, I. Photophysical and Lasing Properties of Rhodamine 6G Confined in Polymeric Nanoparticles. *J. Phys. Chem. C* **2011**, *115* (10), 3926–3933.

(33) Arbeloa, F.; Estevez, M.; Arbeloa, T.; Arbeloa, I. Spectroscopic Study of the Adsorption of Rhodamine 6G on Clay Minerals in Aqueous Suspensions. *Clay Miner*. **1997**, 32, 97–106.

(34) Tapia Estevez, M.; López Rbeloa, F.; López Rbeloa, T.; López Rbeloa, I.; Schoonheydt, R. Spectroscopic Study of the Adsorption of Rhodamine 6G on Laponite B for Low Loadings. *Clay Min*. **1994**, *29*, 105–113.

(35) Vogel, R.; Meredith, P.; Harvey, M. D.; Rubinsztein-Dunlop, H. Absorption and Fluorescence Spectroscopy of Rhodamine 6G in Titanium Dioxide Nanocomposites. *Spectrochim. Acta - Part A Mol. Biomol. Spectrosc*. **2004**, *60* (1–2), 245–249.

(36) Ojeda, P. R.; Amashta, I. a. K.; Ochoa, J. R.; Arbeloa, I. L. Excitonic Treatment and Bonding of Aggregates of Rhodamine 6G in Ethanol. *J. Chem. Soc. Faraday Trans. 2* **1988**, *84* (1), 1.

(37) Hung, J.; Castillo, J.; Olaizola, A. M. Fluorescence Spectra of Rhodamine 6G for High Fluence Excitation Laser Radiation. *J. Lumin*. **2003**, *101* (4), 263–268.

(38) Chapman, M.; Mullen, M.; Novoa-Ortega, E.; Alhasani, M.; Elman, J. F.; Euler, W. B. Structural Evolution of Ultrathin Films of Rhodamine 6G on Glass. *J. Phys. Chem. C* **2016**, *120* (15), 8289–8297.

(39) Lasio, B.; Malfatti, L.; Innocenzi, P. Photodegradation of Rhodamine 6G Dimers in Silica Sol-Gel Films. *J. Photochem. Photobiol. A Chem*. **2013**, *271*, 93–98.

(40) Martínez, V. M.; Arbeloa, F. L.; Prieto, J. B.; Arbeloa, I. L. Characterization of Rhodamine 6G Aggregates Intercalated in Solid Thin Films of Laponite Clay. 2 Fluorescence Spectroscopy. *J. Phys. Chem. B* **2005**, *109* (15), 7443–7450.

(41) Malfatti, L.; Kidchob, T.; Aiello, D.; Aiello, R.; Testa, F.; Innocenzi, P. Aggregation States of Rhodamine 6G in Mesostructured Silica Films. *J. Phys. Chem. C* **2008**, *112* (42), 16225–16230.

(42) Taguchi, J.; Yano, T.; Habuchi, S.; Vacha, M.; Shibata, S. Control of Orientation of Rhodamine 6G in Organic-Inorganic Hybrid Film by Capillary Electrophoresis Doping Technique. *Thin Solid Films* **2011**, *519* (18), 6106–6109.

(43) Khan, A. U.; Kasha, M. Mechanism of Four-Level Laser Action in Solution Excimer and Excited-State Proton- Transfer Cases. *Proc. Natl. Acad. Sci. USA* **2016**, *80* (6), 1767–1770.

(44) Focsaneanu, K.; Scaiano, J. C. Potential Analytical Applications of Differential Fluorescence Quenching: Pyrene Monomer and Excimer Emissions as Sensors for Electron Deficient Molecules. *Photochem. Photobiol. Sci.* **2005**, *4* (10), 817–821.

(45) Birks, J. Excimers. *Rep.Prog. Phys* **1975**, *38*, 903–974.

(46) Claire, P. D. Sainte. Molecular Simulation of Excimer Fluorescence in Polystyrene and Poly (Vinylcarbazole). **2006**, 7334–7343.

(47) Song, Q.; Bamesberger, A.; Yang, L.; Houtwed, H.; Cao, H. Excimer-Monomer Switch: A Reaction-Based Approach for Selective Detection of Fluoride. *Analyst* **2014**, *139* (14), 3588–3592.

(48) Ibnaouf, K. H. Excimer State of a Conjugated Polymer (MEH-PPV) in Thin Films. *Opt. Laser Technol.* **2013**, *48*, 401–404.

(49) Bains, G. K.; Kim, S. H.; Sorin, E. J.; Narayanaswami, V. The Extent of Pyrene Excimer Fluorescence Emission Is a Reflector of Distance and Flexibility: Analysis of the Segment Linking the LDL Receptor-Binding and Tetramerization Domains of Apolipoprotein E3. *Biochemistry* **2012**, *51* (31), 6207–6219.

(50) Yip, W. T.; Levy, D. H. Excimer / Exciplex Formation in van Der Waals Dimers of Aromatic Molecules. **1996**, *3654* (95), 11539–11545.

(51) Ojeda, P. R.; Katime, I.; Ochoa, J. R.; López, I. Excitonic Treatment and Bonding of Aggregates of Rhodamine 6G in Ethanol. *J. Chem. Soc. Faraday Trans. 2* **1988**, *84*, 1–8.

(52) Gilani, A. G.; Sariri, R.; Bahrpaima, K. Aggregate Formation of Rhodamine 6G in Anisotropic Solvents. *Spectrochim. Acta - Part A Mol. Biomol. Spectrosc.* **2001**, *57* (1), 155–161.

(53) Wang, H.; Yang, Q.; Sun, L.; Wang, S.; Wang, W.; Zhang, C.; Li, Y.; Xu, S.; Li, Y. Aggregation States of Rhodamine 6G in Electrospun Nanofibrous Films. *J. Colloid Interface Sci.* **2010***, 341* (2), 224–231.

(54) Antonov, L.; Gergov, G.; Petrov, V.; Kubista, M.; Nygren, J. UV-Vis Spectroscopic and Chemometric Study on the Aggregation of Ionic Dyes in Water. *Talanta* **1999**, *49*, 99–106.

(55) Kunjappu, J. O. Y. T.; Manohar, C. Aggregagtion Characteristics of Laser Dye Rhodamine 6G in Aqueous Surfactant Solutions. **1990**, *52* (4), 717–721.

(56) Zehentbauer, F. M.; Moretto, C.; Stephen, R.; Thevar, T.; Gilchrist, J. R.; Pokrajac, D.; Richard, K. L.; Kiefer, J. Fluorescence Spectroscopy of Rhodamine 6G: Concentration and Solvent Effects. *Spectrochim. Acta - Part A Mol. Biomol. Spectrosc.* **2014**, *121*, 147–151.

(57) Penzkofer, A.; Lu, Y. Fluorescence Quenching of Rhodamine 6g in Methanol at High Concentration. *Chem. Phys*. **1986**, *103*, 399–405.

(58) Fischer, M.; Georges, J. Fluorescence Quantum Yield of Rhodamine 6G in Ethanol as a Function of Concentration Using Thermal Lens Spectrometry S) Xf. **1996**, *2614* (September), 0–3.

(59) Mullen, M.; Euler, W. B. The Influence of Interfacial Effects on the Photophysics of Rhodamine 6G Thin Films on a Poly(vinylidene Fluoride) Surface. *Langmuir* **2017**, *33* (9), 2194–2204.

(60) Matoian, M. A.; Sweetman, R.; Hall, E. C.; Albanese, S.; Euler, W. B. Light Trapping to Amplify Metal Enhanced Fluorescence with Application for Sensing TNT. *J Fluoresc* **2013**, *23*, 877–880.

(61) Kivioja, A. O.; Jääskeläinen, A.-S.; Ahtee, V.; Vuorinen, T. Thickness Measurement of Thin Polymer Films by Total Internal Reflection Raman

and Attenuated Total Reflection Infrared Spectroscopy. *Vib. Spectrosc*. **2012**, *61*, 1–9.

(62) Tran, W.; Tisinger, L. G.; Lavalle, L. E.; Sommer, A. J. Analysis of Thin-Film Polymers Using Attenuated Total Internal Reflection-Raman Microspectroscopy. *Appl. Spectrosc*. **2015**, *69* (2), 230–238.

(63) Walsh, C. B.; Franses, E. I. Ultrathin PMMA Films Spin-Coated from Toluene Solutions. **2003**, *429* (September 2002), 71–76.

(64) Zhongfeng, T.; Youshuang, C.; Xiaoxing, T. Morphology of Irradiated PMMA Membranes Prepared by Phase Inversion with Supercritical CO_2. ***2013***, *24* (11005148), 1–7.

(65) Tippo, T.; Thanachayanont, C.; Muthitamongkol, P.; Junin, C.; Hietschold, M.; Thanachayanont, A. The Effects of Solvents on the Properties of Ultra-Thin Poly (Methyl Methacrylate) Films Prepared by Spin Coating. *Thin Solid Films* **2013**, *546*, 180–184.

(66) Semaltianos, N. G. Spin-Coated PMMA Films. **2007**, *38*, 754–761.

(67) Toal, S. J.; Trogler, W. C.; Dugan, R. E.; Trogler, W. C.; Lo, S. M. F.; Williams, I. D.; Zhu, D.; Tang, B. Z. Polymer Sensors for Nitroaromatic Explosives Detection. *J. Mater. Chem.* **2006**, *16* (28), 2871.

(68) Moore, D. S. Recent Advances in Trace Explosives Detection Instrumentation. *Sens. Imaging An Int. J.* **2007**, *8* (1), 9–38.

(69) Andrew, T. L.; Swager, T. M. A Fluorescence Turn-On Mechanism to Detect High Explosives RDX and PETN. *J Am Chem Soc* **2007**, *129*, 7254–7255.

(70) Nadoo, T.; Yang, X.; Moore, J.; Zang, L. Highly Responsive Fluorescent Sensing of Explosives Taggant with an Organic Nanofibril Film. *Sensors Actuators B Chem.* **2008**, *134* (1), 287–291.

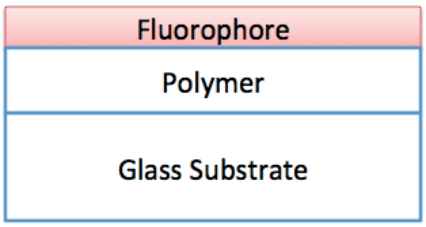

Scheme 4-1. The general structure of the sensor

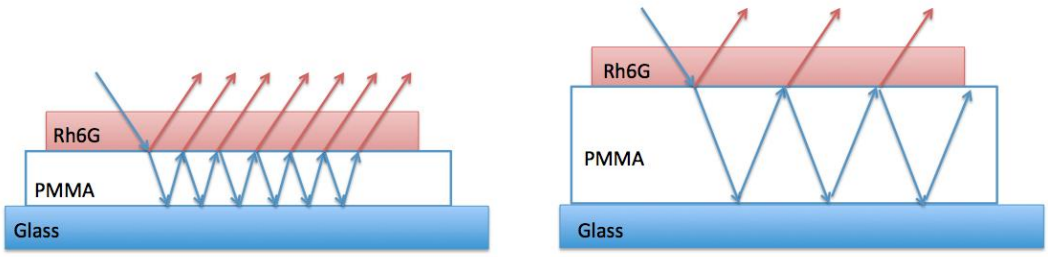

Scheme 4-2. Simple internal reflection model of thin (left) and thick (right) PMMA layer

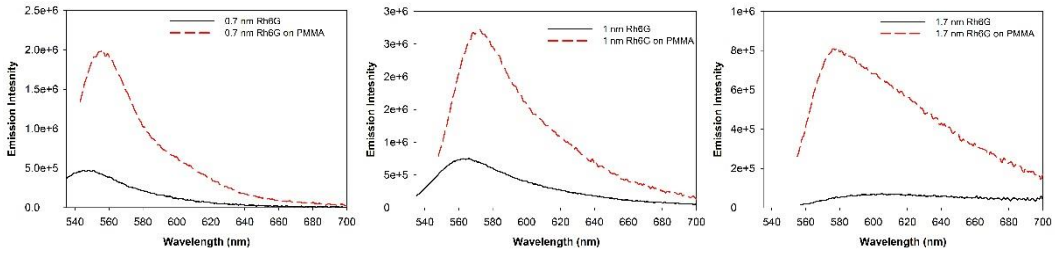

Figure 4-1. Steady-state emission spectra for spin-cast Rh6G thin films on glass surface (black) and PMMA surface (red)

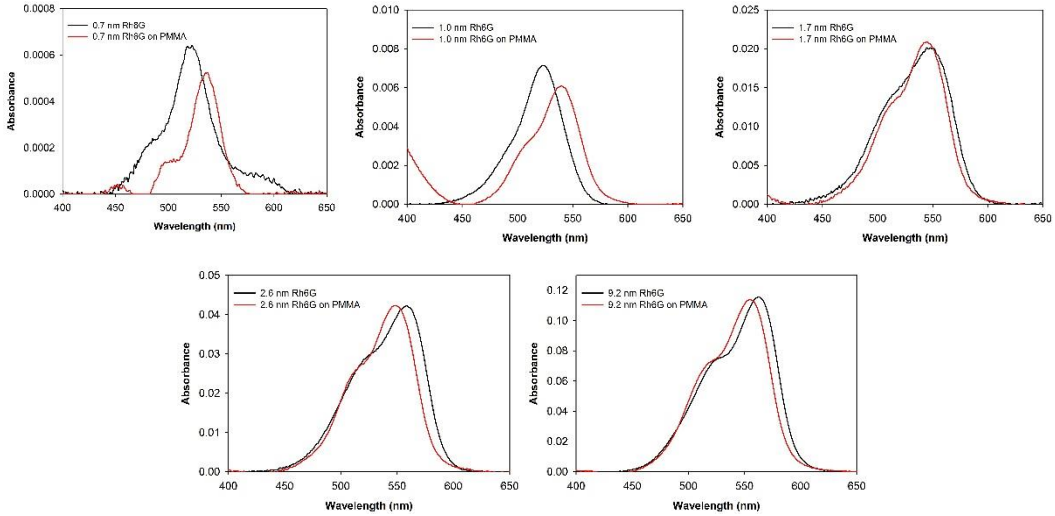

Figure 4-2. Absorbance spectra of Rh6G on glass (black) and 385 nm PMMA (red)

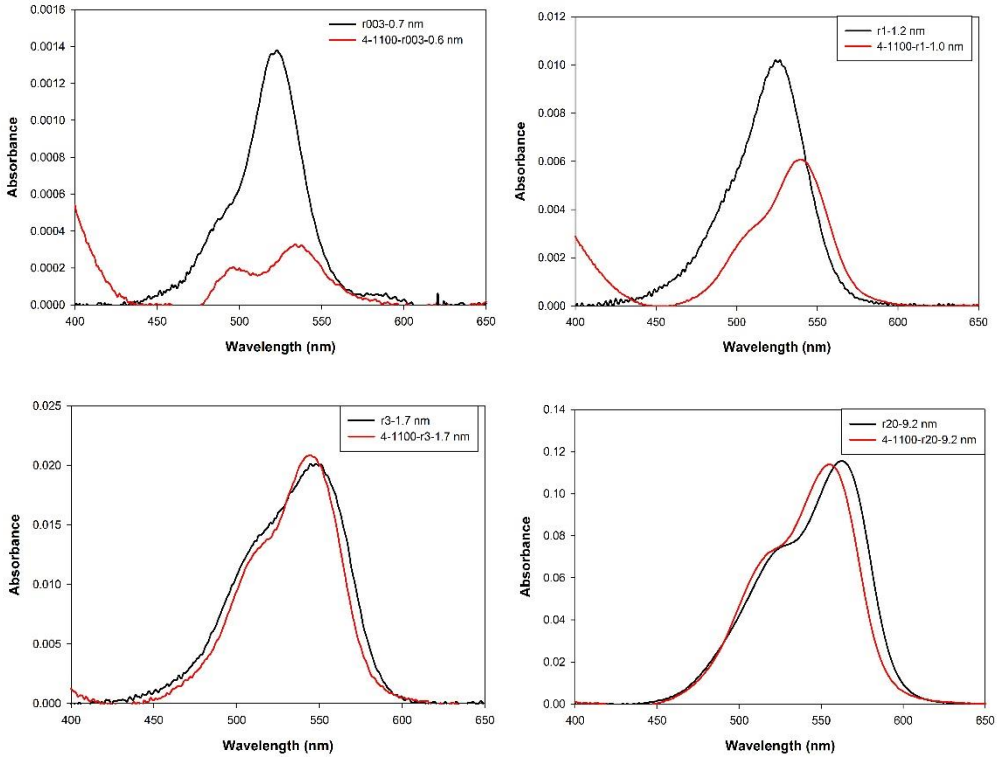

Figure 4-3. Absorbance of Rh6G film on glass surface (black) and 385 nm PMMA film surface (red) with different deposition solution concentration, (A) $3x10^{-6}$ M, (B) $1x10^{-4}$ M, (C) $3x10^{-4}$ M, (D) $2x10^{-3}$ M.

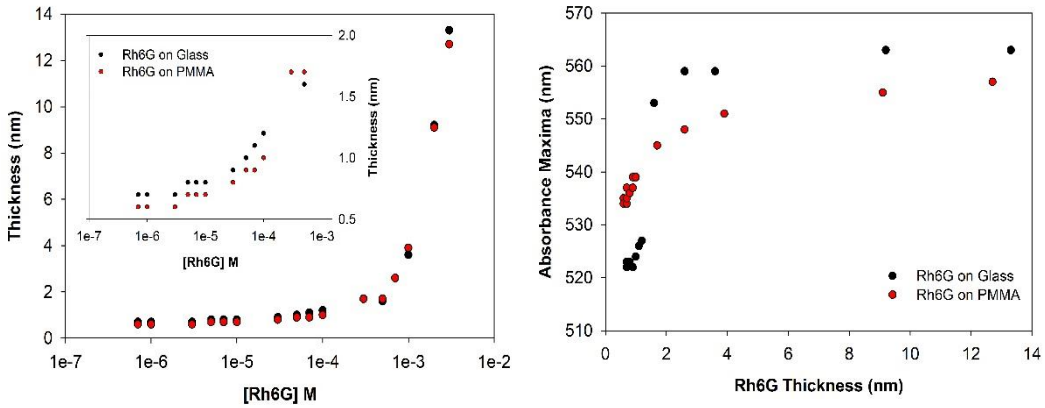

Figure 4-4. (A) Rh6G thin film thickness on glass surface (black) and on 385 nm PMMA film surface (red) as a function of Rh6G solution concentration, (B) The absorbance maxima of Rh6G thin films on glass (black) and PMMA (black) surface as a function of Rh6G film thickness.

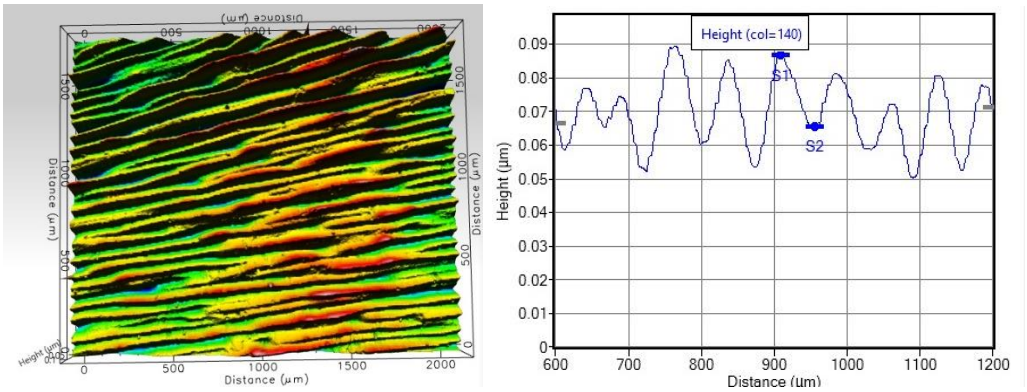

Figure 4-5. Optical profiles of 385 nm PMMA films spin-cast from 4% w/v solution. The image was taken near the edge of the film. Right: Height profile of the image shown in the left. The profile was taken at the right edge in the left image.

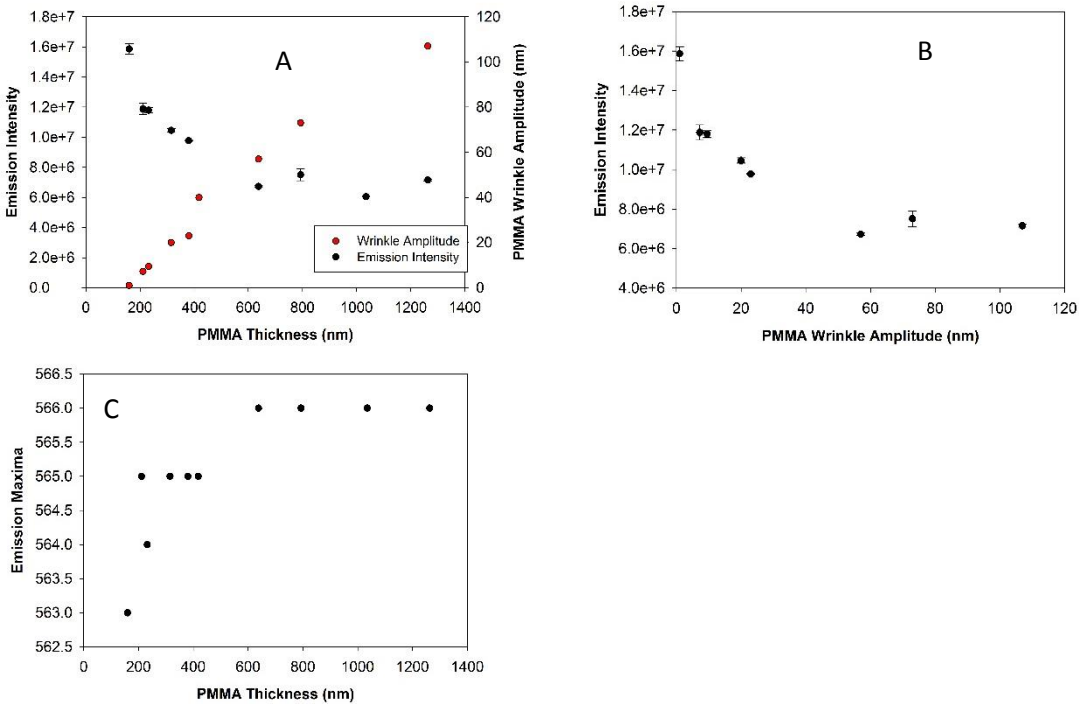

Figure 4-6. 1.0 nm Rh6G thin film (A) emission intensity and PMMA wrinkle amplitude (B) emission intensity and (C) wavelength maxima change as a function of PMMA layer thicknesses.

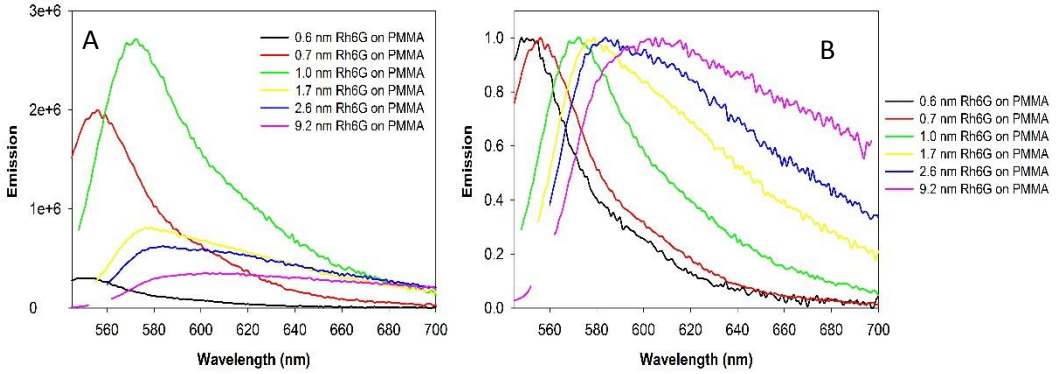

Figure 4-7. (A) Steady-state emission spectra and (B) normalized emission spectra for spin-cast Rh6G thin films on 385 nm PMMA surface as a function of film thickness: 0.7, 1.0, 1.1, 1.2, 1.4, 2.1 nm.

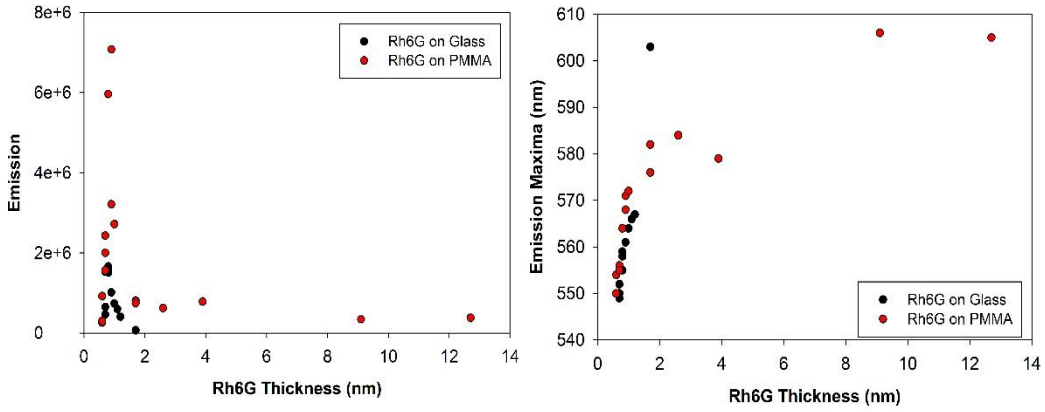

Figure 4-8. (A) Emission intensity changes and (B) emission wavelength maxima Shifts of Rh6G thin films on glass (black) and PMMA surface (red) as a function of Rh6G film thickness.

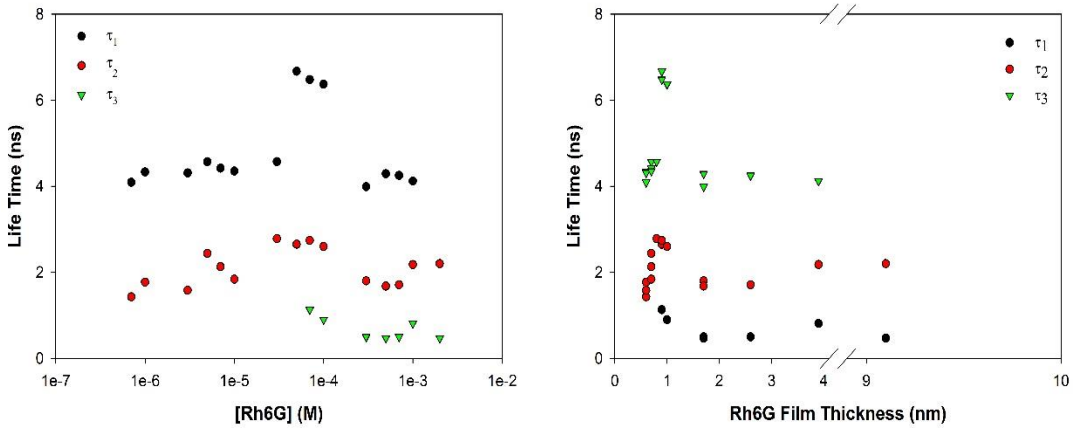

Figure 4-9. Lifetime of Rh6G film on 385 nm PMMA as a function of (a) Rh6G concentration, (b) Rh6G film thickness

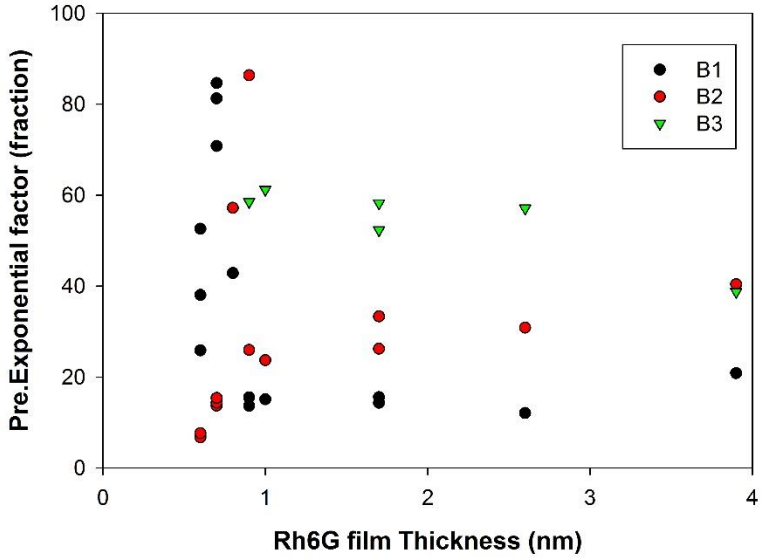

Figure 4-10. The fluorescence components fraction in Rh6G films on 385 nm PMMA. All decay curves are 3-exponential fits: $I(t)=B_1e^{-t/\tau_1} + B_2e^{-t/\tau_2} + B_3e^{-t/\tau_3}$, the pre-exponential factor as a fraction as function of Rh6G film thickness.

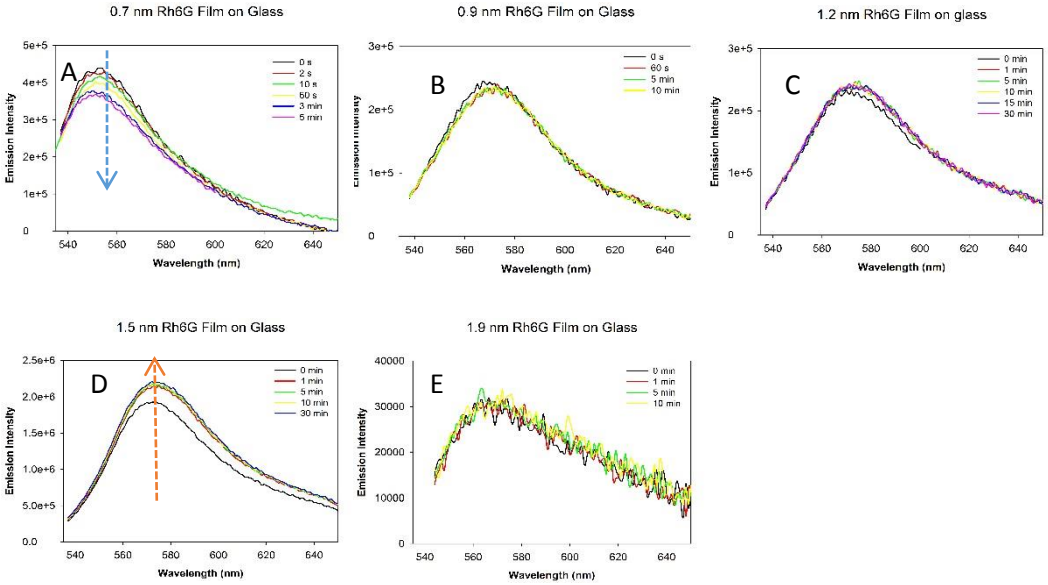

Figure 4-11. Emission intensity changes for different thickness of Rh6G thin films on glass before and after TNT exposure.

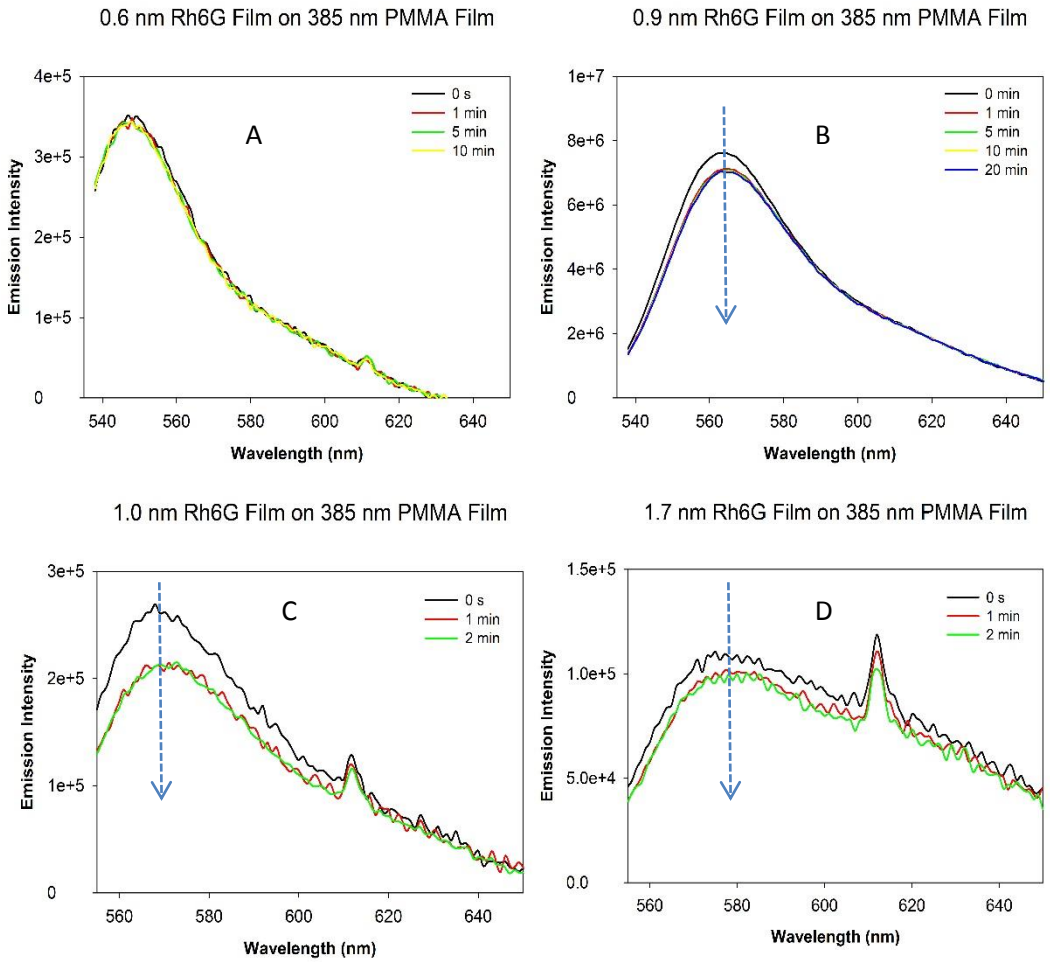

Figure 4-12. Emission intensity changes for different thickness of Rh6G thin films on 385 nm PMMA before and after TNT exposure.